

---

---

A Photometric Study  
of  
Transiting Extrasolar Planets

---

---

Nikolay Krasimirov Nikolov

Max-Planck-Institut für Astronomie





Dissertation in Astronomy  
submitted to the  
Combined Faculties for the Natural Sciences and for Mathematics  
of the Ruperto-Carola University of Heidelberg, Germany.  
for the degree of  
Doctor of Natural Sciences

Put forward by

MASTER PHYS. NIKOLAY KRASIMIROV NIKOLOV

born in: Sevlievo (Bulgaria)

Oral examination: April 13<sup>th</sup>, 2011



---

---

A Photometric Study  
of  
Transiting Extrasolar Planets

---

---

Referees: Prof. Dr. Thomas Henning  
Prof. Dr. Joachim Wambsganss



# Ein Photometrisches Studium Extrasolarer Transitplaneten

In dieser Dissertation präsentiere ich Beobachtungsmethoden um extrasolare Transitplaneten zu detektieren und zu charakterisieren. Ich untersuche die häufigsten Fälle von Fehlidentifikationen, die durch erdgebundene photometrische Surveys identifiziert wurden. Ich implementiere und teste drei robuste Methoden für die Pan-Planets pipeline um Fehlidentifikationen zu identifizieren. Diese basiert auf der Bewertung der out-of-eclipse ellipsoiden Variabilität, Bestimmung der astrophysikalischen Parameter durch einen Fit des Transits und Exoplanetendiagnostik ( $\eta$ ), d.h. der Analyse der Morphologie ihrer Transitlichtkurven. Ich stelle meine Ergebnisse von systematischen Tests der Pipeline mit Hilfe von OGLE-Daten, Pan-Planets Simulationen und bestätigten Transit-Exoplaneten dar. Ich bestätige die erste Methode als die zuverlässigste um transitartige Ereignisse durch binäre Sternsysteme auszuschliessen.

Weiterhin präsentiere ich Ergebnisse einer photometrischen Analyse von Daten, die mit dem LAIWO Instrument am 1-m Teleskop der WISE Observatorium aufgenommen wurden. Ich untersuche die notwendigen Methoden um Lichtkurven hoher Qualität im Millimagnitudenbereich bis hinunter zu  $R = 16$  mag zu erhalten. Ich führe eine Suche nach periodischen Transitereignissen ( $1 - 2\%$ ) und variablen Sternen durch und identifiziere 22 Transitkandidaten sowie 20 periodisch variable Sterne. Eine Analyse von photometrischen Farben, ellipsoider Variabilität und Exoplanetendiagnostik legt nahe, dass zwischen null und zwei der Lichtkurven durch Exoplaneten erzeugt wurden. Desweiteren empfehle ich eine Follow-up Strategie für deren Bestätigung.

Schliesslich analysiere ich Multiband optische und nah-infrarote Photometrie von WASP-4 mit hohem Signal-zu-Rauschen Verhältnis von drei Transits eines Exoplaneten. Die Daten wurden mit dem GROND Instrument des ESO/MPG 2.2-m Teleskop des La Silla Observatoriums aufgenommen. Ich erstelle und analysiere die Lichtkurven und vermesse den Planetenradius, die Periode des Orbits, die grosse Halbachse sowie die Inklination gemeinsam mit der Zeit des Transits. Eine Analyse der WASP-4b Transit Ephemeriden bestimmt aus den Ergebnissen, bestätigt das Fehlen von Variationen der Zeiten des Transits (TTVs).

## A Photometric Study of Transiting Extrasolar Planets

In this thesis I present observational methods to detect and characterize transiting extrasolar planets. I study the most common types of astrophysical false positives, identified by ground based photometric transit surveys. I implement and test three robust methods for the Pan-Planets pipeline to classify false alarms, based on the transit light curve morphology: evaluation of out-of-eclipse ellipsoidal variability; determination of astrophysical parameters from a transit fit; and exoplanet diagnostic ( $\eta$ ). I obtain results from systematic tests of the pipeline using data from OGLE, Pan-Planets simulations and confirmed transiting exoplanets. I confirm the first method as most reliable in ruling out transit-like events due to stellar binaries.

I further, present results from a photometric analysis of data obtained with LAIWO at the 1-m telescope at Wise Observatory. I study the necessary methods to obtain high quality light curves at the millimagnitude level down to  $R = 16$  mag. I perform a search for periodic transit events ( $1 - 2\%$ ) and variable stars and identify 22 transit candidates as well as 20 periodic variables. An analysis of the photometric colors, ellipsoidal variability and the exoplanet diagnostic suggests that between zero and two of the light curves should be produced by exoplanets. Furthermore, I propose a follow-up scheme for their confirmation.

Finally, I obtain high signal-to-noise ratio simultaneous multi-band optical/NIR photometry of WASP-4, during three transits of its exoplanet, with the GROND instrument at the ESO/MPG 2.2-m telescope at La Silla Observatory. I produce and analyze its light curves and measure the planet radius, orbital period, semimajor axis and inclination in conjunction with a study of the transit mid-times. An analysis of WASP-4b transit ephemeris, derived from the results, confirms the lack of transit timing variations (TTVs).



*This thesis is dedicated to my family*





---

# Contents

<b>Acknowledgements</b>	<b>ix</b>
<b>Introduction</b>	<b>1</b>
<b>1 Transiting Exoplanets</b>	<b>5</b>
1.1 The method . . . . .	5
1.2 Transit surveys . . . . .	7
1.3 Science from transiting exoplanets . . . . .	10
1.3.1 Transmission spectroscopy . . . . .	11
1.3.2 Occultation spectroscopy . . . . .	12
1.3.3 Rossiter-McLaughlin effect . . . . .	12
1.3.4 Eclipse timing . . . . .	14
<b>2 Transit False Alarms</b>	<b>17</b>
2.1 Introduction . . . . .	17

2.1.1	Eclipsing binary stars . . . . .	17
2.1.2	Multiple systems . . . . .	18
2.2	Morphological analysis of the light curves . . . . .	19
2.2.1	Inspection of the out-of-eclipse parts. Detection of ellipsoidal variability . . . . .	19
2.2.2	Inspection of the transit shape . . . . .	26
2.2.3	Exoplanet diagnostic $\eta$ . . . . .	32
<b>3</b>	<b>Detection of Exoplanets With LAIWO</b>	<b>39</b>
3.1	The GITPO program . . . . .	39
3.2	Observations . . . . .	39
3.2.1	The LAIWO instrument . . . . .	39
3.2.2	Data acquisition . . . . .	40
3.3	Data reduction . . . . .	42
3.3.1	Image calibration . . . . .	42
3.3.2	Stellar source detection and image quality constraints . . . . .	43
3.4	Photometry . . . . .	51
3.4.1	Source measurement . . . . .	51
3.4.2	Astrometry and matching to stellar catalogs . . . . .	53
3.4.3	Differential photometry . . . . .	58
3.4.4	Data loss . . . . .	66
3.4.5	Time stamp . . . . .	68
3.5	Detrending . . . . .	68
3.6	Detection of variability . . . . .	70
3.6.1	Transit search . . . . .	70

<i>Contents</i>	vii
3.6.2 Variable stars . . . . .	77
3.7 Transit light curve analysis . . . . .	81
3.7.1 Overlap with previous transit surveys . . . . .	81
3.7.2 Size estimation . . . . .	81
3.7.3 Exoplanet diagnostic ( $\eta$ ) . . . . .	86
3.7.4 Ellipsoidal variability . . . . .	87
3.8 Planetary candidates summary and proposed scheme for efficient follow-up	90
<b>4 Multi-band Photometry of WASP-4</b>	<b>93</b>
4.1 Introduction . . . . .	93
4.2 Observations . . . . .	94
4.3 Data reduction and photometric analysis . . . . .	95
4.4 System parameters . . . . .	96
4.5 Results . . . . .	97
<b>Conclusions</b>	<b>105</b>
<b>Appendices</b>	<b>109</b>
<b>Appendices</b>	<b>114</b>
<b>Bibliography</b>	<b>121</b>



---

## Acknowledgements

I am most indebted and grateful to my supervisors, Thomas Henning, Reinhard Mundt and Cristina Afonso, for their patient and always expert supervision and for the encouragement they also granted to me to pursue my research activities.

I am grateful to my colleague and friend Maximiliano Leonardo Moyano D'Angelo for the constructive discussions and always positive support.

I thank to all my collaborators: Monika Lendl, Johannes Koppenhoefer, Nicola Da Rio, Joe Carson, Johny Setiawan, Mathias Zechmeister, Michaela Doellinger for the fruitful discussions, expert comments and responsibility.

I acknowledge to the Klaus Tschira Stiftung (KTS), which funded my PhD research.

I thank the Heidelberg Graduate School of Fundamental Physics, the International Max-Planck Research School and the Max-Planck Institute for Astronomy for the excellent opportunity I was granted, and for the additional financial support.

I thank to all my friends, who always supported me through the years.

Finally, I am specially grateful to my family for the *love*, support, and encouragement. I thank them for the pleasant and warm environment they created for me.



---

# Introduction

Prior to the 1990s, our understanding of how planets form was limited because we had observed only one planetary system, our own Solar System. Since then many extrasolar planets have been discovered and certainly many more are likely to be found in the upcoming decades. Various methods for detecting extrasolar planets are being used or investigated for future application. As the planets, circling round their host stars at greatest orbital distances were a difficult target for direct imaging, many indirect detection techniques were attempted at the dawn of the exoplanet quest. Using oblique methods, a planet is detected through its influence on the star that it orbits. As a result, each technique is sensitive to a specific class of planets, and provides us with some of the missing puzzle pieces from the picture of planetary systems diversity.

Historically, the pulsar timing technique provided the first confirmed detection of extrasolar planet (Wolszczan & Frail, 1992). Since the first Hot Jupiter discovery (Mayor & Queloz 1995), the radial velocity surveys have been so far the most successful method for detecting planets around main sequence stars. However, among all exoplanet finding techniques, the photometric detection of transits has played a fundamental role for our understanding of planet formation. When a planet passes periodically in front of the disk of its host star, it removes a small portion of starlight. This temporal variation in the star light curve enables astronomers to directly measure the size of the transiting body. A transit light curve, when combined with a radial velocity orbit, gives a direct access to the planet's mean density. Currently, the transit method is the only technique which provides

accurate measurements of radii, orbital inclinations and densities of planets, beyond our Solar System. The study of transiting extrasolar planets hence, bear upon our knowledge of the bulk composition and physical structure of these worlds and precisely constrain models of their formation (Charbonneau, 2008).

Since the first observation of HD 209458b, transiting its host star (Charbonneau et al. 2000; Henry et al. 2000; Mazeh et al. 2000) it became clear that exoplanetary transits provide a bunch of opportunities for follow-up studies of their nature. Spectroscopy during transits enable identification of several chemical species in the planetary atmosphere, an astonishing achievement that would sound as impossible just fifteen years ago. In addition, if precise enough, radial velocity measurements of the star during planetary transits provide important constrain on the alignment of the stellar spin with the planetary orbit. Furthermore, infrared photometry of secondary eclipses (a passage of the planet behind the star) have already permitted direct measurements of the planet thermal emission as well as the orbital eccentricity. Accurate measurements of the mid-transit epochs of known exoplanets disentangle the presence of additional (non-transiting) bodies in the system.

Perhaps one of the most exciting opportunities in the next few years would be an application of all mentioned techniques to study terrestrial planets, transiting M dwarf stars (Charbonneau & Demming 2007; Gaidos et al. 2007; Nutzman & Charbonneau 2008). Such planets circle their hosts at orbital distances permitting liquid water to exist on their surfaces (*habitable zone*) and present a tremendous opportunity for the emerging science of astrobiology. At the currently known orbital distances, Jupiter-like planets would transit M5V stars more frequently. The smaller radii and masses of M5V dwarfs in comparison with those for G2V stars translate into much larger photometric and radial velocity signals, hence easier to detect from the ground. Furthermore, M dwarfs are among the most widespread stars in the Galaxy.

My personal enthusiasm and motivation over transiting exoplanets is a consequence of their major scientific importance for astronomy. In this thesis I concentrate on observational studies, focused on (1) photometric detection and classification of transits; and (2) characterization of the WASP-4b transiting extrasolar planet. I have been developed and carried out the thesis based on the following approach:

In Chapter 1 I describe the transit method to detect extrasolar planets. I discuss astrophysical parameters that can be studied from observations of planetary transits and present a short description of the follow-up science, related to the characterization of



transiting planets.

Chapter 2 contains detailed discussion on the nature of the false positives (transit-like events, produced not by planets), detected by transit surveys. In addition, it describes three methods proposed for the identification of the false alarms in the Pan-Planets<sup>1</sup> project. Finally, I present results from the application of the three approaches to the OGLE<sup>2</sup> data set, which is similar to the LAIWO data, simulated Pan-Planets light curves as well as data from confirmed transiting planets.

In Chapter 3 I present first results based on a time series, obtained with the LAIWO wide-field camera in the Ophiuchus field. A detailed description of the data analysis process with all required steps for the production of high quality light curves is thoroughly presented. Moreover, I report the detection of new transit candidates and periodic variable stars along with additional analysis of their light curves. Finally, I propose a chain of steps for an efficient spectroscopic and photometric follow-up, which is required for the confirmation of our candidates.

In Chapter 4 I use a high quality optical and near-infrared (NIR) photometric data to study the astrophysical parameters of the WASP-4b transiting planet. Furthermore, I perform an analysis of the transit mid-times to investigate for deviations from the predicted ephemeris.

A conclusive summary and future perspectives of this research are presented at the end of the thesis.

---

<sup>1</sup>Pan-Planets is a photometric transit search program at MPIA, using the 2.0m PanSTARRS 1 telescope.

<sup>2</sup>OGLE-Optical Gravitational Lensing Experiment.



## Chapter 1

---

# Transiting Exoplanets

## 1.1 The method

An extrasolar planet that passes in front of the disk of its host star causes a periodic temporal decrease of the star brightness. Such a phenomenon is referred in astronomy as transit and grants us an extraordinary opportunity to discover and explore planets outside the Solar System (Figure 1.1). Transiting exoplanets can be observed when a number of specific conditions are satisfied.

First, transits are seen only by privileged observers, who view the planet's orbit nearly perpendicular to the celestial sphere or edge-on. If we consider a set of circular orbit planetary systems with a random orbital orientation with respect to the line-of-sight, the geometric probability ( $P_{transit}$ ) for any of the planetary systems to show a transit of its host is determined by

$$P_{transit} \approx \frac{R_*}{a}, \quad (1.1)$$

where  $R_*$  is the radius of the star and  $a$  is the planetary orbital radius. If we consider Jupiter transiting the Sun, the geometric probability to observe such an event would be  $P_{transit} \approx 1/1000$ , i.e. we must search about a thousand stars to find a single transit, if all stars host a planet.

Secondly, during a transit the planet blocks a small fraction of the starlight, because planets are considerably cooler than stars. The brightness variation of the host star is

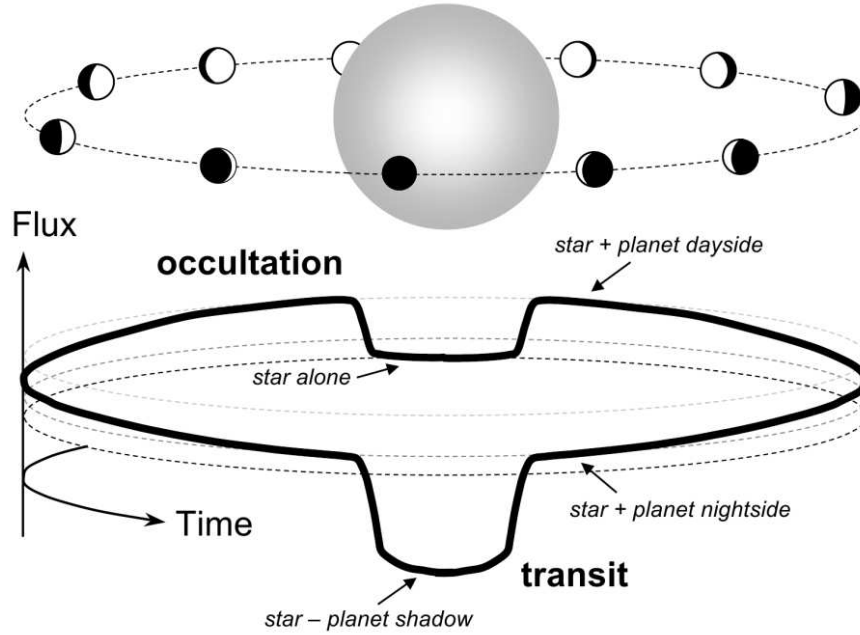


Figure 1.1 Illustration of transits and occultations, assuming observation of the combined flux from the star and the planet. While transiting, the planet blocks a portion of the starlight. Then the planet’s dayside comes into view. The flux decreases again when the planet is behind the star, (Winn, 2010).

proportional to the relative sizes of both objects and is given by

$$\delta F \approx \left( \frac{R_p}{R_*} \right)^2, \quad (1.2)$$

where  $R_p$  and  $R_*$  are the planet and star radii, respectively. The brightness variation is an important quantity, as it determines the photometric precision that should be attained to detect a transiting planet. Referring again to the example of Jupiter in the Solar System, the decrease of sunlight would be  $\delta F \approx 0.01$  mag or about 1%.

Third, certainly the detection of a transiting exoplanet depends on the duration of the event. For  $a \gg R_* \gg R_p$  the transit duration  $t_{transit}$  is given by the relation

$$t_{transit} \approx \frac{P}{\pi} \sqrt{\left( \frac{R_*}{a} \right)^2 - \cos^2 i}, \quad (1.3)$$

Table 1.1 Transit properties for the planets in the Solar System, if viewed by a distant observer.

#	Planet	Period [yr]	Probability	Duration [h]	Depth [mag]
1	Mercury	0.24	$1.2 \times 10^{-2}$	8	$1.2 \times 10^{-5}$
2	Venus	0.62	$6.4 \times 10^{-3}$	11	$7.6 \times 10^{-5}$
3	Earth	1.00	$4.7 \times 10^{-3}$	13	$8.4 \times 10^{-5}$
4	Mars	1.88	$3.1 \times 10^{-3}$	16	$2.4 \times 10^{-5}$
5	Jupiter	11.86	$8.9 \times 10^{-4}$	30	$1.1 \times 10^{-2}$
6	Saturn	29.46	$4.9 \times 10^{-4}$	40	$7.5 \times 10^{-3}$
7	Uranus	84.01	$2.4 \times 10^{-4}$	57	$1.3 \times 10^{-3}$
8	Neptune	164.79	$1.5 \times 10^{-4}$	71	$1.3 \times 10^{-3}$
9	Pluto	247.68	$1.2 \times 10^{-4}$	81	$2.7 \times 10^{-6}$

While moving on its present orbit, Jupiter would transit the Sun for about 30h, which is favorable for transit search surveys.

The three described parameters determine the chances for success of a transit search program. Table 1.1 lists their values computed for each planet of the Solar System. The numbers elucidate the main drawback a planet survey could face. If no knowledge is available for exoplanets, thousands of stars have to be monitored over a long time with precision high enough to permit a successful detection.

## 1.2 Transit surveys

The prospects for detecting exoplanets with the transit technique increased significantly after the detection of the first close-in extrasolar planet (51 Peg b), around a main sequence star (Mayor & Queloz, 1995). Although this exoplanet was roughly half the mass of Jupiter it was orbiting the host star once every 4.5 days. The first successful transit observation came in 1999 with HD 209458b (Charbonneau et al. 2000, Henry et al. 2000, Mazeh et al. 2000). However, the planet was initially detected with the radial velocity method, which measures velocity variations of the star along the line-of-sight due to the gravitational influence of a companion.

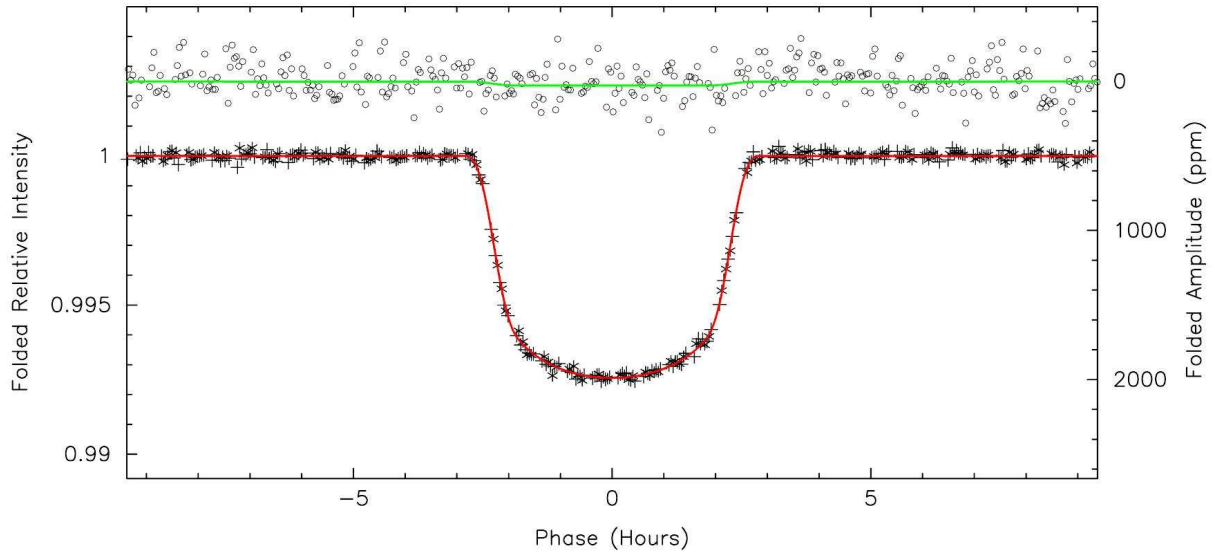


Figure 1.2 The light curve of Kepler-7, phase-folded by the period  $P = 4.885525$  days. The model fit to the transit is plotted in red and a secondary eclipse model is indicated with green (Borucki et al. 2010).

As the transit geometric probability for the 'Hot Jupiters' class of exoplanets is on the order of 10%, several groups undertook photometric search programs from the ground and from space (see Charbonneau et al. 2007 and references therein). Historically, the OGLE survey was the first to deliver planets detected from photometric transits (Udalski et al. 2002a, Konacki et al. 2003, Bouchy et al. 2004). Subsequent transit confirmations were announced later by the TrES (Alonso et al. 2004), XO (McCullough et al. 2006), HAT (Bakos et al. 2007) and the Super WASP (Collier Cameron et al. 2007) surveys. In addition, the CoRoT (Baglin et al. 2002) and KEPLER (Borucki et al. 2010) space crafts deliver transit detections and light curves of high quality (Figure 1.2). The annual rate of transit discoveries is reported on Figure 1.3.

Although, the transit method is strongly biased towards detecting planets with very short periods, it is currently the only opportunity to increase our knowledge for the bulk composition of planets outside the Solar System. Photometric transit light curves provide estimations of the planetary radii and orbital inclinations. This permits planetary mass estimates from radial velocity curves and hence, a derivation of the planetary mean

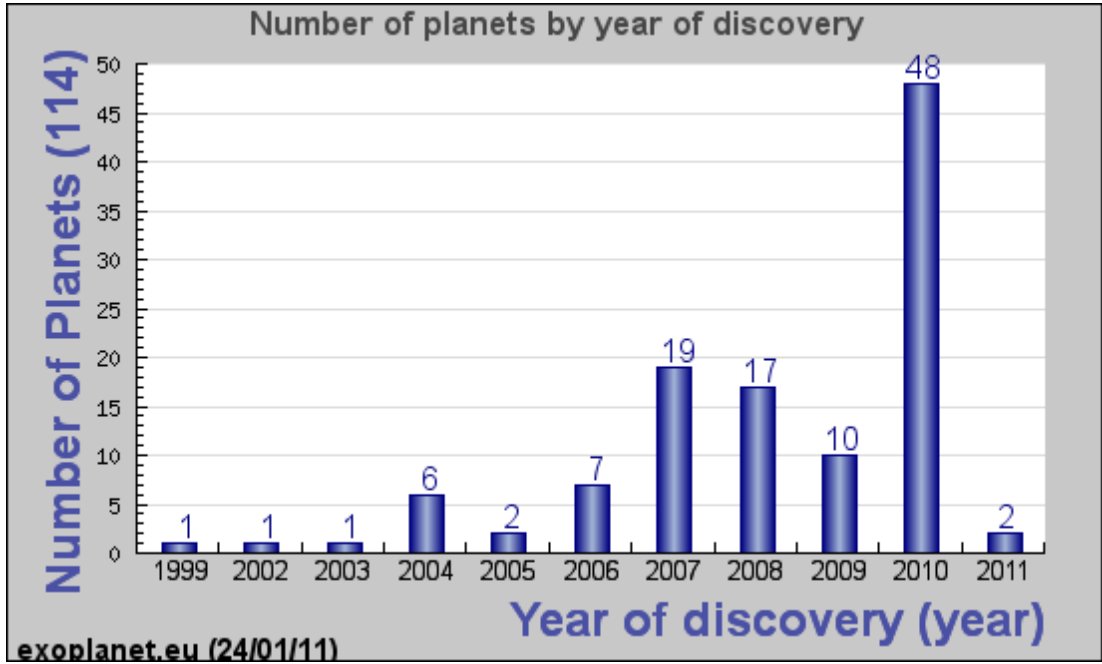


Figure 1.3 Histogram of the number of transiting exoplanet discoveries as a function of the year (as of 24 January 2011). Prior to 1995 no transit searches were performed as the hot Jupiter class of exoplanets was unknown. Presently, ground based and space based transit surveys report planet confirmations with an average rate of  $\sim 10$  planets per year.

densities. Figure 1.4 displays the current observational mass-radius diagram for the known transiting planets, which is of fundamental importance for the theory of planet formation, providing constraints for its models.

The transiting planets confirmed to date have been detected using two different approaches: (1) photometry of wide fields, using small size telescopes or photographic lenses (apertures  $< 20\text{cm}$ ), monitoring stars down to  $V = 12$  mag; and (2) narrow field, deep photometric transit searches, using telescopes with size  $> 1\text{m}$  and stars fainter than  $V = 13$  mag. In both cases the transit surveys attempt to identify stars which exhibit short period ( $\sim 1 - 5$  day) small variations ( $\sim 1 - 2\%$ ) in their light curves with the appropriate U-shape. However, there can be several cases of astronomical objects that can produce such signals: eclipsing binary stars, viewed at high inclinations (grazing eclipsing binaries); transits of small stellar companions, such as M-dwarfs or brown dwarfs in F-M eclipsing binary systems; eclipsing binaries blended with a foreground/background star or

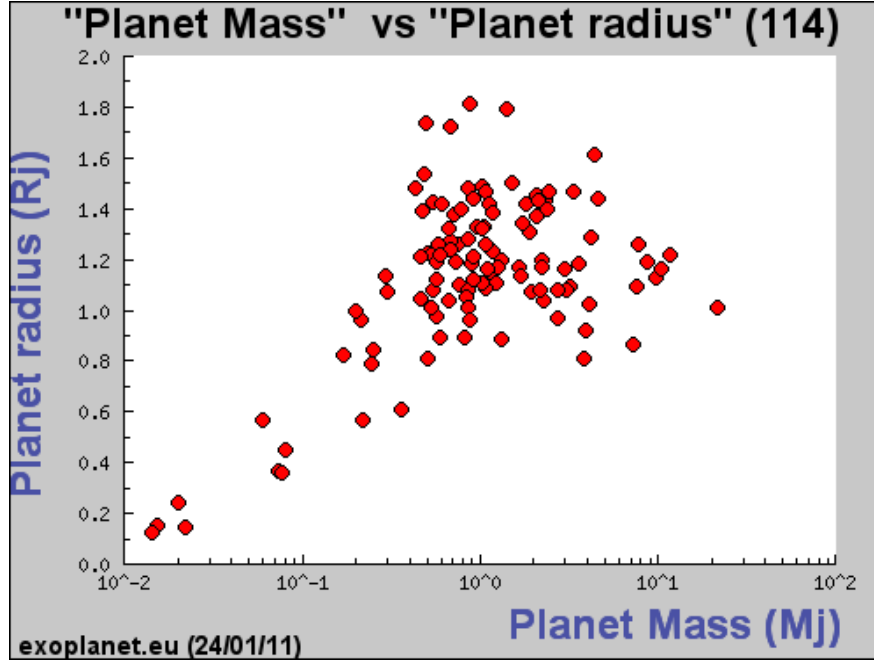


Figure 1.4 Observational mass-radius diagram, based on the confirmed planets detected with the transit method (as of 24 January 2011).

finally, a statistical false positive, caused by instrumental effects, variations in the observing conditions or photometric calibration errors (Moutou et al. 2006). The main impostors are discussed in detail in the next chapter of this thesis along with several methods to disentangle their nature.

### 1.3 Science from transiting exoplanets

The transiting extrasolar planets grant us a special opportunity to study their nature. Presently, the transit observations are the only way to measure accurate sizes, densities and dynamical parameters, such as orbital distances, inclinations and eccentricities of planets beyond the Solar system. The transiting exoplanets allow direct investigations of the dynamics and chemistry of their atmospheres and therefore, provide the first insights on the habitability of alien planets. We provide a short description of the important techniques, which enable transit follow up studies.



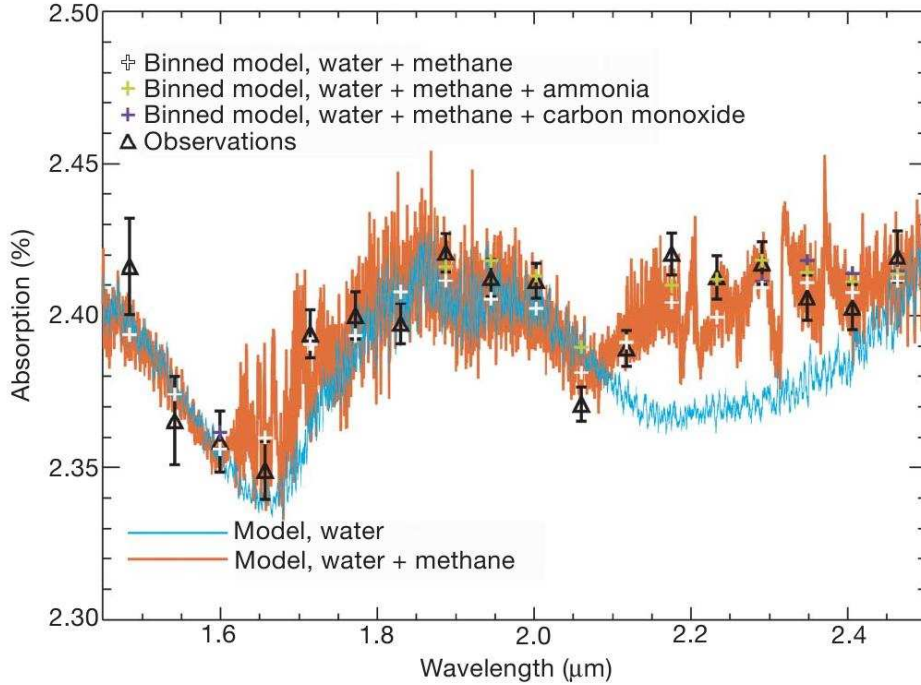


Figure 1.5 A comparison of observations with simulated water and methane absorption lines for the transiting exoplanet HD 189733b. The spectrum is an evidence for the presence of water ( $\sim 1.9\mu\text{m}$ ) and methane ( $\sim 2.2\mu\text{m}$ ) in the planet's atmosphere (Swain et al. 2008).

### 1.3.1 Transmission spectroscopy

Gas giant planets do not have a sharp edge of their silhouette. Therefore, when a planet transits a star, part of the starlight is filtered through the upper planetary atmosphere. The filtered light is also partially absorbed, depending on the scattering properties of the atoms and molecules present in the planetary atmosphere. Measurements of the spectral features in transiting exoplanets at different wavelengths provides information for the composition of their atmospheres.

Using the transmission spectroscopy technique, Charbonneau et al. (2000) confirmed the presence of sodium ( $Na$ ) in the atmosphere of HD 209458b, predicted earlier by Seager & Sasselov (2000). It has been later proposed that the spectral signatures of water ( $H_2O$ ), methane ( $CH_4$ ) and carbon monoxide ( $CO$ ) may be able to be detected in this way as well.

Swain et al. (2008) obtained infrared spectra (1.5 and 1.3 microns using NICMOS/HST) of the transiting extrasolar planet HD 189733b and confirmed the presence of the expected molecules (Figure 1.5).

### 1.3.2 Occultation spectroscopy

Nearly half an orbital period after a transit, the planet goes behind the star, causing a small decline of the starlight, known as a secondary eclipse or occultation (Figure 1.6). The missing portion originates from reflected light and thermal emission produced by the planet. Observations bracketing occultations thereby reveal the relative brightness of the planetary disk. Thermal emission measurements (1) constrain the temperature-pressure profile of exoplanetary atmospheres (Fortney et al. 2008); (2) provide a better estimate of the bolometric luminosity of the planets' dayside emission; and (3) provide evidences for the heat transport mechanism from the planetary day to nightside at variety of depths and pressures in their atmospheres (Barman 2008). In addition, the timing and duration of the secondary eclipses place constraints on the orbital eccentricity that are much more restrictive than those from the radial velocity orbit alone (Charbonneau et al. 2005).

### 1.3.3 Rossiter-McLaughlin effect

While transiting, extrasolar planets affect not only the brightness of the host star, but also the shape of their spectral lines. The effect is a consequence of the star rotation. Each point of the stellar surface contributes to the stellar spectrum with its own one, blue-shifted or red-shifted depending on its line-of-sight velocity component. When the planet transits, it removes a portion of the stellar surface, and therefore the corresponding velocity components. This causes successive variations in the blue-shifted and red-shifted wings of the spectral lines similar to those produced by star spots. The phenomenon is referred as "Rossiter-McLaughlin effect", after the names of the two astronomers who describe it (Rossiter 1924, McLaughlin 1924) although, the effect had been observed earlier in spectroscopic studies of eclipsing binary stars (Forbes 1911, Schlesinger 1911). Figure 1.7 illustrates the effect.

Precise spectroscopic measurements during planetary transits permit estimation of the

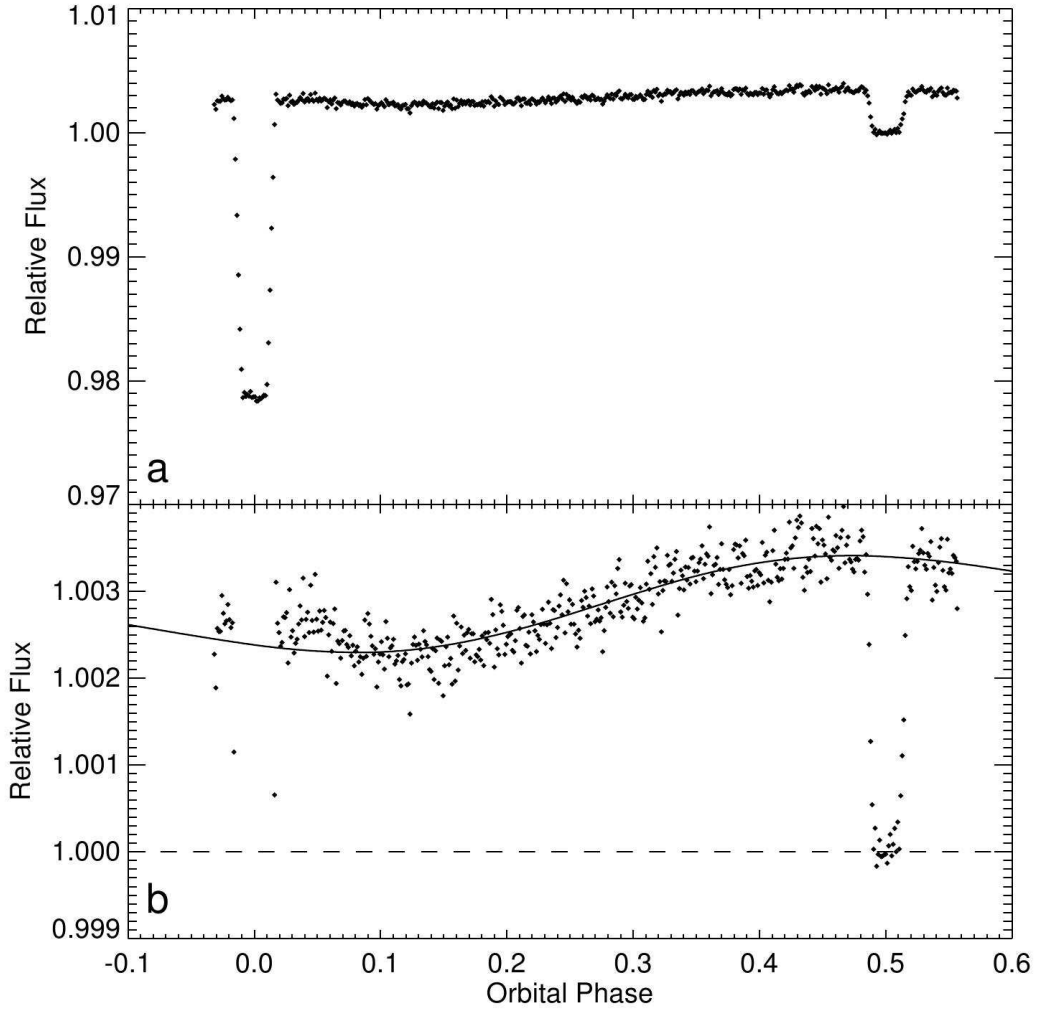


Figure 1.6 The combined  $8\mu\text{m}$  observations of the K-star HD 189733 and its planet, including a transit and a secondary eclipse. The bottom panel shows the same data as the top panel but the range of the vertical scale was chosen to highlight the gradual rise in brightness as the planet's dayside contributes to the starlight. The measured amplitude of this variation gives the temperature contrast between the dayside ( $\sim 1211 \pm 11$  K) and the nightside ( $973 \pm 33$  K) (Knutson et al. 2007).

line-of-sight component of the stellar equatorial rotation velocity and the angle on the sky between the stellar rotation axis and the planetary orbital axis (spin-orbital alignment).

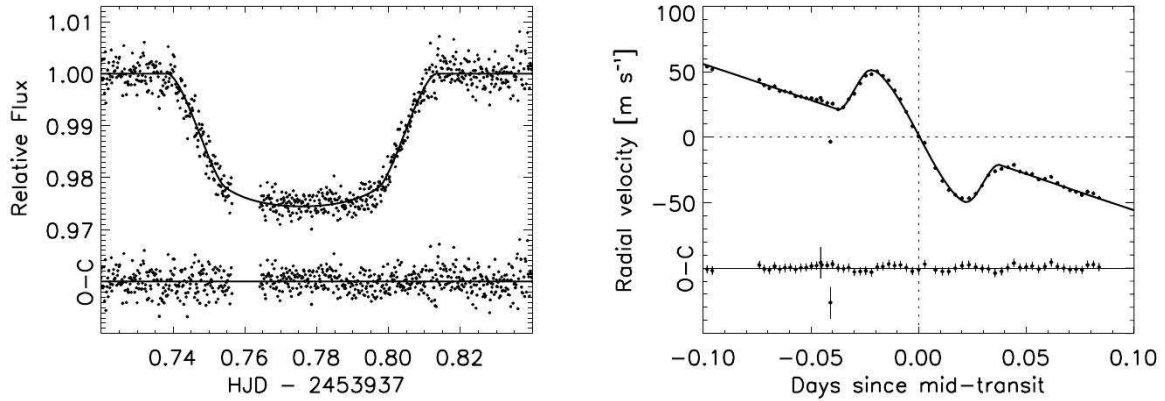


Figure 1.7 The photometric and spectroscopic transit of HD 189733, from Winn et al. (2006). The photometry (in the Sloan  $z$ -band) was obtained with the 1.2m telescope at the Fred L. Whipple Observatory. Radial velocity measurements were performed after obtaining spectra with the HIRES instrument on the Keck I 10m telescope.

### 1.3.4 Eclipse timing

The time interval between successive transits or secondary eclipses (occultations) of a single planet around a star (unperturbed planet) is always a constant number. It is equal to the planetary orbital period. However, the presence of a second planet, orbiting the star could cause variations in the eclipse/occultation times of the transiting planet (and vice versa).

The transit timing variations (TTVs) method is based on the dynamical interactions within the system. It allows inference of the orbital elements and the mass of the perturbing planet, down to sub-Earth masses. The method is particularly sensitive to small trapped planets in resonant configurations. For an Earth-mass perturber in 1:2 mean motion resonance with a 3 day period transiting Jupiter-mass planet, the TTV is about 3 min (Agol et al. 2005).

Holman et al. (2010) performed an analysis of photometric data, obtained with the Kepler spacecraft and detected the first system of multiple planets transiting a Sun-like star (Kepler-9). At the time of the discovery both objects were observed with 19.2- and 38.9-day periods, increasing and decreasing at respective average rates of 4 and 39 minutes per orbit. Figure 1.8 shows the TTVs for the Kepler-9 planetary system.

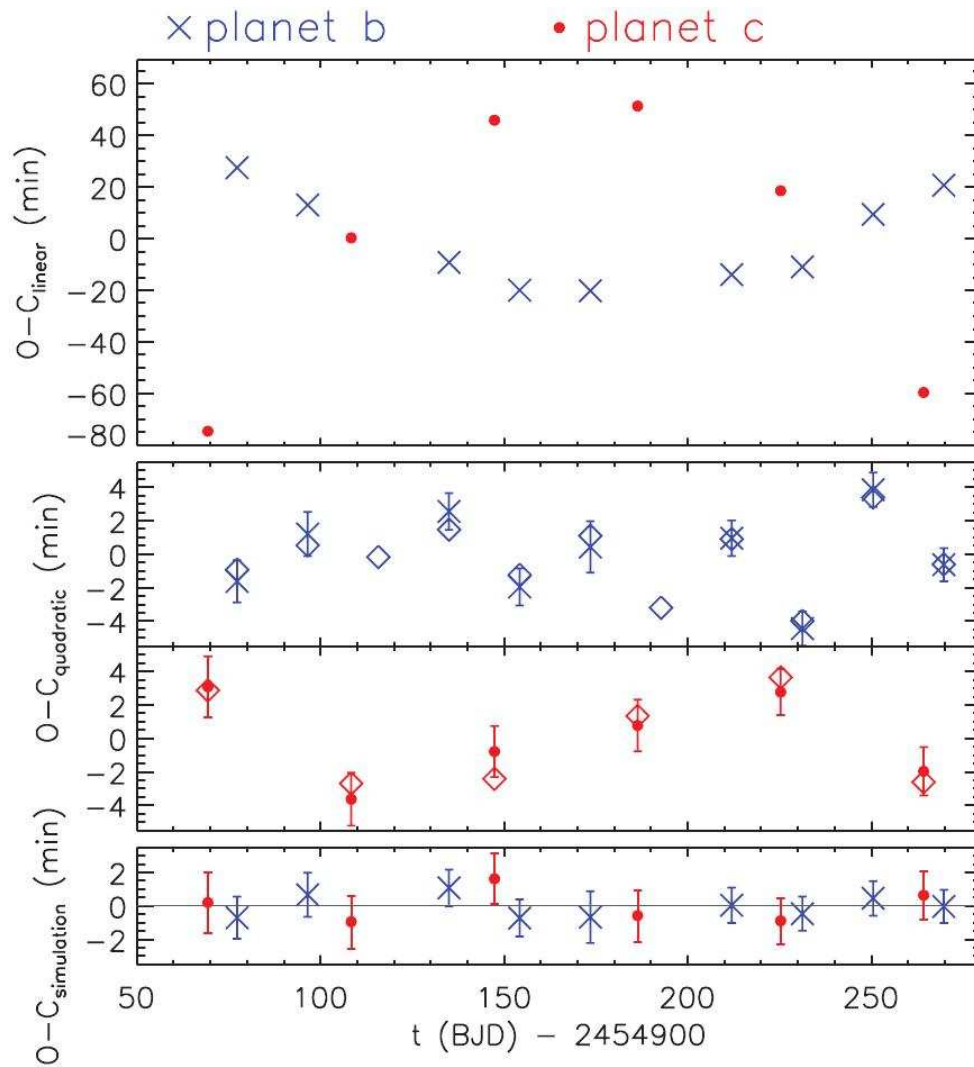


Figure 1.8 Deviations of the observed transit times for the Kepler-9b (blue  $\times$  symbols) and Kepler-9c (red dot symbols), compared to the calculated ephemeris, Holman et al. (2010). The top panel refers to linear, the middle to a quadratic and the lower to a dynamical model in which the two planets fully interact. The diamond symbols refer to transit times for which Kepler data was not available (Holman et al. 2010).



## Chapter 2

---

# Transit False Alarms

## 2.1 Introduction

Not every light curve, that looks like a transit is produced by a planet passing in front of its host star. Several combinations of stellar systems can mimic transit shapes that are similar to those caused by real transiting planets. The impostors become more indistinguishable when the data contains a signal, which amplitude is of the order of the noise level. The most expected cases of false alarms or false positives for a ground-based transit search are described by Brown (2003) and they include:

### 2.1.1 Eclipsing binary stars

The light curve of an eclipsing binary can be confused by that of a regular transiting planet in the following two cases:

- When the radius ( $R_1/R_2$ ) and the temperature ( $T_1/T_2$ ) ratios for the components of an eclipsing binary is such that the system produces change of the observed flux  $\sim 1\%$  during the primary eclipse. Indeed, some binaries containing main sequence stars can satisfy this condition (see Table 2.1 based on the data of Cox 2000). Of particular interest are the pairs of F and M stars, since they are the most numerous stars present in a typical ground-based transit survey. Moreover, such systems produce secondary eclipses which are one order of magnitude smaller than the primary eclipses and

Table 2.1 Maximum flux drop (in %) for combinations of main-sequence stars. The computation is based on radii and effective temperatures from Cox (2000).

	A0	A5	F0	F5	G0	G5	K0	K5
M0	6.24	12.38	15.81	20.81	28.28	38.78	43.18	49.63
M2	4.34	8.62	11.04	14.62	20.15	28.20	32.17	40.33
M5	1.27	2.52	3.24	4.30	6.00	8.54	9.95	13.55
M8	0.17	0.35	0.44	0.59	0.83	1.18	1.38	1.92

therefore, cannot be detected and used as a signature for the presence of a massive secondary.

On the other hand, a Jupiter-like transit can be mimicked by a stellar binary when a hydrogen burning star is accompanied by a more evolved companion, that has started a post main sequence stage, i.e. increased its radius.

- If the impact parameter  $b = (a/R_*) \cos i$ , where  $a/R_*$  is the normalized planet orbital semi-major axis and  $i$  the orbital inclination, is in the range  $R_1 - R_2 \leq b \leq R_1 + R_2$ , the secondary ( $R_2$ ) will partially eclipse the primary ( $R_1$ ). Such a stellar system produces shallow V-shaped transits, which in a light curve with relatively low signal-to-noise ratio can easily be mistaken as due to a planetary transit.

### 2.1.2 Multiple systems

The depth of the primary and the secondary eclipses of a stellar binary can be diluted by the light of a third star. The third object can be bound in the system (hierarchical system) or, can be just a blending star, which is not physically attached, projected at an angular distance of about one Full Width at Half Maximum (FWHM) of the Point Spread Function PSF and to be indistinguishable. We identify such configuration as a blend. In the next section, we explain some techniques that can be applied to reveal the nature of such systems.



## 2.2 Morphological analysis of the light curves

A careful inspection of the transit shape and the out-of-eclipse parts of the light curve of a transit candidate can identify a false positive. That is the fastest and the cheapest way to rule out impostors without using radial velocity follow-up, which is time consuming, however a requisite for the confirmation of the planetary nature, and for the identification of some hard to identify cases of false positives.

### 2.2.1 Inspection of the out-of-eclipse parts.

#### Detection of ellipsoidal variability

It is a well-known fact that nearly half of the stars we see on the night sky belong to double or multiple systems and hence, significant part of the eclipses detected in a transit survey should be produced by stellar binaries.

When two stars exist in a tight physical binary, their gravitational potentials stretch the envelopes of each companion in ellipsoids (von Zeipel 1924). The rotating stellar configuration generates sinusoidal modulations, similar to these observed in the light curves of *W* UMa binary systems. The brightness of an eclipsing binary depends on the luminosities and the cross sections of the two components. The local effective temperature  $T_g$  acts in proportion to the gravity ( $g$ ) such that

$$T_g \propto g^\beta, \quad (2.1)$$

where  $\beta$  is a constant, determined according to whether radiative ( $\beta = 0.25$ ) or convective ( $\beta = 0.08$ ) equilibrium is maintained. It is clear that the gravity darkening/brightening<sup>1</sup> depends on the constant  $\beta$ .

The sinusoidal modulation, due to the ellipsoidal shape of the stars varies twice per orbital period, and is a tracer for the mass of the companion, no-matter if it is seen or not. Moreover, the ellipsoidal variability can be observed at very wide range of orbital inclinations even if an eclipse does not occur in general, as observed for first time in the light curve of  $\pi^5$  Orionis (Stebbins 1920). Furthermore, if both stellar companions have

---

<sup>1</sup>both terms relate to the same physical phenomenon

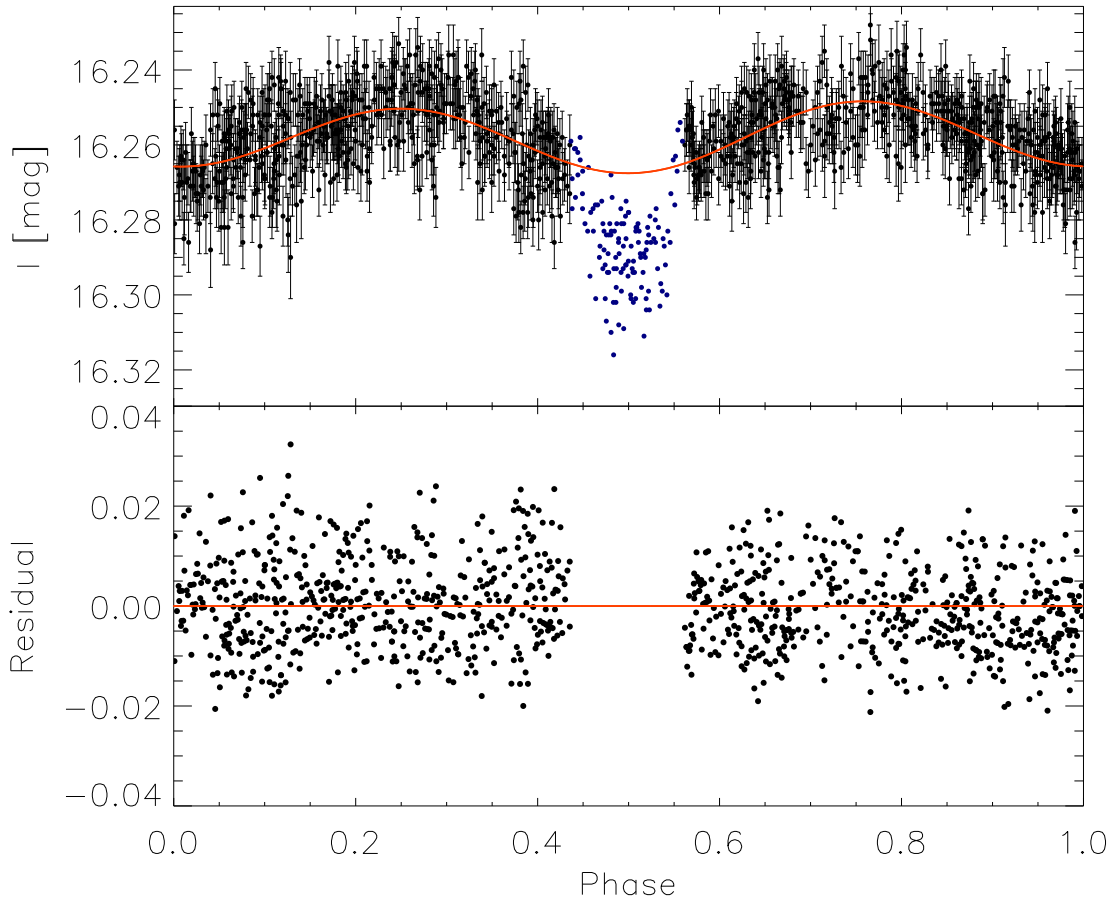


Figure 2.1 Phase-folded light curve and residual for the transit candidate OGLE-TR-61, showing ellipsoidal variability of  $\sim 1\%$ . The filled squares were removed in order not to influence the estimated ellipsoidal amplitude toward higher values. The red line in the upper panel is the fitted function (see the text).

similar luminosities a reflection effect can cause light changes twice per orbital period with maximum at the secondary eclipse.

Using eclipsing binary simulators (such as the program *Nightfall*<sup>2</sup>), it can be shown that secondaries with masses  $\geq 0.2 M_{\odot}$  produce baseline luminosity variations  $\geq 0.5\text{mmag}$ , for orbital periods longer than 2 days (Drake 2003). Therefore, detection of greater

<sup>2</sup>see <http://www.hs.uni-hamburg.de/DE/Ins/Per/Wichmann/Nightfall.html>

amplitudes of sinusoidal modulations would be sufficient to identify transits due to a stellar companion. On the other hand, Pont et al. (2005) showed that the ellipsoidal variation due to a Jupiter-like planet is in the  $\mu\text{mag}$  domain and hence, undetectable with the modern transit survey resources from the ground.

We have implemented a tool that automatically estimates the out-of-eclipse ellipsoidal variations and we intend to apply it for the Pan-Planets transit candidates. Our approach is based on the work of Drake (2003) and Sirko & Paczyński (2003), who used the method for the first time to select the most promising transit candidates in the released lists of OGLE planet candidates (Udalski et al. 2002a, Udalski et al. 2002.b, Udalski et al. 2003). We followed their methodology and obtained all light curves from the database of the OGLE team.<sup>3</sup>

Typically, every candidate contained between 800 and 1500 photometric measurements in the I band with accuracy of 1.5 %. We phase folded all light curves with the most current period. Candidates OGLE-TR-43 to OGLE-TR-46 do not have derived periods, and therefore they were not included in the analysis. Simple visual inspection of the rest of the candidates showed that approximately 95% of all data points lie in the out-of-eclipse baseline magnitude. Those points are of little or no use for the determination of the planet's size or shape. However, they are reliable for a very accurate evaluation of the degree of sinusoidal modulations due to tidal distortions.

In order to estimate correctly the amplitude of the ellipsoidal variability we removed all photometric measurements in the transit. Their presence would bias the measured amplitudes towards higher values. The absence of ellipsoidal variability would result in a relatively constant baseline magnitude out of the transit.

Our algorithm was to start at the mid-eclipse of each candidate, working outward, and to reject data points until the third data point for which the baseline magnitude was within its photometric errorbar. The further analysis is practically a repetition of what was done in the past on binary stars showing ellipsoidal variability. We performed an analytic five parameter least squares fit with a model of the form:

$$I_k = \langle I \rangle + a_{c1} \cos p_k + a_{s1} \sin p_k + a_{c2} \cos 2p_k + a_{s2} \sin 2p_k, \quad (2.2)$$

---

<sup>3</sup><http://ogle.astrouw.edu.pl/>

where  $I_k$  is the apparent magnitude of data point  $k$  and  $p_k$  is the phase, computed with the correct period. The coefficients in front of the *sin* and the *cos* functions take care for

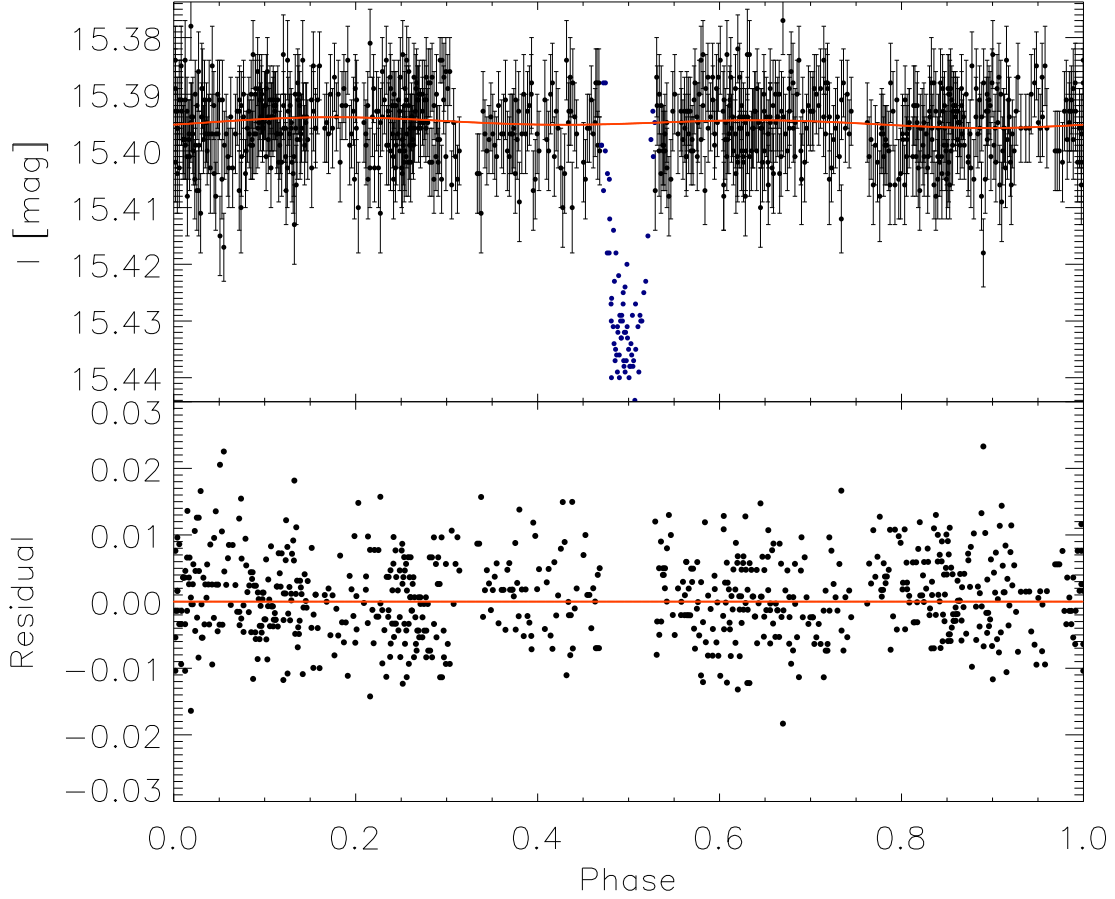


Figure 2.2 The light curve and residual for the transit candidate OGLE-TR-41. The filled squares were removed in order not to influence the estimated ellipsoidal amplitude toward higher values. The red line in the upper panel is the fitted function (see the text).

the different out-of-transit light modulations. The most dominant of them are  $a_{c2}$  and  $a_{c1}$ , which represent the ellipticity (due to surface gravity) and the reflection (or 'heating') effects respectively. The other two parameters ( $a_{s1}$  and  $a_{s2}$ ) account for spot activity and their values usually are close to zero.

The result of our analysis confirmed once again the conclusion of Drake (2003) and Sirko & Paczyński (2003) that the ellipsoidal variability is present in a significant fraction

of the OGLE light curves. In fact 83 of the 173 candidates, i.e.  $\sim 50\%$  of all candidates can be rejected due to the presence of a stellar companion. The results of our implementation are in a good agreement with those of Sirko & Paczyński (2003), see Figure 2.3 and 2.4. On Figure 2.1 and 2.2 we present two light curves respectively, showing ellipsoidal variability (OGLE-TR-61) and almost zero out-of-transit variation (OGLE-TR-41).

Alonso et al. (2004) used the same approach to select the best transit candidates for the STARE survey. They concluded that 13 of 16 candidates can be eliminated, because of significant out-of-transit sinusoidal modulation.

The result that many of the detected transits are due to eclipsing binaries should not be accepted as unusual. It is well-known that a large fraction ( $\sim 50\%$ ) of the stars we see on the night sky belong to binary or multiple systems and hence, a significant part of the eclipses detected in a transit survey should probably be due to such objects. The method of ellipsoidal variability detection is currently the only way to select candidates based on the mass and using photometry alone. Therefore, it is the most reliable one. All other methods (see next sections) attempt to evaluate the size of the transiting body. However, the photometry alone cannot unambiguously distinguish between Jupiter-size planets and other low-luminosity objects: brown dwarfs and late type M dwarfs, as all of them have similar radii of  $0.1\text{-}0.2\text{ R}_{\odot}$  ( $1\text{-}2\text{ R}_{Jup}$ ).

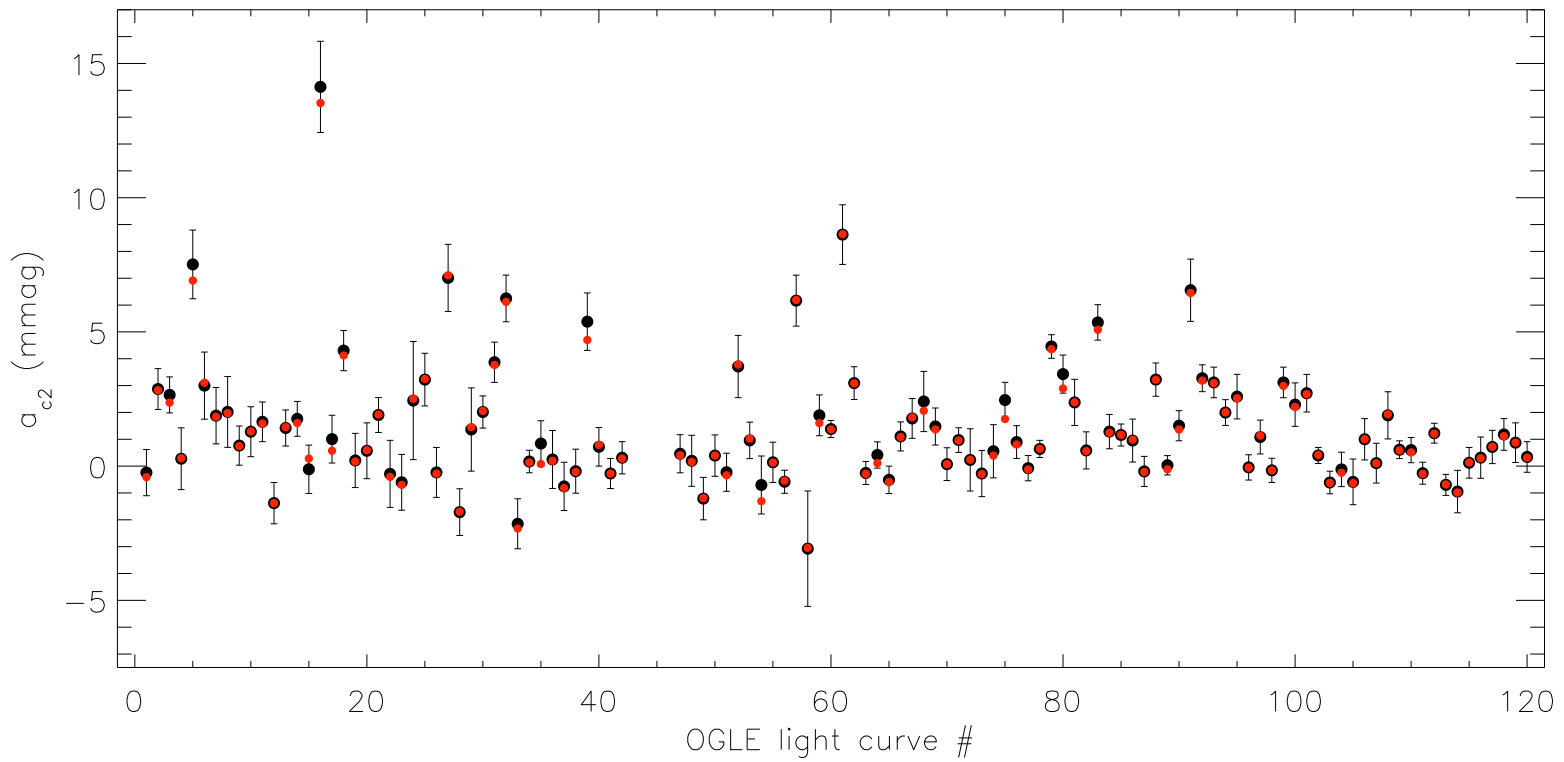


Figure 2.3 Comparison of the parameter  $a_{c2}$  obtained from our implementation (red dots) and the result of Sirko & Paczyński (2003) (black dots with error bars). Up to  $\sim 50$  % of the OGLE candidates may have significant ellipsoidal variability, indicating the presence of massive (not planetary) companion.

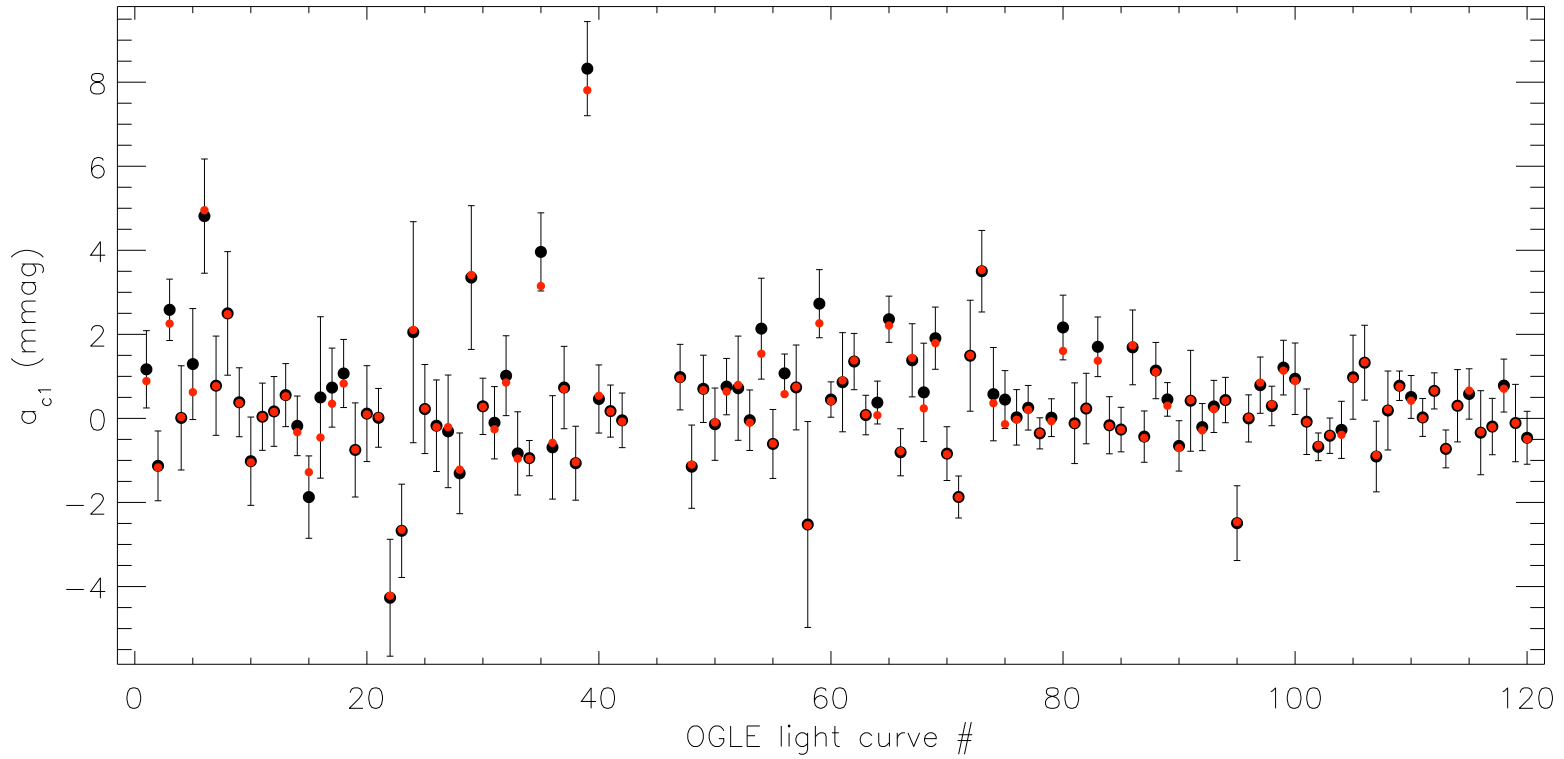


Figure 2.4 Same as Figure 3.2, but for the parameter  $a_{c1}$ . The big value of this coefficient is indicative for possible reflected light of the companion's hemisphere facing the primary. OGLE-TR-39 is the only object in the list showing the effect most significantly. The results produced by our implementation (red dots) is again in very good agreement with those (black dots with error bars) of Sirko & Paczyński (2003).

### 2.2.2 Inspection of the transit shape

Based on the transit light curve, i.e. without any additional color or spectroscopic information, it is still possible to estimate some stellar and planetary parameters, which can be used to distinguish between transiting extrasolar planets and false alarms. The shape of the light curve can be used for such analysis and therefore, a good photometric precision (1% or better) and a high time sampling (or well-covered phase-folded light curve) must be achieved.

Seager & Mallén Ornelas (2003) presented a unique analytical solution for the planet and star parameters, derived only from the transit light curve. The determination requires several assumptions for the host star and the transiting planet, as well as for the produced light curve. The planet ( $m_p \ll M_*$ ) must be on a circular orbit around an unblinded main sequence star. When transiting the stellar face, the planet must be entirely superimposed, which means that the observed light curve should have a flat bottomed shape.

The most important application of the unique solution is the determination of the mean density of the extrasolar planet host star ( $\rho_*$ ). It can be derived unambiguously from the transit light curve alone (see equation 2.3). No further information (color or spectroscopic) is needed or an assumption such as a stellar mass-radius relation.

$$\rho_* = \left( \frac{4\pi^2}{P^2 G} \right) \left\{ \frac{(1 + \sqrt{\delta F})^2 - b^2 [1 - \sin^2(t_{\text{transit}}\pi/P)]}{\sin^2(t_{\text{transit}}\pi/P)} \right\}^{3/2} \quad (2.3)$$

All transit observables included in equation (2.3): period ( $P$ ), transit duration ( $t_{\text{transit}}$ ) and transit depth ( $\delta F$ ), must be accurately measured from a fit to the light curve. The mean density of the host star is a selection criterion for the best transiting candidates for radial velocity follow-up. We point out the three most significant aspects:

- Giant stars have typical values for  $\log(\rho_*/\rho_\odot) \leq -1.5$  and occupy a specific position on the stellar density  $\rho_*$  vs. star mass ( $M_*$ ) diagram (see Figure 2.5). A measured stellar density from the light curve alone makes it possible to distinguish between a main sequence star and a giant. Hence, the light curves produced by a giant star with an eclipsing main sequence companion can be identified.
- The knowledge of the stellar density is a proxy to the stellar size to first order ( $R_*$ ),



since several tables relate both quantities (see for example Cox 2000). The star radius can be combined with the transit depth ( $\delta F$ ), derived from the light curve fit and the planetary radius ( $R_p$ ) can be evaluated.

- A possible false positive candidate can be rejected by comparing  $\rho_*$  derived from the transit light curve with  $\rho_*$  derived independently (for example, from spectral information). If both densities differ then something is amiss with the physical assumptions made for the derivation of equation (2.3).

The accurate computation of the mean density of the host star requires a robust tool that measures the observables from the light curve of every candidate. We have designed, implemented and tested a transit fitting program, for the specific needs of the Pan-Planets data. Our tool analyses automatically all light curves and outputs all requisite transit parameters.

The relative stellar flux as a function of the projected separation of the planet and the star was computed employing the analytical transit models of Mandel & Agol (2002). In the derivation of those equations we assume a dark planet moving on a circular orbit around the star, which is reasonable since circular orbits are expected for short-period planets as a result of their short tidal circularization timescale. In fact, most of the currently known short-period transiting planets have eccentricities consistent with zero.

The transit models of Mandel & Agol (2002) are generally parameterized by the planet to star size ratio ( $p = R_p/R_*$ ) and the normalized planet to star distance ( $z$ ). The later quantity is related to the times from the center ( $t$ ) of the transit by the following relation:

$$z = (a/R_*) [(\sin \omega t)^2 + (\cos i \cos \omega t)^2]^{1/2}, \quad (2.4)$$

where  $\omega$  is the orbital frequency ( $\omega = 2\pi T/t$ ),  $a/R_*$  is the normalized semi-major axis and  $i$  is the orbital inclination. As the computation of the normalized planet to star distance requires the orbital period ( $P$ ) and the mid-transit time ( $T_0$ ), their values must be known.

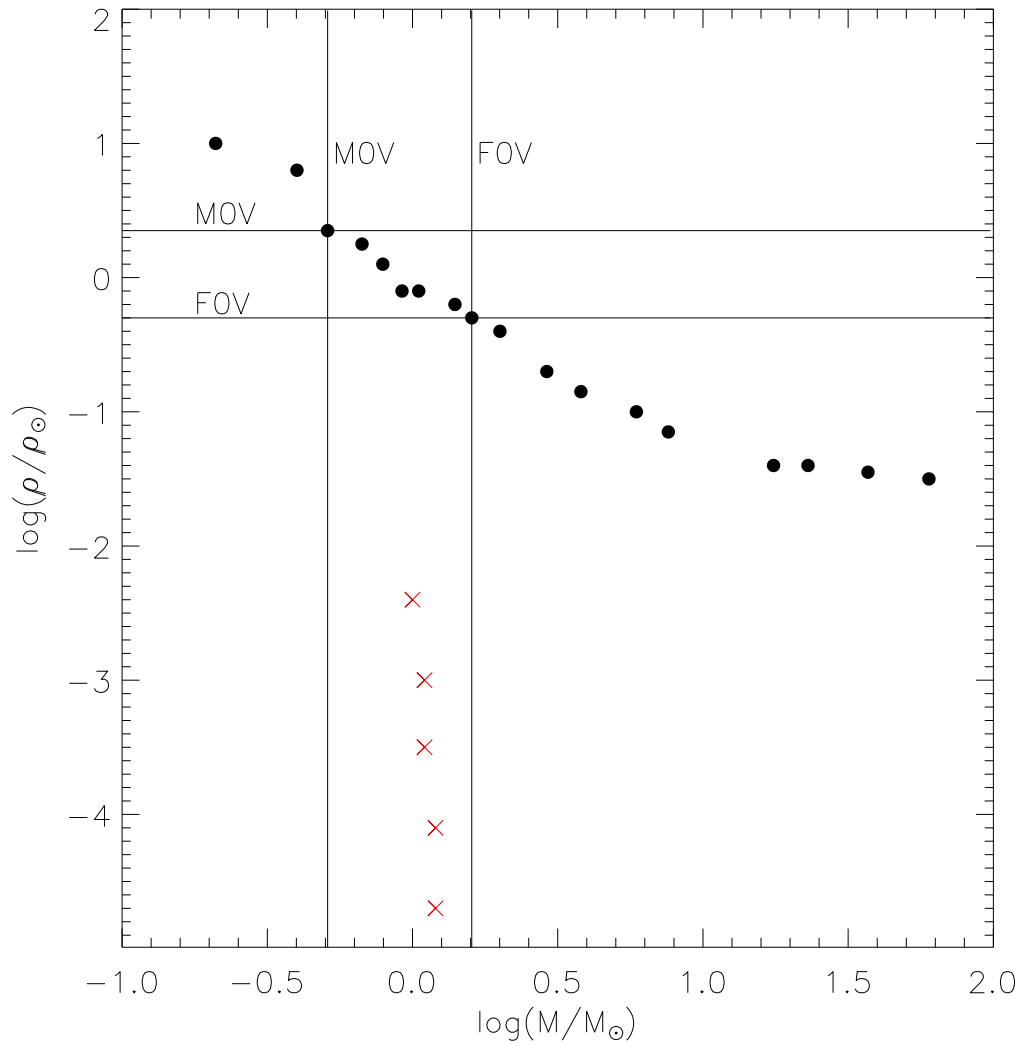


Figure 2.5 Stellar density-mass ( $\rho_*$  vs.  $M_*$ ) diagram based on the tables in Cox 2000. The black dots represent main sequence and the red crosses giant stars. The box F0V-M0V shows the main sequence stars that are mainly monitored by transiting planets surveys. The mean density of the main sequence stars is clearly distinguishable from that for the red giants below.

The modeling of the stellar limb darkening in earlier ground-based transit studies showed that the quadratic law is an adequate approximation. Therefore, we also selected to implement it in our models:

$$\frac{I_\mu}{I_1} = 1 - u_1(1 - \mu) - u_2(1 - \mu)^2 \quad (2.5)$$

where  $I$  is the intensity of the star and  $\mu$  is the cosine of the angle between the line-of-sight and the normal to the stellar surface. In all our fitting approaches we fixed the two limb darkening coefficients ( $u_1$  and  $u_2$ ). To determine their values we used the grid, computed by Claret (2004) for various stellar parameters ( $T_{eff}$ ,  $\log g$  and  $[Fe/H]$ ). In the absence of any additional information (such as photometric colors or spectra), constraining the limb darkening coefficients, we used solar-like values.

We choose the selection of the best transit model through the minimization of the  $\chi^2$  statistic:

$$\chi^2 = \sum_{i=1}^n \left[ \frac{f_i(obs) - f_i(calc)}{\sigma_i} \right]^2, \quad (2.6)$$

where  $f_i(obs)$  is the observed flux,  $\sigma_i$  is the corresponding photometric uncertainty and,  $f_i(calc)$  is the calculated analytic flux.

Before measuring transit observables from the light curve, our tool requires some initial data preparation. First, the brightness of the star has to be converted to normalized flux. The times of the observations must be phase folded with the known period and converted to times before and after the mid point of the transit. The value for the planet to star size ratio ( $p$ ) is the only initial guess.

For each set of data, period, limb darkening coefficients and initial guess for the planet to star size ratio, our utility computes a maximum and a minimum limits for the normalized semi-major axis, using Kepler's third law and a mass-radius relation. The range of  $a/R_*$  is then divided into sub-values and for each of them the tool assigns a range of inclinations. For every value the inclination corresponding to the smallest  $\chi^2$  statistic is selected. At this point we have a range of normalized semi-major axis with selected inclinations. We then select the pair  $a/R_*$  and inclination, minimizing our statistic at this point. Then we fix the two selected parameters and minimize  $\chi^2$  by varying the normalized planet to star size ratio. The described procedure iterates until the condition for the minimum used step is maintained.

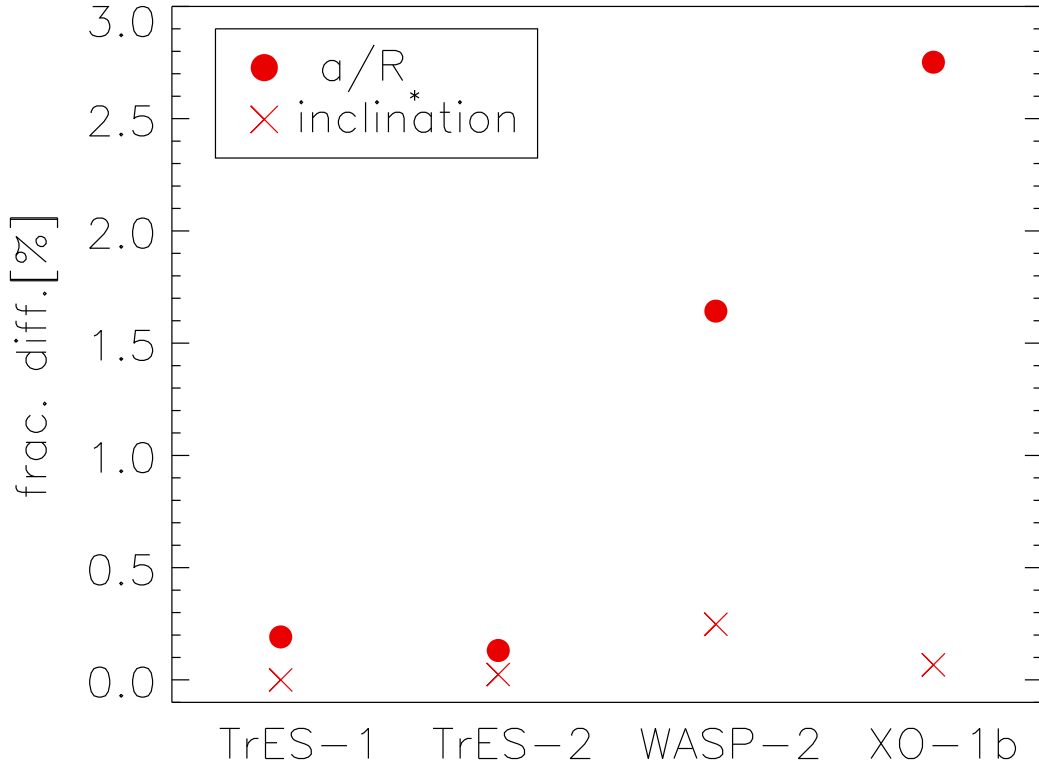


Figure 2.6 Fractional difference of the normalized semi-major axis  $a/R_*$  and the inclination  $i$  inferred from our modeling and that of the earliest papers related to the data.

To test the quality of our tool, we obtained four high-accuracy (photometric uncertainties  $\sim 0.2\%$ ), high-cadence transit light curves, acquired from the ground<sup>4</sup> and the related papers. Three of the four sets of data were measured within the Transit Light Curve project (Winn et al. 2007, Holman et al. 2006 and Holman et al. 2006) and the fourth one is a precise radius estimation of WASP-2b (Charbonneau et al. 2007). All data sets and the uncertainties in the fitted parameters were modeled with advanced methods (such as MCMC<sup>5</sup>), as described in the papers. We judged the efficiency of our implementation by comparison of our results with those produced by high-quality dedicated tools. The difference between the results is shown on Figures. 2.6 and 2.7.

<sup>4</sup>see <http://nsted.ipac.caltech.edu/>

<sup>5</sup>Markov Chain Monte Carlo

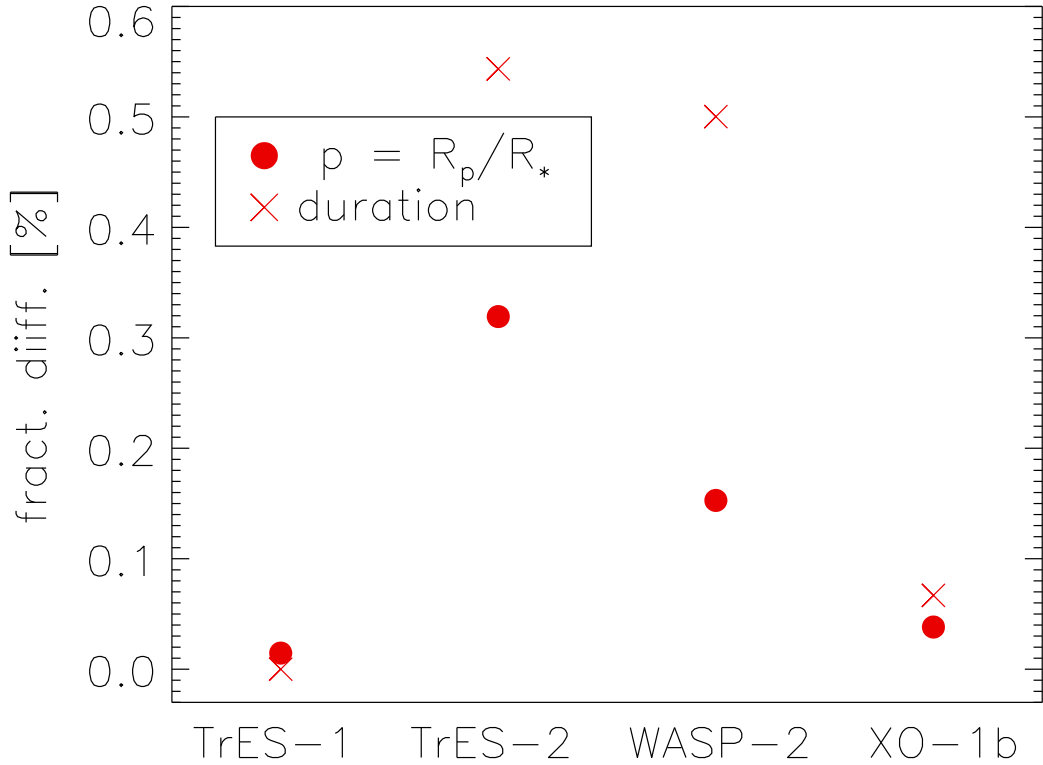


Figure 2.7 Fractional difference of the planet to star size ratio and the transit duration inferred from our modeling and that of the earliest papers related to the data.

The results for the normalized semi major axis differ the most, as it is clearly seen on Figure 2.6. In fact, the maximum deviation is not more than 2.8%, which is still in a good agreement with the results in the publications. The results for the planet to star size ratio and the transit duration are in a better agreement with fractional differences not exceeding 0.55%.

To compute the uncertainties of the fitted parameters, we implemented the Bootstrap Monte-Carlo method (Press et al. 1992). In this approach, the data measurements were re-sampled with repetitions and 'new' sets of data were generated. Every data set was modeled with our grid search code and the corresponding set of fitted parameters were accumulated in distributions. To obtain the later we iterated the process  $10^3$ - $10^4$  times. Finally, the

resulted parameter distributions were statistically examined. For each parameter the standard deviation of every corresponding parameter distribution was calculated. After an analysis of the results of our tests on the Bootstrap Monte-Carlo implementation, we concluded that it systematically underestimated the computed uncertainties, which is expected for the Bootstrap Monte-Carlo method.

### 2.2.3 Exoplanet diagnostic $\eta$

The ratio of the transit duration time  $t_{transit}(obs)$ , measured from the observed transit light curve, to the theoretical duration  $t_{transit}(th)$ , computed for the same system is known as  $\eta$ -diagnostic (Tingley & Sackett 2005). Its value can be computed for each transit candidate using the equation

$$\eta \equiv \frac{t_{transit}(obs)}{t_{transit}(th)} = \frac{t_{transit}(obs)}{2Z(1 + \sqrt{1.3/\delta F})} \left( \frac{2\pi G M_{\odot}}{P} \right)^{1/3} R_p^{-7/12} R_{\odot}^{-5/12} \left( \frac{1.3}{\delta F} \right)^{5/24}, \quad (2.7)$$

where  $\delta F$  is the transit depth,  $P$  is the orbital period,  $R_p$  is the planet radius and  $G$  is the gravitational constant. The factor  $Z$  has a simple geometric interpretation. Its value is equal to unity for transits at inclination of  $90^\circ$  and drops to zero for no transits.

As planetary transits are expected to have much shorter durations than those due to stellar eclipses, all transit candidates with values of  $\eta$  less than unity should be considered as produced by real planets. We used equation 2.7 and implemented it in a tool that computes the  $\eta$ -diagnostic for the transit candidates in the Pan-Planets survey.

In order to test our implementation and to illustrate the efficiency of the method, we computed the  $\eta$ -diagnostic for three different sets of data - the OGLE list of candidates, a set of known transiting planets, obtained from the Extrasolar Planet Encyclopedia (<http://exoplanet.eu/>) and a set of simulated Pan-Planets transits (Koppenhoefer et al. 2009). Our results are presented on Figures 2.8, 2.9 and 2.10.

The ability of the the  $\eta$ -diagnostic and our implementation to separate real transiting planets from impostors is clearly seen on Figure 2.8. In fact, all of the confirmed transiting planets in the set fall below the cutoff line (unity), as well as the two theoretical central

---

transits of Jupiter and Saturn, from our own Solar System. The cutting line should not be interpreted as a strict border. Several false positives fall below it. A possible explanation could be related with the physical assumptions made for the derivation of equation 2.7. The theoretical transit duration there is computed for a Jupiter-sized ( $1 R_{Jup}$ ) planet, transiting a solar-like ( $1 R_{\odot}$ ) star. Furthermore, to eliminate the mass of the star in their equation, Tingley & Sackett (2005) assumed a stellar mass-radius relation.

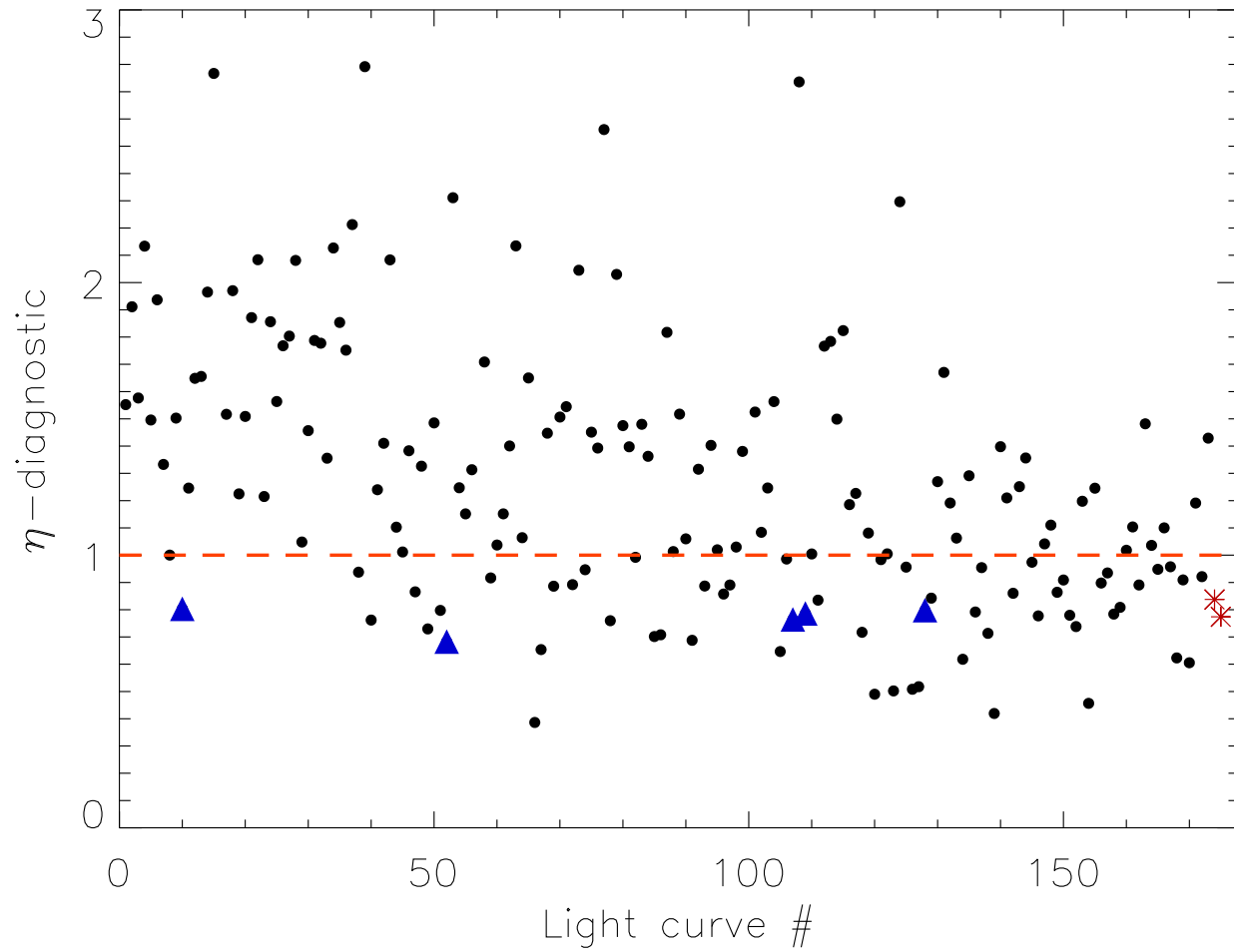


Figure 2.8  $\eta$ -parameter computed for the 173 released OGLE transit light curves (black dots). The red hatched line represents the cutoff below which any extrasolar planets should fall. The blue triangles are the known exoplanets in the sample. The two red stars are theoretical central Jupiter and Saturn transits in our solar system. The trend towards smaller values for the  $\eta$  diagnostic with increasing light curve number reflects the increasing ability of the OGLE team in selecting real transiting planets



At the time of writing (June 2009), there were 59 confirmed transiting planets. Not all of them were considered in our analysis, since only 38 had uniquely determined transit parameters and were included. As it is seen from Figure 2.9 almost 32% of all transits fall above the cutoff line, those objects have rather closer to unity  $\eta$ -diagnostic, i.e. can be distinguished from the false positives, shows that a strict separation should be considered with caution.

As an additional test we computed the  $\eta$ -diagnostic for a set of 110 simulated Pan-Planets transits generated by Koppenhöfer et al. (2009). Those light curves represent an expected outcome of the project during the first year. We found that the result (Fig.2.10) is very similar to the one for known transits. Almost 46% of all transits are above the cutoff line, but still the greatest deviation is smaller than 1.3. The later result will be taken into account when the tool is applied in the real sets of Pan-Planets data and all candidates lying below it will be considered.

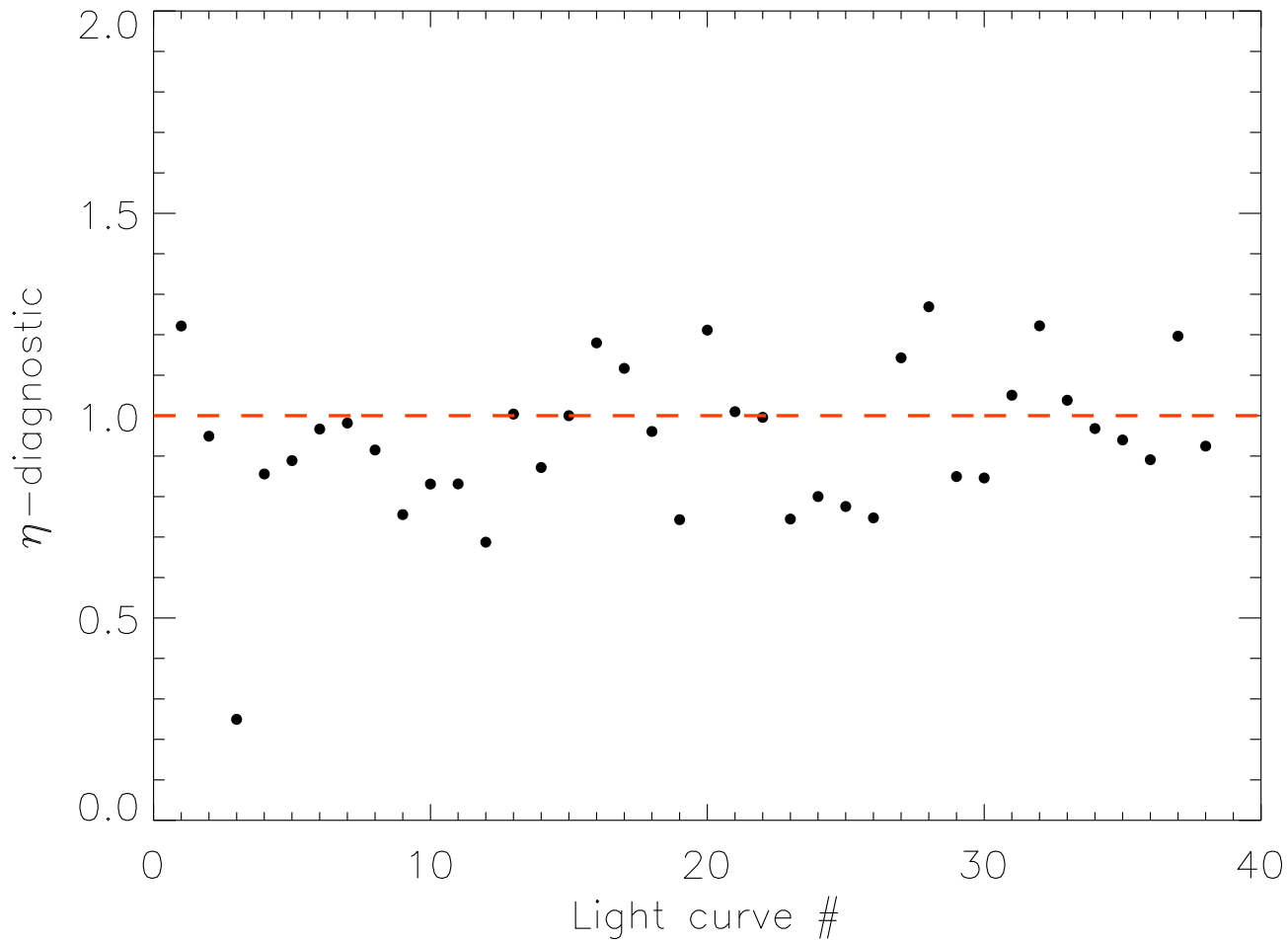


Figure 2.9  $\eta$ -parameter computed for all confirmed transiting extrasolar planets (as of June 2009) with unambiguously determined transit observables (black dots). The red hatched line represents the cutoff below which any extrasolar planets should fall.

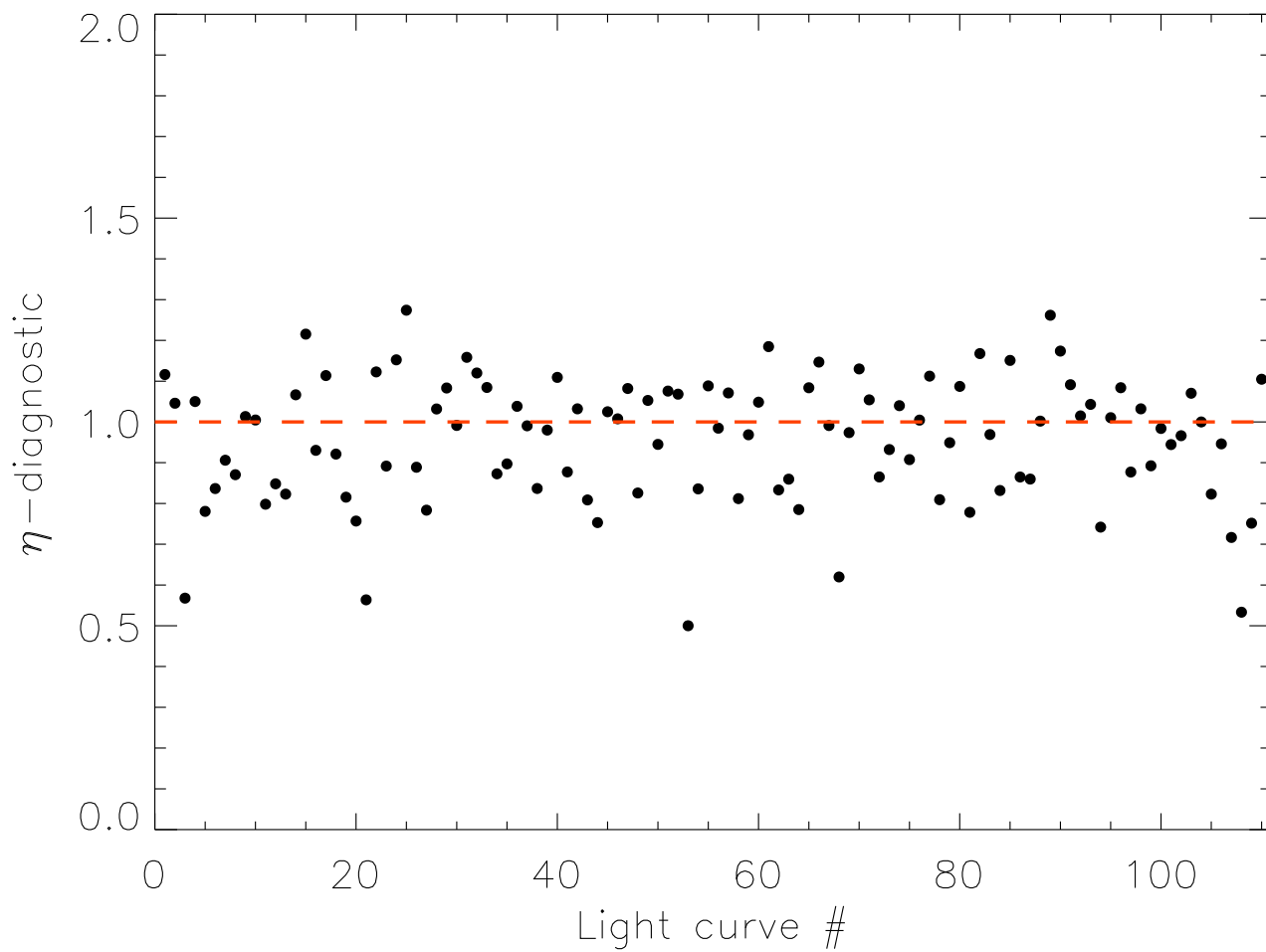


Figure 2.10  $\eta$ -parameter computed for simulated Pan-Planets transits (black dots). The red hatched line represents the cutoff below which any extrasolar planets should fall.



## Chapter 3

---

# Detection of Exoplanets With LAIWO

### 3.1 The GITPO program

The Giant Transiting Planets Observations (GITPO) program is an international collaboration between the Max-Planck Institut für Astronomie - Heidelberg (MPIA), the University of Tel Aviv and the Sternwarte of Göttingen, aiming to discover new Jupiter-size transiting extra-solar planets around main sequence (MS) stars with photometry precision better than 1.5% down to  $V=17$  mag. The observations of the targeted fields are conducted by a ground-based network of two telescopes: 1) the 1m Ritchey-Chrétien (RC) reflector, located at the Wise Observatory in the Negev desert, Israel ( $\lambda = 30^{\circ}35'45''$  N,  $\varphi = 34^{\circ}45'48''$  E) and 2) the 1.2m RC MONET telescope in Texas, USA ( $\lambda = 30^{\circ}40'17''$  N,  $\varphi = 104^{\circ}01'21''$  W) operated by the University of Göttingen, Germany.

This PhD thesis contains scientific results based on a single field observations with the one-meter telescope located at the Wise Observatory.

### 3.2 Observations

#### 3.2.1 The LAIWO instrument

To perform our photometric study we acquired data using the one-meter Wise telescope equipped with the Large Area Imager (LAIWO), built at the Max Planck Institute for

Astronomy (MPIA), Heidelberg, Germany. LAIWO is a wide field optical camera consisted of an array of four front-side illuminated  $4K \times 4K$  CCDs (Lockheed CCD486) with pixel size of  $15 \mu\text{m}$ . The array is arranged in a non-contiguous  $4 \times 4$  mosaic of sixteen quadrants. The gain of each chip is adjusted to be about 5 electrons/ADU<sup>1</sup> with readout noise from about 9 to 19 electrons depending on the chip. The field of view of each chip is a square of  $29.5 \times 29.5$  minutes of arc and the distance between the CCDs is about 26 arcmin. The chips saturate at 65,500 ADU and are connected to four output channels to reduce the read-out time of the entire camera ( $\sim 28$  sec). A telescope guider CCD with field of view  $6.4 \times 6.4$  arcmin is located at the center of the space between the four science CCDs. Figure 3.1 presents a scheme with the LAIWO camera layout.

The telescope (Boller and Chivens) is mounted on a rigid, off-axis equatorial mount and the optics (when adjusted to f/7) delivers one square degree field of view. This translates to about 0.87 arcsec/pixel, when the camera is binned by  $2 \times 2$  pixels. The resultant image produced by a single LAIWO exposure is a sixteen-extension FITS file with a size of 32.1 MB.

### 3.2.2 Data acquisition

Our observations targeted a field located in Ophiuchus (LAIWO-V), which was not previously surveyed for transiting extrasolar planets. The telescope field of view was centered at R.A. (J2000) =  $17^h 21^m 40^s$  and DECL. (J2000) =  $+00^\circ 08' 26''$ . The observing campaign was carried-out over  $\sim 60$  clear nights interval between February 05 and August 06, 2009 and March 02 and June 24, 2010, obtaining a total of 3939 images. The observations consisted of 180 sec Johnson R-band (OG570/2mm+Calflex/1mm) exposures repeated throughout the night as long as the field was above the horizon, resulting in 20-130 images each night, with a  $\sim 210$  sec time resolution. Figure 3.2 displays the 2009 and 2010 observing distributions of the field LAIWO-V. It can be seen that during several nights the observations were terminated due to overlap with other programs.

The weather conditions of our observations ranged from completely clear to slightly cloudy. We undertook several steps in our data reduction process to eliminate the low quality images, caused by excessive cloud cover, moonlight or other undesired effects that

---

<sup>1</sup>ADU - analog-to-digital unit.

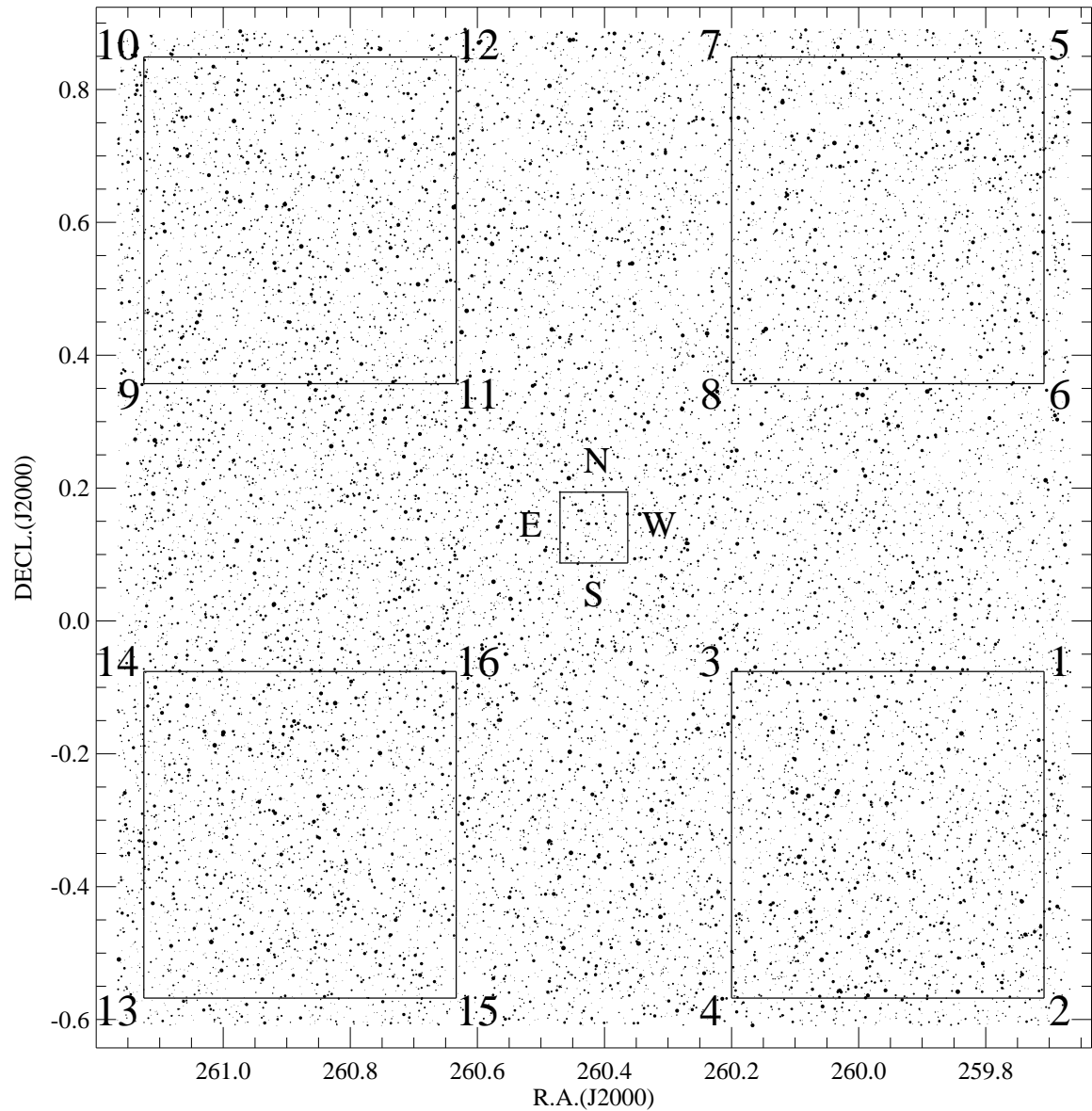


Figure 3.1 The Ophiuchus star field (LAIWO-V), showing the field of view of LAIWO (the four big squares  $29.5' \times 29.5'$ ). The sixteen individual quadrants are numbered as they appear on the sky. The celestial orientation is indicated with capital letters around the guiding detector at the center of the plot.

lower the photometric accuracy.

The autoguiding of the WISE telescope was very accurate during each night, providing a rather steady positions of the stars on the CCD chips. The typical drifts of the stellar

point spread function (PSF) centers was about 2-3 pixels. Unfortunately, the pointing of the telescope was far from ideal. The equatorial coordinates of the center of the observed field were shifted between images of different nights. Typically the shift was  $\sim 20''$  while on 2-3 nights it reached  $\sim 2'$ . The typical telescope pointing shift is small in comparison with the size of the observed field ( $\sim 5\%$ ), however it introduces some unwanted effects on our data. First, it causes the stars at the edges of the field to enter and exit the camera's field of view at the different observational nights, resulting in incomplete light curves for those stars. Secondly, as the  $(x, y)$  positions for a given star vary dramatically over the entire observational campaign, it introduces undesired systematics in the instrumental magnitudes.

### 3.3 Data reduction

#### 3.3.1 Image calibration

All of the 3939 images for our study were processed by a self-developed fully automated data-reduction pipeline. It was implemented in IDL<sup>2</sup> incorporating standard built-in functions and several astronomy utilities<sup>3</sup>, IRAF<sup>4</sup> procedures, SExtractor<sup>5</sup>, SCAMP<sup>6</sup>, and custom-written functions. Figure 3.3 presents a block diagram for each step we undertook in the data reduction and analysis of the LAIWO-V field. Each observational night was processed separately to permit flexibility in the inclusion of new data or a re-analysis of any previously processed data set, if needed.

The pipeline first performed identification, sorting and organizing of the images by type and generated catalogs with extracted header information (such as image identifier, image size, exposure time, filter, time stamp note, etc.). To build the light curves we treated images taken in the R-band only, as they were the most numerous. However, several multi-band exposures were obtained for the further characterization of the observed

---

<sup>2</sup>IDL - Interactive Data Language

<sup>3</sup>mainly from the IDL Astronomy Library (see, <http://idlastro.gsfc.nasa.gov/homepage.html>)

<sup>4</sup>IRAF - Image Reduction and Analysis Facility distributed by the US National Optical Astronomy Observatory

<sup>5</sup>SExtractor - Software for source extraction, Bertin (1996)

<sup>6</sup>SCAMP - software for astrometric solution, Bertin (2006)



field (acquired in the Johnson B, V and the Sloan I' pass bands). While performing this step of the data organization it became clear that nearly each night the header keywords OBJECTNAME and OBTYPE for the BIAS, DARK and the FLAT fields were uniquely selected by the observer. This resulted in difficulty and additional time spent in the identification of the calibration frames. In addition, we identified one night in which the field identifier was different in comparison with those of the remaining images. The equatorial coordinates header keywords (RA and DEC) contained values significantly different from the real field positions and were therefore, not used in the field identification process. Finally, the image scale was nearly correct in the DEC however, inconsistent in the R.A. direction.

The sixteen-extension mosaic images were processed independently to account for the differences between them, so there were a total of 63,024 raw images to reduce. First, each of them was bias and dark subtracted. The master/combined bias and dark frames were calculated from the median of the available number of zero-second exposures and 180-second exposures respectively (typically  $\sim 5$ ), after applying a quality selection criterion. Bias and dark calibration frames showing variation  $\geq 10\%$  of their median and averaged ADU values were not considered in the master frame calculation. Next, the science images were divided by a master flatfield, computed from the reduced and median combined twilight sky flats. We considered only flat frames with values in the range 10,000 to 45,000 ADUs taken over the same observational date. There were no calibration frames for a 3-4 nights, as well as a few flat frames with presence of stars. In such cases we used calibration frames from the closest observational date.

Finally, the calibrated science images were carefully checked to ensure the successful execution of all tasks at this stage of the data reduction process.

### 3.3.2 Stellar source detection and image quality constraints

Identification of the stars on each science image was performed using SExtractor 2.8.6 (Bertin & Arnouts 1996). It produced catalogs containing measurements of the  $(x, y)$  pixel coordinates on the image, full width at half maximum (FWHM), source flux and uncertainty and sky level for each detected stellar source in the range  $(0 - 65,000)$  ADU. We excluded all detections at distances  $\leq 10$  pixels from the image borders, as well as

all non-isolated detections as they might produce erroneous photometric measurements (due to blends) in the subsequent light curves. We found that SExtractor executes very efficiently ( $\sim 2$ -3 sec per image) and identifies sources successfully even in the few closely located stars in our field.

Quality criteria cuts were established for each reduced image, based on the distributions of the median seeing (FWHM), sky background and the number of star sources measured by SExtractor in the corresponding quadrant. We collected those measurements for each image and computed the seeing, number of stars and background distributions after the data reduction phase (Figures 3.4, 3.5 and 3.6). Image quality constraints were considered and performed as necessary to indicate the low quality data. On one hand, the images showing abnormally high median seeing are a clear indication for low quality observational conditions. On the other hand, the high sky background levels in combination with extremely low number of stellar sources originated probably due to clouds or moonlight.

Images satisfying the following criteria were excluded from the further analysis for each quadrant:

1. Seeing  $\geq 3.5''$ ;
2. Number of stars  $\leq 350$ ;
3. Background level  $\geq 12,000$  ADU or  $\geq 4.1$  in logarithmic scale;

In all, on average about 1240 low quality images for each quadrant ( $\sim 34\%$ ) were eliminated from the initial data set (Figure 3.7). The remaining  $\sim 2700$  (on average) images per quadrant were processed by our pipeline. We describe that procedure below.

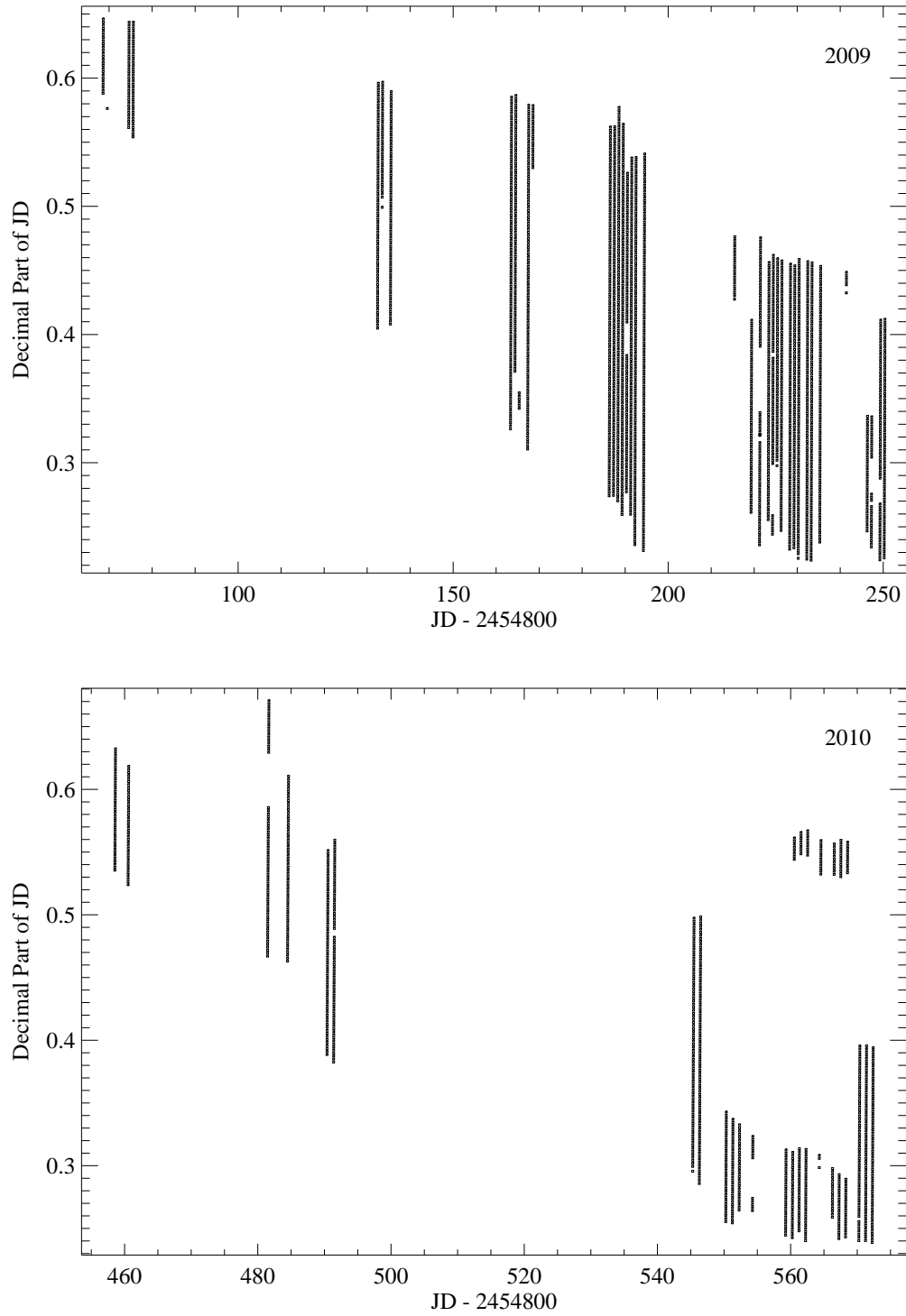


Figure 3.2 Observation distributions of the LAIWO-V field during 2009 (top panel) and 2010 (bottom panel). Each vertical sequence represents an observing night and each point corresponds to an image. The observations during several nights have been interrupted due to time critical observations and other projects.

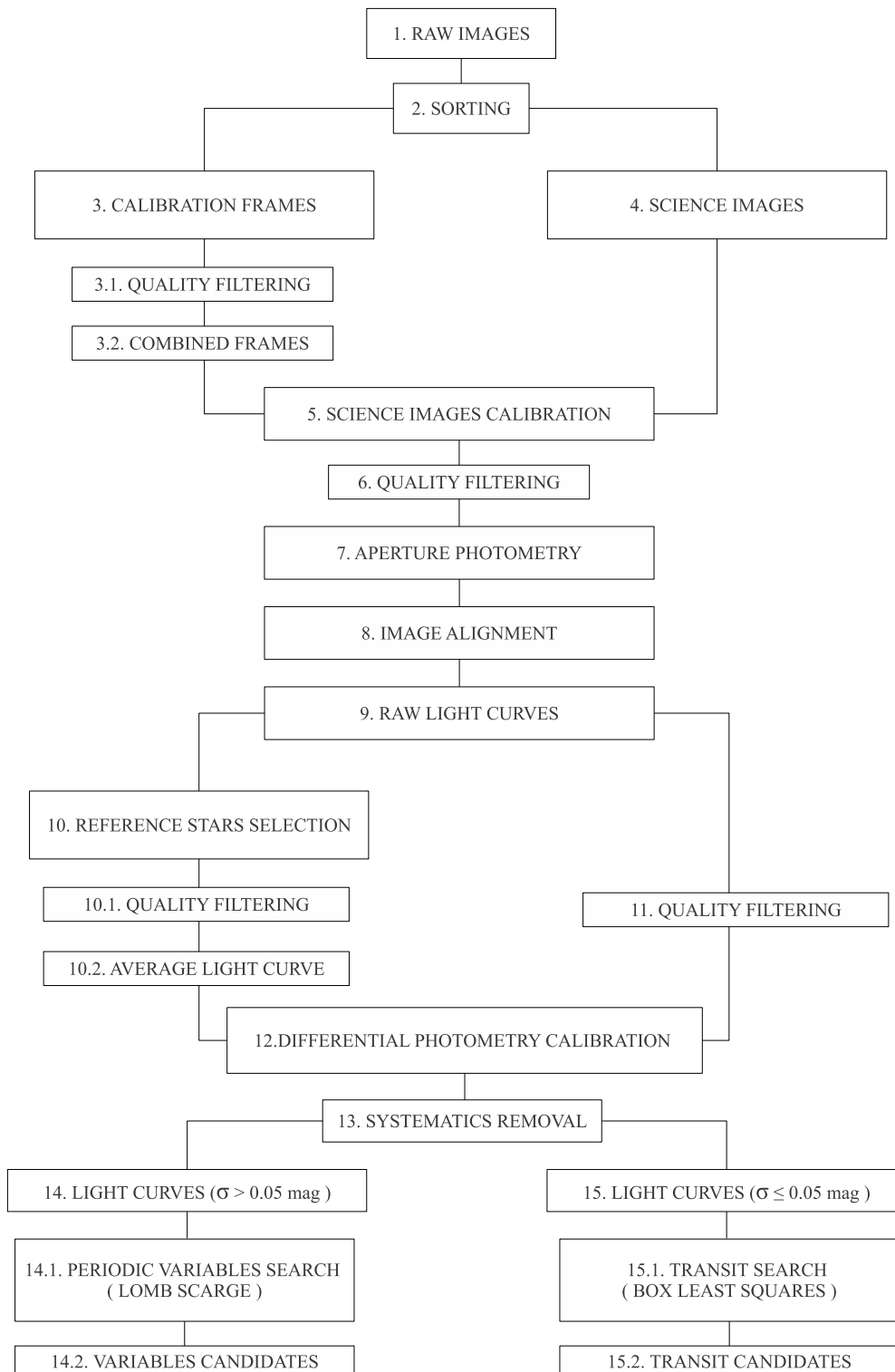


Figure 3.3 Flow chart describing the individual levels of data treatment in our processing pipeline.

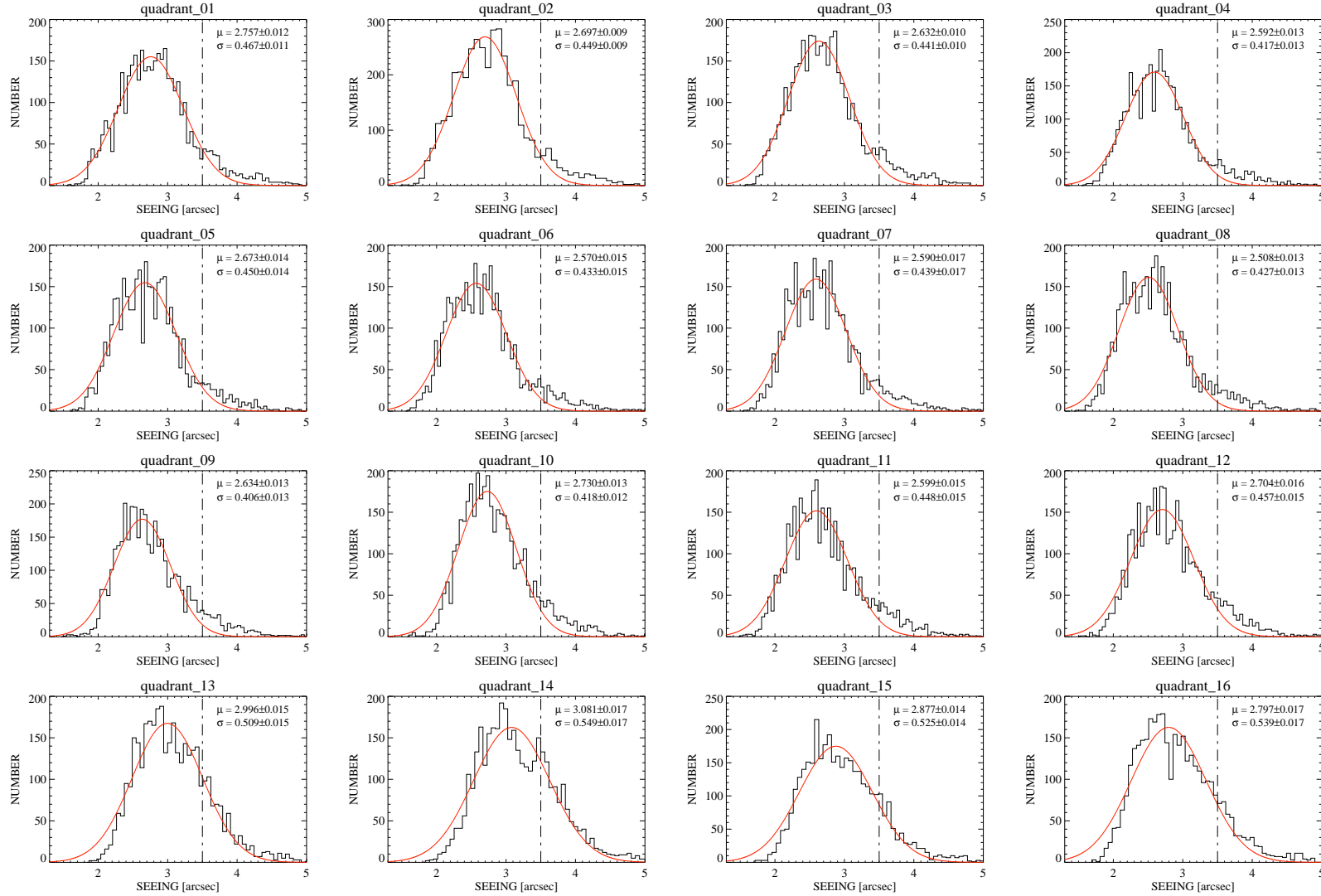


Figure 3.4 Seeing distributions for each quadrant of the LAIWO-V field, based on the entire data set before any cuts. We assumed a Gaussian model as a rough approximation of our seeing distributions. The best fit Gaussian curve is overplotted and its mean ( $\mu$ ) and standard deviation ( $\sigma$ ) is indicated along with the corresponding uncertainties. Each seeing image quality cut is represented with a vertical dash-dotted line.

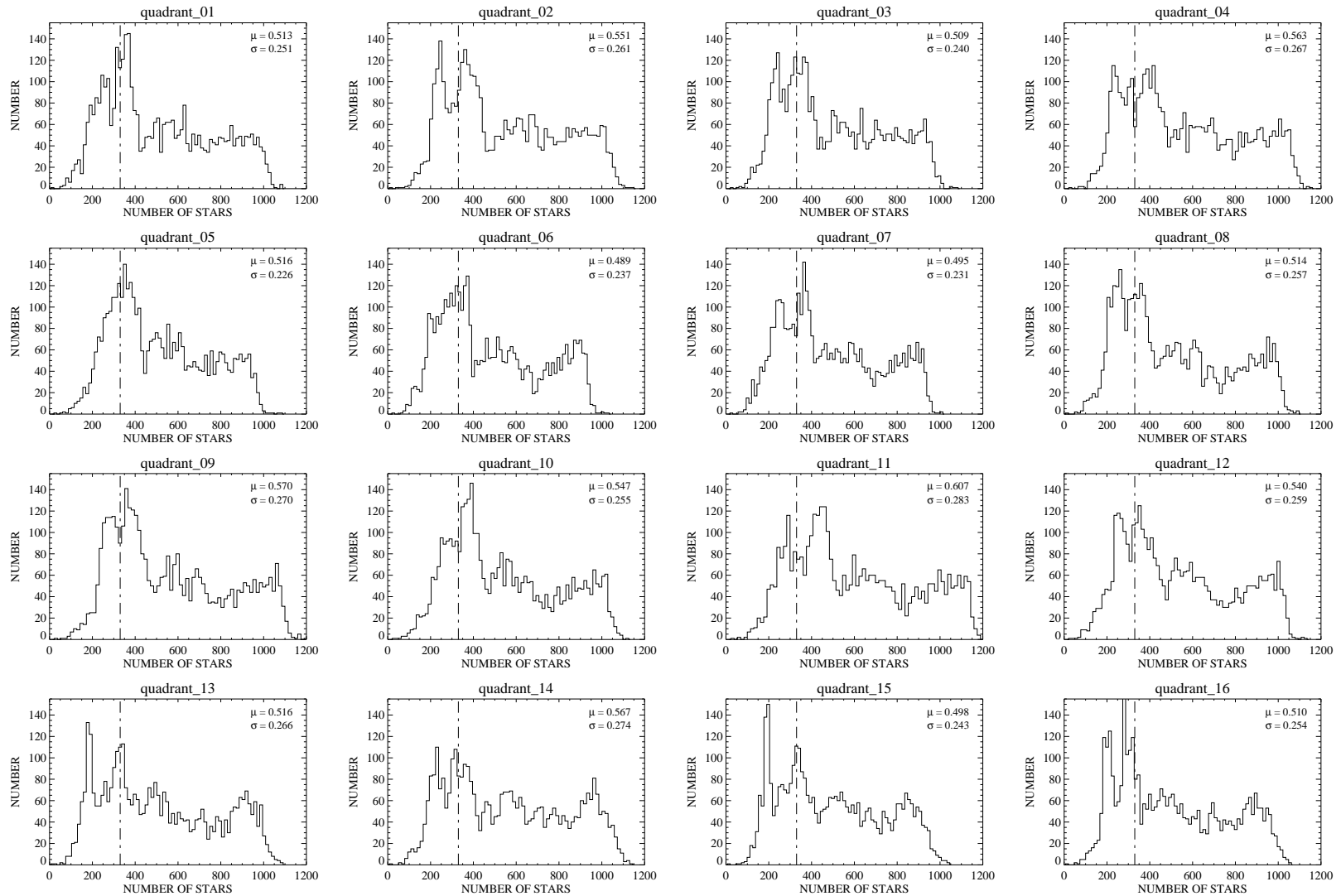


Figure 3.5 Histogram of the median number of stars per image for the LAIWO-V field. The mean ( $\mu$ ) and the standard deviation ( $\sigma$ ) were computed using the entire data set. Image quality cuts are indicated with the dash-dotted vertical lines for each quadrant.

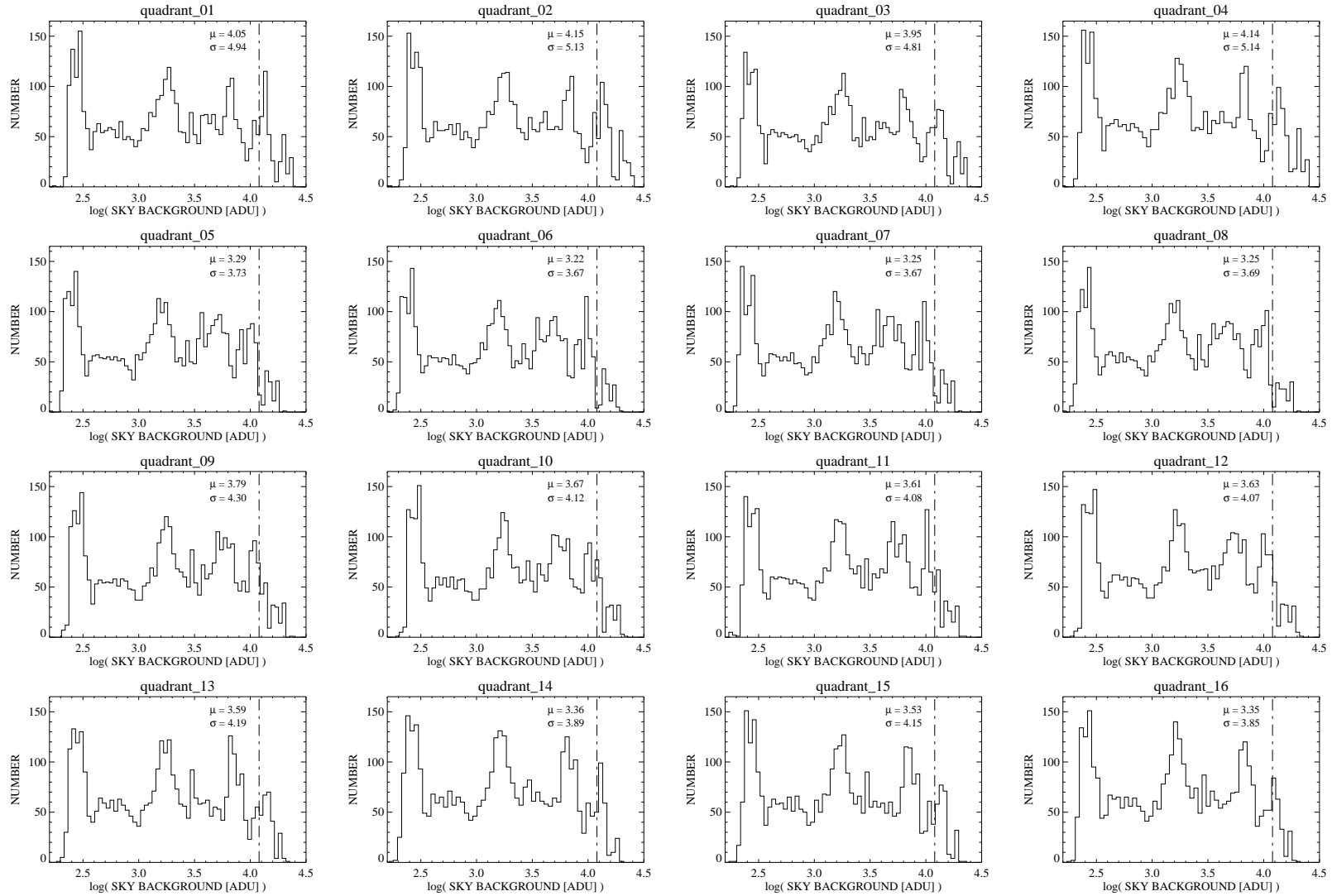


Figure 3.6 Same as Figure 3.5 however, for the median sky background in logarithmic scale. Images with exceptionally high median background level ( $\geq 12,000$  ADU or 4.1 in logarithmic scale) were excluded from the further data analysis.

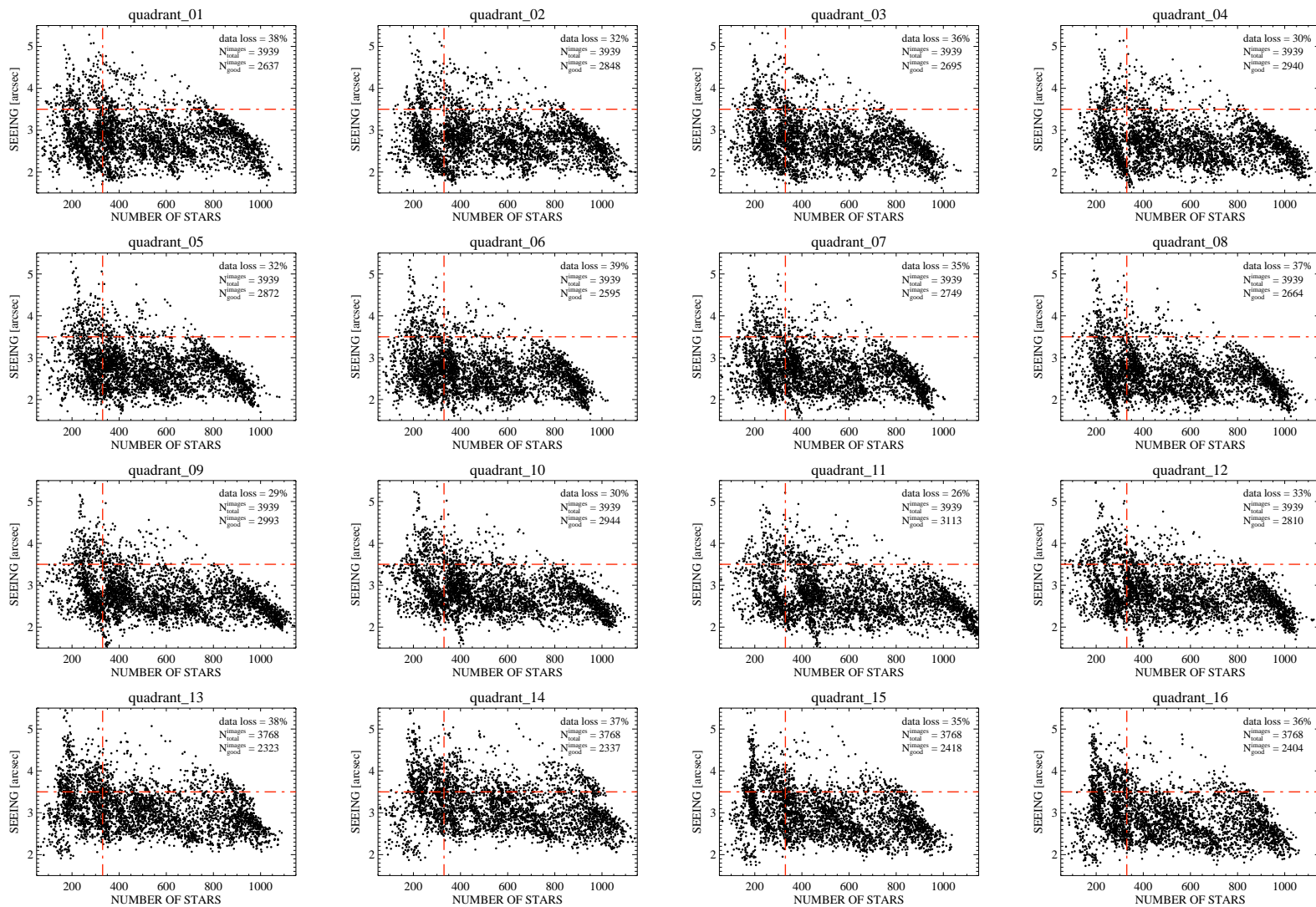


Figure 3.7 Correlation between the number of stars and the seeing for the total data set of the LAIWO-V field. Two of the data quality cuts are indicated with horizontal (seeing  $3.5''$ ) and vertical (number of stars at 350) dash-dotted lines. Percentage data loss, initial number of images and remaining good quality images are indicated after the cuts including a background cut.



## 3.4 Photometry

### 3.4.1 Source measurement

The variability study, presented in this thesis, was based on differential photometry relative to a set of non-variable reference stars. To measure the instrumental magnitudes we employed aperture photometry using the DAOPHOT-type photometry procedures from the IDL Astronomy Library. The initial PSF central pixel positions  $(x, y)$  of the detected stars were recentered by a Gaussian fitting to parts of a pixel precision (computed by GCNTRD). We used the APER routine to perform aperture photometry with a constant radius throughout each image. We experimented with various aperture sizes in images with different sky backgrounds, aiming to maximize the signal-to-noise ratio ( $SNR$ ), which is given by

$$SNR = \frac{1.0857}{\delta m}, \quad (3.1)$$

where  $\delta m$  is the error in the instrumental magnitude and the equation is valid as long as  $\delta m \ll 1$ . Finally, the stellar instrumental magnitudes were measured with apertures in the range (3.0 to 4.0) pixels. We considered only stars with pixel values (within the aperture size) in the linear regime of the CCD detector (0 to 35,000 ADUs).

The background level for each frame was measured using the APER function. The sky subtraction was performed by measuring the median background level around each star by a large aperture. To avoid contamination of neighbor stars we selected the big aperture to have area typically four times bigger than the one used to measure the star flux.

To be able to trace low photometric quality atmospheric conditions (such as clouds, moonlight, etc.) we employed the following methodology. The flux of several bright stars was measured using a relatively large aperture (typically  $\geq 10$  pixels) to guarantee a consideration of the total starlight. We denoted such stars as 'Flux Monitoring Stars' (FMS) and we used them later in the relative photometry analysis (see Section 3.4.3).

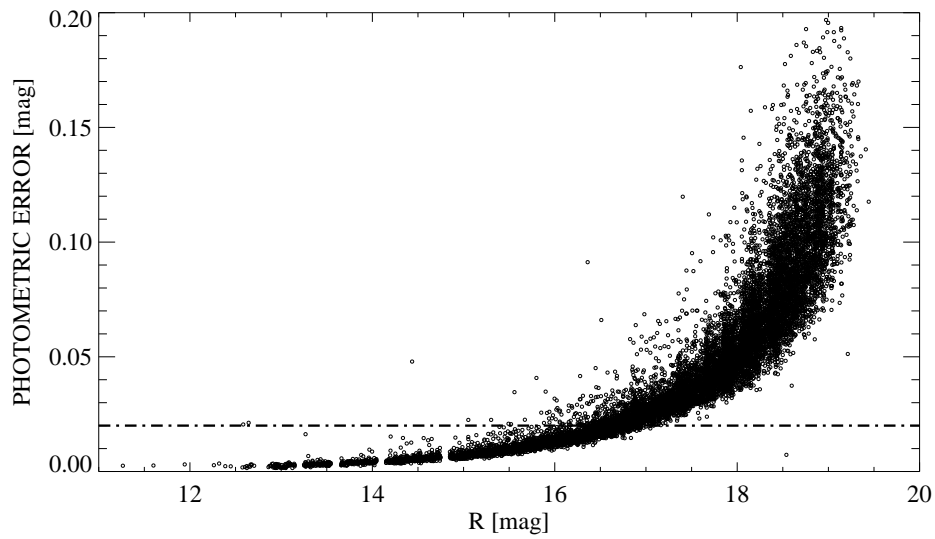


Figure 3.8 Photometric uncertainty as a function of the R magnitude for all quadrants of the LAIWO-V field, computed from the 20100613lc0050 image. The dashed dotted line marks the 2% level with 3069 stars below it, or  $\sim 20\%$  of all stars in the field.

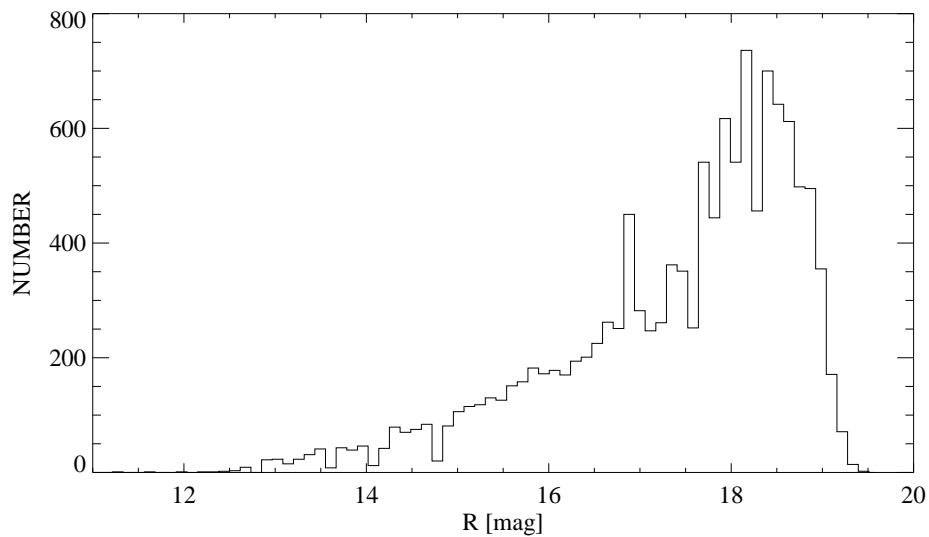


Figure 3.9 Stellar R magnitude distribution of all sources detected in the LAIWO-V field. 2820 of all stars were measured with a R magnitude below 16.5.

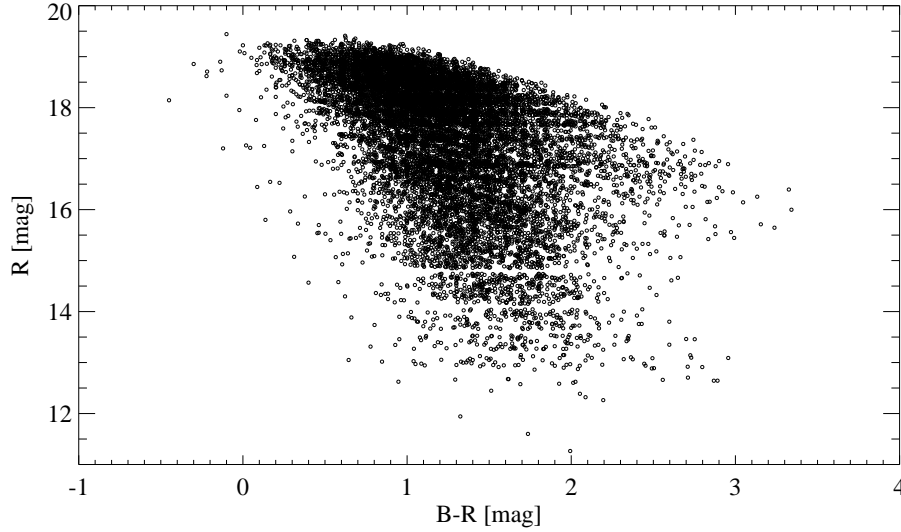


Figure 3.10 Color magnitude diagram (CMD) for the stars in the LAIWO-V field, after matching with the USNO-B1 catalog.

### 3.4.2 Astrometry and matching to stellar catalogs

To be successful, the process of light curves production requires a proper identification of one and the same light source on each image of a time series. One solution for such a problem is to compute the coordinates of each source on each image with respect to a reference point. We used the SExtractor, SCAMP and SWARP programs to derive astrometric solutions for each of our images, using the Two Micron All Sky Survey (2MASS) catalog (Skrutskie 2006). Figure 3.11 displays a diagram with each step we undertook to produce the light curves.

First, we selected reference frames for each quadrant based on high number of stars. Then an initial rough astrometric solution was obtained by identification of one star per field with its equatorial coordinates on a DSS<sup>7</sup> image (R-filter). Using the SExtractor, SCAMP and SWARP modules we then found an accurate astrometric solution between the reference image and the 2MASS catalog. We acquired <sup>8</sup> the later centered on the

---

<sup>7</sup>Digitized Sky Survey

<sup>8</sup><http://www.ipac.caltech.edu/2mass/>

LAIWO-V field of view with size  $3^\circ \times 3^\circ$ . Since several images were obtained at a significant displacement from the actual coordinate positions of our field (see Section 3.2.2) we allowed the three modules to search each image to shifts up to 15 arcmin. We found that the three astrometric tools work quite efficiently, providing accurate (typically fractions of seconds of arc) astrometric solutions for a reasonable amount of time (about three seconds per image). Figure 3.12 presents an example of the astrometric solutions for all images in the tenth LAIWO-V quadrant with the selected reference frame.

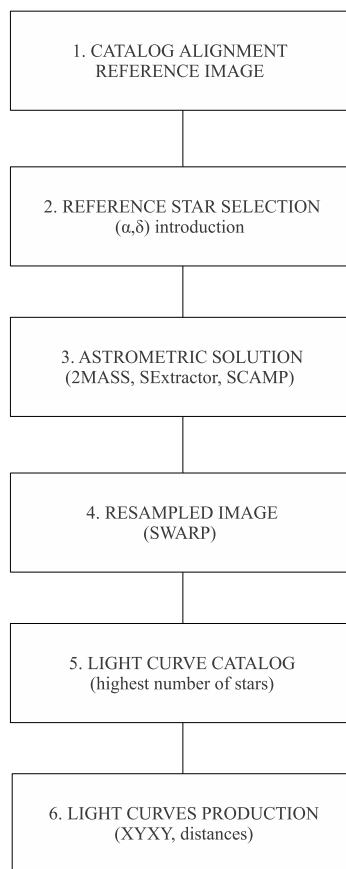


Figure 3.11 Digram presenting the astrometric alignment process.

Traditionally, SWARP produced astrometrically aligned images which were re-sampled, as the program corrects for rotation and image distortions. Typically, the values of the re-sampled image pixels were plagued with about 1-2% variation, as explained in the SWARP's

user guide. To avoid an introduction of such unwanted variability in the aligned images we undertook the following strategy. The aligned images were used only to provide header astrometric information, while the photometric measurements of the same sources were used from the images before alignment.

To generate the light curves for each quadrant we selected new reference images satisfying the following criteria: (1) high number of stellar sources (typically about 1000 stars); and (2) positions on the sky close to those at which the bulk of the images were taken (see Figure 3.12). The stars found in the newly selected reference images were used to create each light curve identification number (ID). It consisted of the prefix 'laiwo\_lc\_' plus the number of the star in the reference image.

We further computed the matched  $(x, y)$  positions of each reference star with those on each of the remaining images using the XY2XY function, provided by the IDL Astronomy Library. A source matching was performed by calculating the distances between a given reference source and all available stellar detections present on each image. To save computational time we further constrained our code to search in a radius of 50 pixels around each reference star, and finally produced the light curves. It was found that the described procedure worked for most of the sources with a sub-pixel accuracy.

Once we had accurate astrometric information for each header we computed the equatorial coordinates (R.A. and DEC.) for each of the present stars with the XY2RADEC function. A knowledge of the stellar equatorial coordinates permits one to perform source match with known stellar catalogs. We investigated all astronomical catalogs available on the WEB for overlap with our field. It became clear that besides the JHK bands available from the 2MASS catalog the USNO-B1 catalog provides BVR photometry. Both catalogs are incorporated in the common PPMXL catalog (Roeser et al. 2010). In our source matching approach we attempted to identify the closest reference point object within a radius of 3'' around the coordinates of our targets. We found that  $\geq 85\%$  of the LAIWO-V stellar detections were present on both catalogs. Figure 3.8 shows the error diagram for the field LAIWO-V, from the reference image 20100613lc0050 after, source matching. Nearly 20% of the stars had photometric precision better than 2%, which is the necessary photometric precision to search for transiting planets. Figure 3.9 displays the corresponding to Figure 3.8 R magnitude distribution. It can be concluded that most of the stars are faint, i.e. with magnitudes fainter than 16.5–17.0. Figure 3.10 presents a color magnitude ( $B - R$  vs.  $R$ ) diagram for the bulk stellar sources (matched) in the LAIWO-V field.

Besides the UBV and JHK magnitudes, the PPMXL catalog provided stellar proper motion (PM) measurements with uncertainty. We found that many of our sources showed PM different than zero (typically  $\sim 10 \text{ mas}^9$ ), which is indicative for their close distance.

---

<sup>9</sup>milliarcsecond

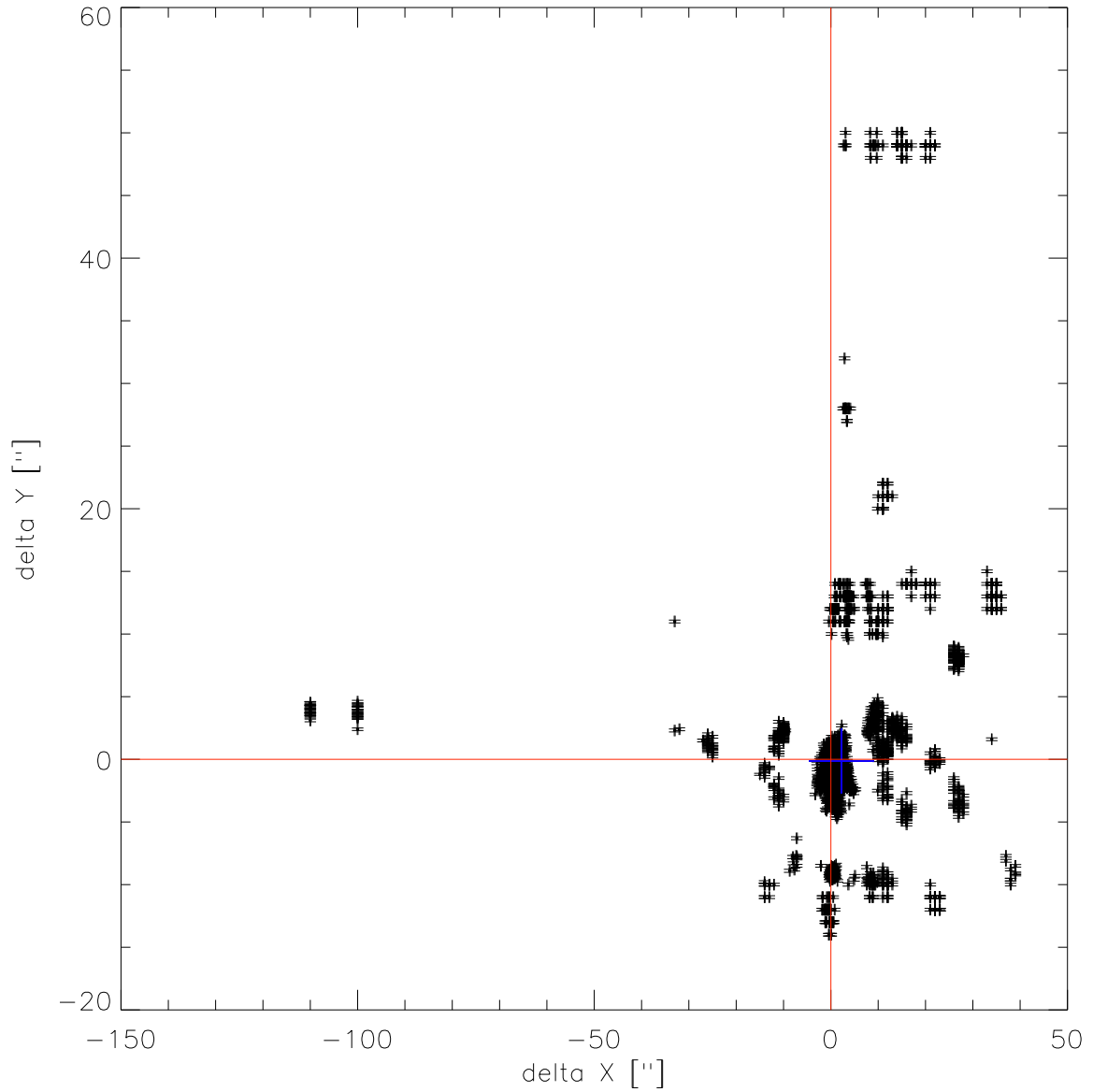


Figure 3.12 Horizontal and vertical shifts (in pixels) of the images (black crosses) from the tenth LAIWO-V quadrant, with respect to the reference frame used for catalog matching (the plot origin is marked with red cross). The blue cross corresponds to the geometric center of the point sequence. The closest to that point image, showing in the same time a high number of stellar sources, served as a reference for the  $(x, y)$  transformation of all remaining images.

### 3.4.3 Differential photometry

In the previous section we described our approach to obtain light curves from a time series. However, without a photometric calibration, such light curves contain a bunch of systematics, caused by airmass variations, clouds, moonlight etc. To be able to search for small variations in the stellar brightness on the 1-2% level, it is essential to calibrate the starlight with respect to a constant flux that appear on each image. We performed differential photometry of all sources, using a reference light curve of an artificial star. It was calculated by averaging the magnitudes of a set of non-variable stars, present on each image of the observed field, following the method of Scholz & Eislöffer (2004). We describe the details in the selection process of the reference stars.

First, a sample of potential reference stars (PRS) was selected for each quadrant from the entire data set. The PRS had to satisfy a list of conditions:

1. Presence on every image of the time series.
2. PSF centers sufficiently isolated from the image borders and other close sources (to avoid light contamination);
3. Photometric errors (given by APER) on average  $\leq 0.025$  mag (2.5%).

Secondly, to identify and reject variable objects present in the initial PRS subset we examined the intrinsic variability of each star with respect to the mean light curve of all other potential reference stars. Taking the original designations of Allain (1995), we indicated with  $i = 1...N_R$ , the number of PRS, with  $j = 1...N_B$  the image number and computed the several statistical quantities.

Average magnitude for each PRS, using the relation

$$\overline{m}_i = \frac{1}{N_B} \sum_{j=1}^{N_B} m_i(t_j) \quad (3.2)$$

Then for each reference star we subtracted the average magnitude (Eq. 3.2) from the corresponding PRS magnitudes on every image:



$$m_i^0(t_j) = m_i(t_j) - \overline{m_i} \quad (3.3)$$

At this point we obtained  $N_R$  light curves each consisted of  $N_B$  differences (originating from each element of the time series) from Eq. 3.3. Next, we computed the mean and the standard deviation of each PRS light curve, following the equations:

$$\overline{m_j^0} = \frac{1}{N_R} \sum_{i=1}^{N_R} m_i^0(t_j) \quad (3.4)$$

$$\sigma_j = \sqrt{\frac{1}{N_R - 1} \sum_{i=1}^{N_R} (m_i^0(t_j) - \overline{m_j^0})^2} \quad (3.5)$$

The photometric quality of the images included in the described calibration can be quantified. Figure 3.13 displays the mean difference as a function of the standard deviation. We studied the scatter of our light curves after calibration with the reference source and found that it increases when images showing high mean and standard deviation values are included. In particular, the FMS brightness correlates with the mean difference (Figure 3.14). As the light of the FMS was measured with a large aperture, much larger than those used for the other sources, its flux is practically insensitive to seeing variations. Thus, the correlation proves that the mean difference is indicative for cloud cover (low extinction).

To exclude the low quality images we applied a compromise  $\sim 2\sigma$  level cut in the mean difference plot of each quadrant. The described procedure (step one and step two) is repeated again without the rejected low quality images. Some moderately bright stars might be missing on those images, while present on most of the good ones.

Third in our reference light selection procedure, for each PRS we computed an average brightness correction (per image  $t_j$ ) determined by averaging the magnitudes of all other reference stars.

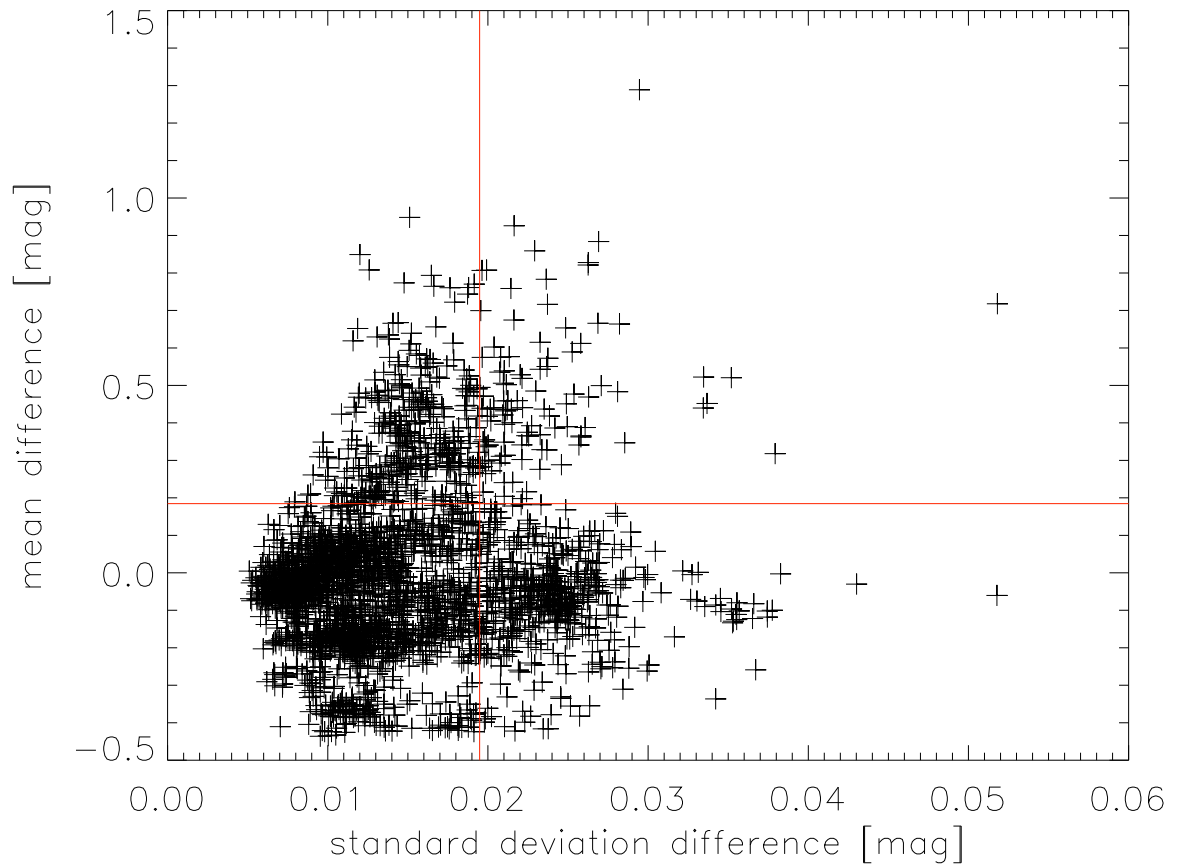


Figure 3.13 Mean difference as a function of the standard deviation, computed for the PRS light curves. Each point on the plot corresponds to an image. The higher values of mean differences and standard deviations are indicative for low quality atmospheric conditions. The two continuous lines indicate the  $2\sigma$  levels beyond which low quality images should fall.

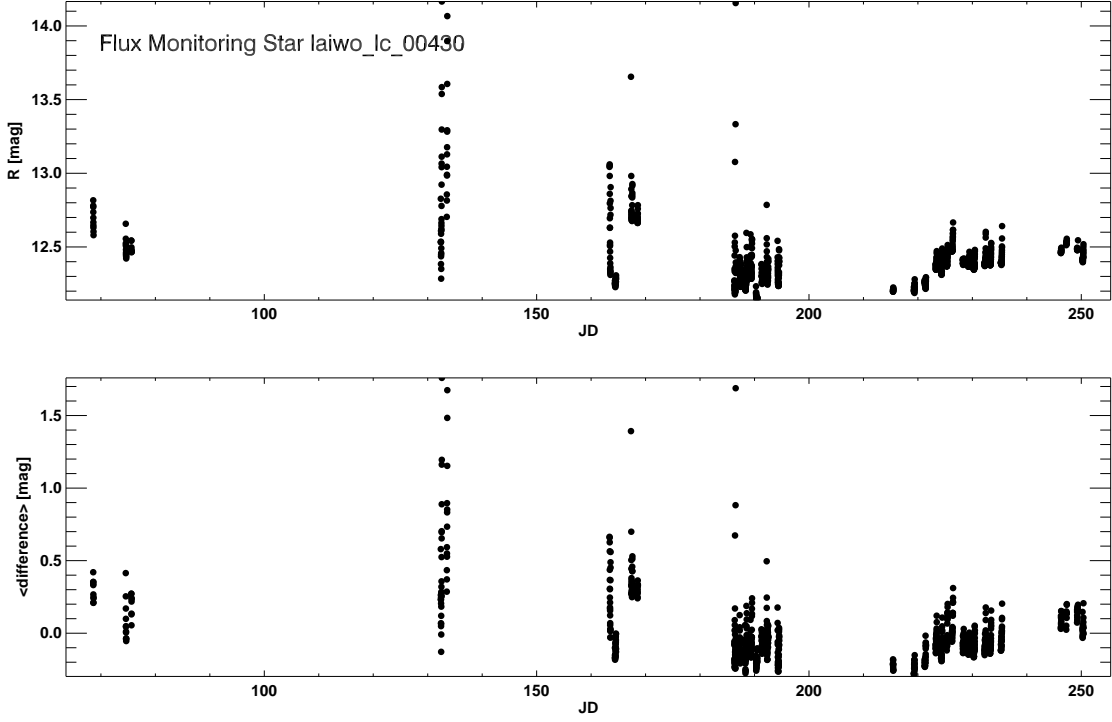


Figure 3.14 Correlation between the magnitude of the flux monitoring star and the mean difference indicative for low quality atmospheric conditions.

$$\overline{m'_j} = \sum_{i \neq k} m_i(t_j) \quad (3.6)$$

The differential light curve of each PRS was computed following

$$m_{k,j}^0 = m_{k,j} - \overline{m'_j} \quad (3.7)$$

The intrinsic variability of each PRS was further evaluated by examining the standard deviation (scatter) of their light curves. We then excluded the light curve with the highest scatter and repeated the third step without the rejected PRS. The described procedure was iterated until the mean scatter of the average reference light curve was greater than 0.7%. Due to the low number of bright stars in the LAIWO-V field we decided to terminate the iterations if the number of stars was less than twenty.

Finally, the reference stars were identified and their magnitudes per image averaged to produce the artificial light curve. Figure 3.15 presents the positions of the 29 identified stars in the seventh quadrant, used to compute the reference light source. The correct computation of the average reference star requires a uniform distribution of the reference stars along the chip.

$$\overline{m}^{ref}(t_j) = \frac{1}{N_{ref}} \sum_{i=1}^{N_{ref}} m_i^{ref}(t_j) \quad (3.8)$$

To correct each stellar source we subtracted the artificial light and produced light curves with significant decrease of systematics.

$$\overline{m}^{rel}(t_j) = m(t_j) - \overline{m}^{ref}(t_j) \quad (3.9)$$

Figures 3.16 and 3.17 display two examples of reference star light curves. Note the significant decrease of the standard deviation in the calibrated light curves. Figure 3.18 shows the magnitude root mean square (r.m.s) or scatter in logarithmic scale, computed for all differential light curves as a function of the R magnitude. Without detrending, 1840 light curves lie below the 2% threshold, necessary for transit detection.

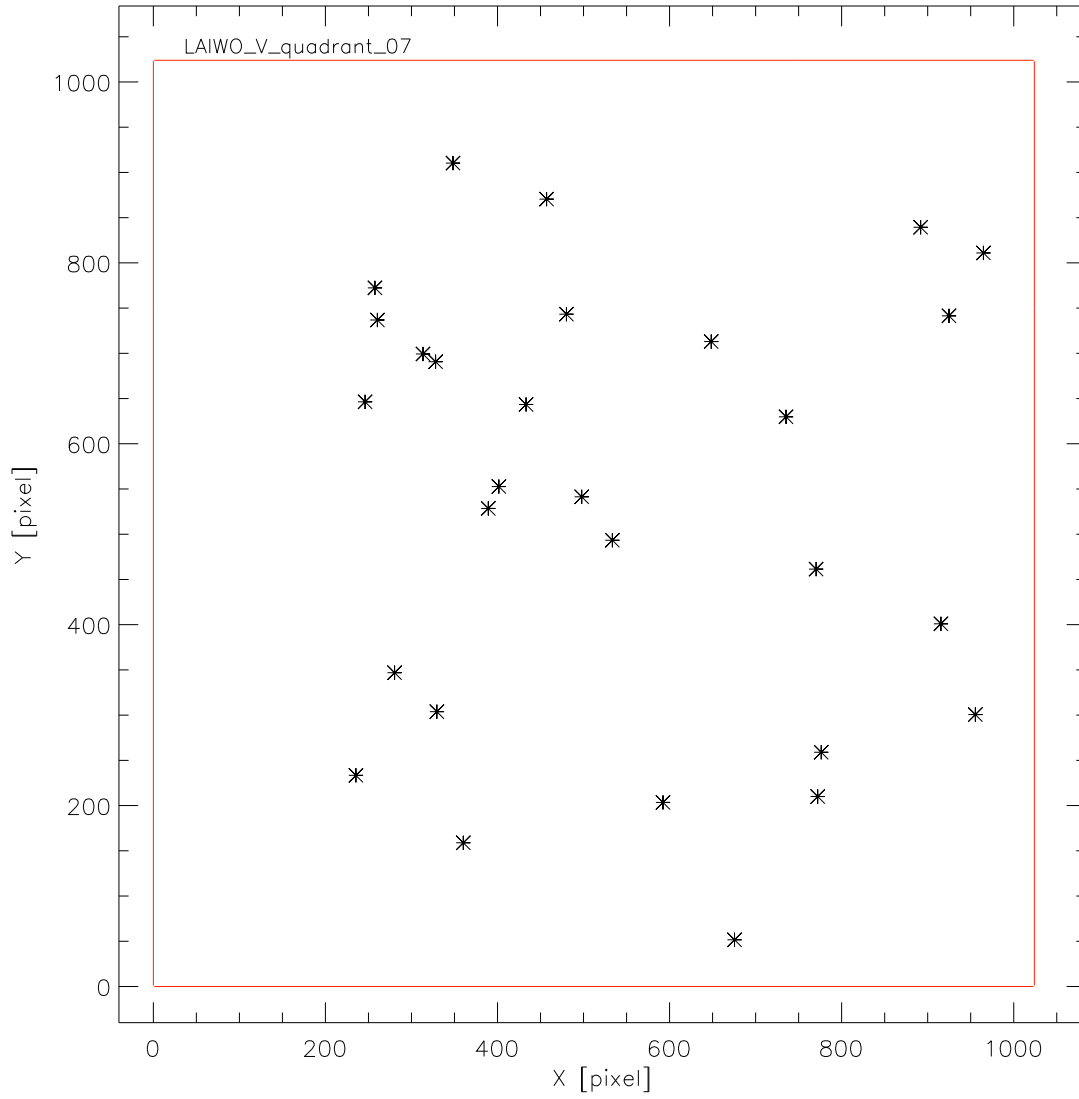


Figure 3.15 Reference stars positions on the seventh LAIWO-V quadrant. The selection of uniformly distributed reference stars along the CCD chip is critical for the proper computation of artificial source for differential photometry.

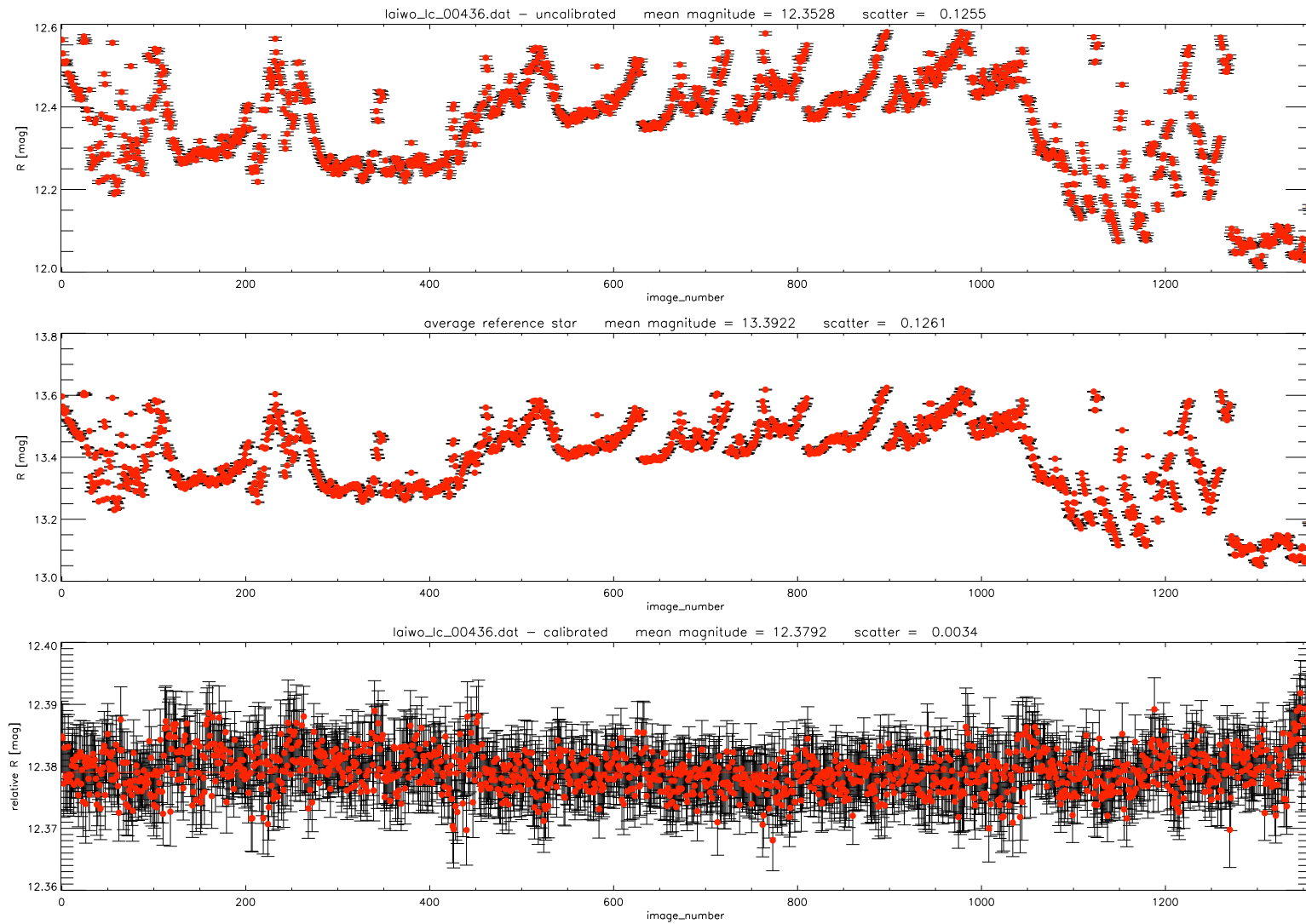


Figure 3.16 The light curve of reference star laiwo\_lc\_00436 identified in the seventh quadrant of the LAIWO-V field. The upper panel displays uncalibrated light curve, the middle panel the artificial light curve and the lower panel the calibrated reference star. The light curve scatter after calibration has dropped to  $\sim 0.3\%$ .

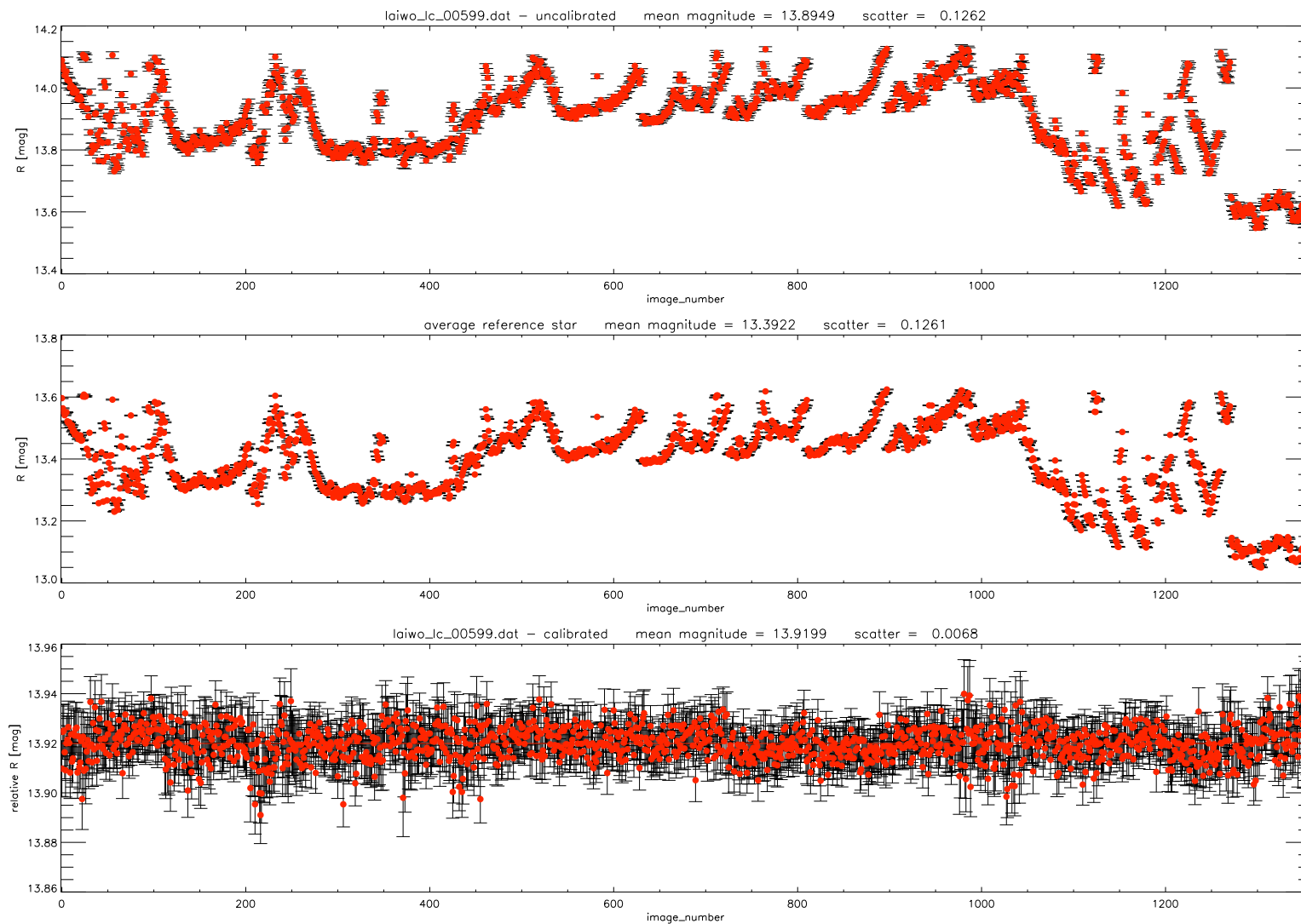


Figure 3.17 The light curve of reference star laiwo\_lc\_00599 identified in the seventh quadrant of the LAIWO-V field. The upper panel displays uncalibrated light curve, the middle panel the artificial light curve and the lower panel the calibrated reference star. The light curve scatter after calibration has dropped to  $\sim 0.3\%$ .

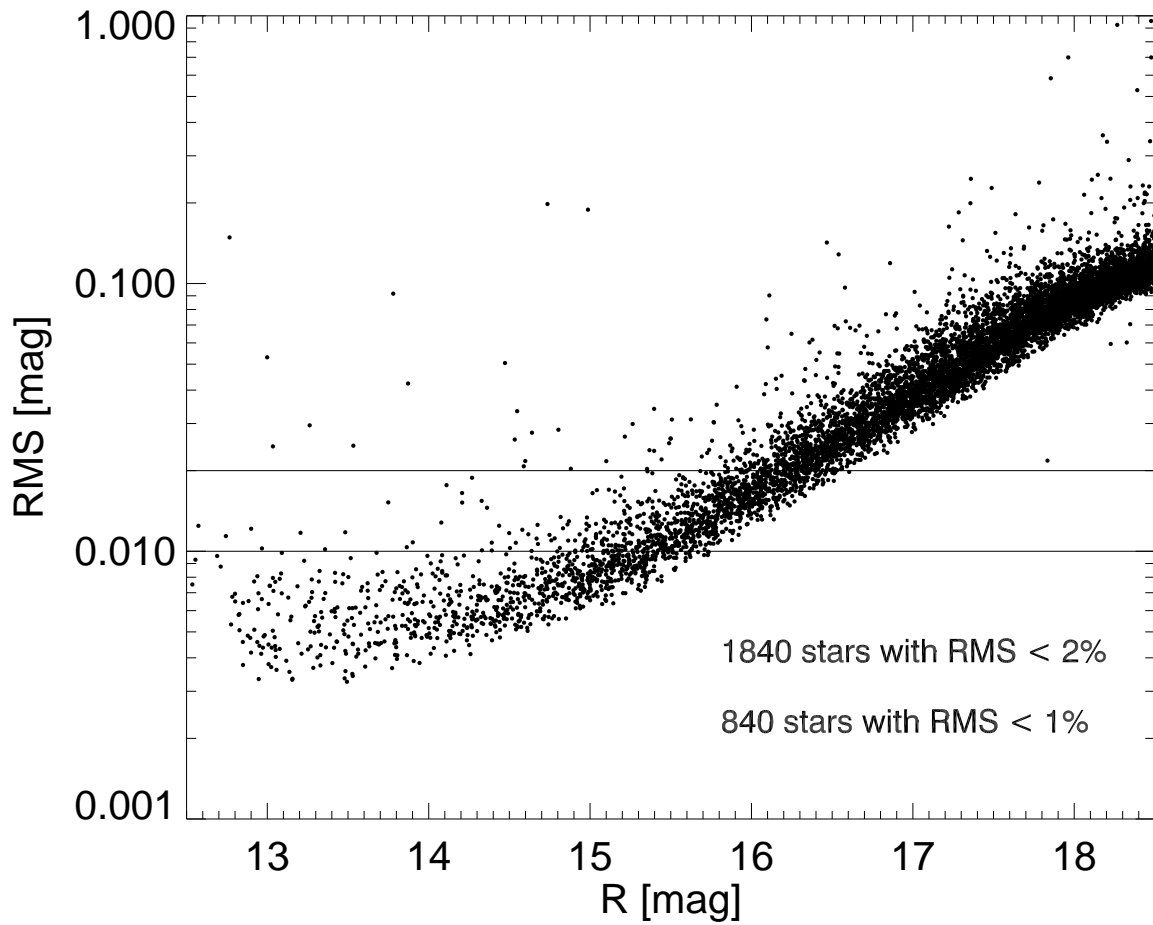


Figure 3.18 Photometric results for the stars in the LAIWO-V field. RMS (root mean square) in logarithmic scale over the observations in 2009 and 2010 is plotted as a function of the R magnitude without detrending.

#### 3.4.4 Data loss

A summary of the data loss after the application of all data quality constraints is presented in Table 3.1.



Table 3.1 Summary of the data survived after each step of the analysis. The last two columns correspond to the final number and percentage of survived images.

Q <sup>a</sup>	TOTAL <sup>b</sup>	Constrain 1 <sup>c</sup>		Constrain 2 <sup>d</sup>	
	Number	Number	%	Nimber	%
01	3940	2575	65	2092	53
02	3940	2770	70	1259	32
03	3940	2624	67	1646	42
04	3940	2808	71	1147	29
05	3940	2824	72	1343	34
06	3940	2535	64	1267	32
07	3940	2699	69	1358	34
08	3940	2611	66	1031	26
09	3940	2897	74	1454	37
10	3940	2853	72	1438	36
11	3940	2953	75	1453	37
12	3940	2744	70	1294	33
13	3769	2239	59	1023	27
14	3769	2201	58	1092	29
15	3769	2350	62	1193	32
16	3769	2297	61	1169	31

<sup>a</sup>Quadrant ID

<sup>b</sup>Total number of images at the begining of the data analysis

<sup>c</sup>Image quality cut based on the seeing, number of images and background distributions

<sup>d</sup>Image quality cut undertaken during the photometric calibration process

### 3.4.5 Time stamp

The time stamp note present in the headers (such as DATE-OBS, JUL-DATE, LST, MJD-DATE) of all LAIWO images was incorrect for several periods of observations. First, time shifts of one/two hours were present due to switch to Israel summer/winter daylight savings time as described in the "Wise Observatory One Meter Telescope Manual"<sup>10</sup>. Secondly, accumulated error of 125 sec was reported on July 27, 2009. To compute correct Julian Date (JD) we relayed on the DATE-OBS keyword and followed the time shifts recipe of the observatory manual. Using the JULDATE function in IDL and the corrected DATE-OBS values we computed JD for each image.

## 3.5 Detrending

Transit surveys are prone to several systematic errors which affect the photometric accuracy and lower the detections number of transit events. Taking exposures of a fixed field of the sky over long stretches of the night requires the telescope to monitor through significant airmass changes. In addition, wide fields of view (such as the LAIWO field of view) permit differential cloud pattern to additionally complicates the photometric accuracy. Temperature variations can affect the telescope optics and the detector performance. Flat field errors and instrumental effects specific for the telescope and detector (such as internal reflection, dewar haze, etc.) can also lower the photometric quality of the data. Several methods have been developed to identify, measure and remove all of these effects present in transit search data. We choose to apply the publicly available SYSREM algorithm (Tamuz et al. 2005), which in breaf identifies and subtracts out linear trends appearing in a large portion of light curves in a given data set.

We applied SYSREM to the LAIWO light curves that have been produced using the differential photometry procedure to remove any survived systematics. To measure the improvement of the light curves scatter we calculated the magnitude root mean scatter (rms) before and after applying SYSREM. Figure 3.19 displays the scatter decrease (in %) for each light curve as a function of the average magnitude. For most of the detrended light curves we found an improvement of  $\sim 0.5\%$ , especially towards the fainter end.

---

<sup>10</sup>see Section 5.5, "Time Stamp"

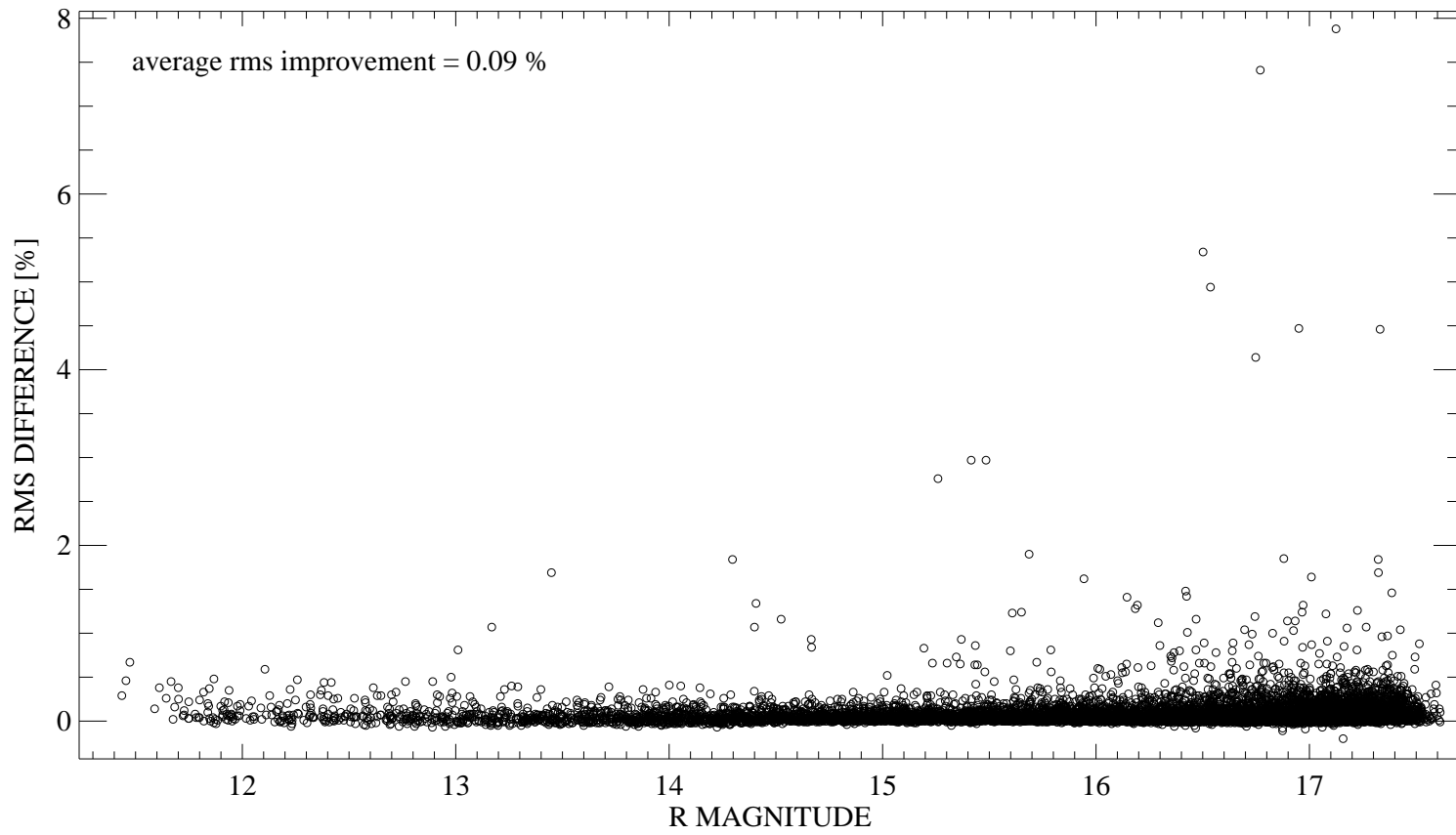


Figure 3.19 Scatter improvement after SYSREM application as a function of the stellar magnitude. Each point originates from a single light curve.

Table 3.2 BLS configuration parameters.

#	PARAMETER	VALUE	UNIT
1	Minimum frequency	0.1	[ <i>day</i> <sup>-1</sup> ]
2	Maximum frequency	2.0	[ <i>day</i> <sup>-1</sup> ]
3	Number of frequencies	1500	–
4	Number of bins	500	–
5	Minimum fractional transit length <sup>a</sup>	0.01	–
6	Maximum fractional transit length	0.1	–

<sup>a</sup>Transit duration-to-period ratio

## 3.6 Detection of variability

We undertook a periodic signal search in all LAIWO-V light curves using two independent approaches. First we attempted to detect shallow ( $\leq 4.5\%$ ), transit-like (box-shaped) periodicities that could be produced by transiting exoplanets. The second approach aimed to identify sinusoidal-shaped periodic signals with a wide range of amplitudes. Astronomical objects such as eclipsing binaries or pulsating stars could generate light curves with that shape.

### 3.6.1 Transit search

To detect transit events we applied an implementation of the box-fitting least squares<sup>11</sup> (BLS) transit search algorithm (Kovacs et al. 2002). It attempts to fit a box-shaped model (approximation of a transit-like event) to the data, while cycling through a range of orbital periods and phases. The transit event with the highest significance was selected. We adopted the experience of the OGLE team and set the BLS configuration parameters to those listed in Table 3.2.

BLS was executed for each of the sixteen LAIWO quadrants separately. On average the algorithm took  $\sim 5$  sec to detect a periodic event per light curve. Light curves with  $SDE^{12} > 3$  and  $S/N > 8$  were selected as promising transit candidates. We also imposed

<sup>11</sup>developed and tested by Maximiliano Moyano

<sup>12</sup>Signal Detection Efficiency

the condition for each detected candidate to contain not less than three transit events. Figures 3.20, 3.21 and 3.22 display three of the identified candidates.

After the described procedure and constraining criteria we were left with a total of 484 transit-like light curves, which were further visually examined for the presence of a characteristic transit shape and depth. We identified 22 possible transit candidates and many false detections, showing periods of about one day or multiple of that number (i.e.  $\sim 2$ ,  $\sim 3$ , etc). The transit properties and the equatorial coordinates of the candidates are reported in Tables 3.3 and 3.4. The corresponding phase-folded light curves are presented in Appendix A. All of the twenty two light curves showed variability with periods  $< 7$  days and transit depths of 4.5% or less. Most probably many of them might be produced by astrophysical false positives (mainly eclipsing binaries). Therefore, we performed a careful inspection of the transit candidates, based on the photometric and catalog data to reveal such impostors, without the need for further telescope time.

Table 3.3 Catalog of the detected transit candidates in the LAIWO-V field.

ID <sup>a</sup>	LAIWO-ID <sup>b</sup>	Period <sup>c</sup> [day]	Epoch <sup>d</sup> [day]	Depth <sup>e</sup> [mag]	Duration <sup>f</sup> [day]
01	LAIWO_V_01_lc_00408	4.21544	2454967.21491879	0.00970	0.41305
02	LAIWO_V_02_lc_00002	5.77829	2454968.92006818	0.00770	0.54296
03	LAIWO_V_02_lc_00735	3.03675	2454875.57854129	0.01460	0.20632
04	LAIWO_V_02_lc_00750	1.70453	2454874.63887036	0.00430	0.11249
05	LAIWO_V_03_lc_00643	4.44273	2454965.82484315	0.00530	0.33496
06	LAIWO_V_04_lc_00004	1.81039	2454968.28822877	0.00940	0.17565
07	LAIWO_V_06_lc_00624	6.56389	2454877.63460602	0.00740	0.46100
08	LAIWO_V_06_lc_00808	2.22654	2454875.89193963	0.00670	0.20910
09	LAIWO_V_07_lc_00647	2.87834	2454874.59044466	0.00670	0.22107
10	LAIWO_V_08_lc_00704	1.98738	2454986.51984609	0.02700	0.19457
11	LAIWO_V_09_lc_00651	1.37680	2454874.58727359	0.00810	0.13217
12	LAIWO_V_09_lc_00749	1.45099	2454875.74737468	0.02360	0.09863
13	LAIWO_V_09_lc_00811	3.03377	2454875.69243809	0.00630	0.23659
14	LAIWO_V_10_lc_00179	2.41823	2454876.27411655	0.00790	0.23698
15	LAIWO_V_10_lc_00796	4.47490	2454877.90454062	0.00620	0.29532
16	LAIWO_V_11_lc_00121	1.62925	2454874.73150199	0.01130	0.15962
17	LAIWO_V_11_lc_00803	2.21497	2454876.17086785	0.01050	0.21691
18	LAIWO_V_12_lc_00240	3.95509	2454970.67972506	0.00480	0.23948
19	LAIWO_V_12_lc_00747	3.87936	2454970.42730956	0.01700	0.36447
20	LAIWO_V_14_lc_00189	2.65683	2454875.77226211	0.00870	0.22681
21	LAIWO_V_15_lc_00078	2.00479	2454875.04195617	0.00630	0.17093
22	LAIWO_V_15_lc_00438	2.62133	2454874.59892374	0.00550	0.13103

<sup>a</sup>Transit candidate identification number (LAIWO-V-TR-ID);

<sup>b</sup>Internal light curve identification number(used during the data analysis); It consists of the field ID (LAIWO\_V), the quadrant number and the light curve number.

<sup>c</sup>Orbital period of the transit candidate in days.

<sup>d</sup>Mid-transit central time (JD).

<sup>e</sup>Transit depth in magnitudes.

<sup>f</sup>Transit duration in days.

Table 3.4 Catalog and visual properties of the LAIWO-V transit candidate host stars.

ID <sup>a</sup>	R.A.(J2000) [hh mm ss]	DECL.(J2000) [dd mm ss]	B <sup>b</sup> [mag]	V <sup>b</sup> [mag]	R <sup>b</sup> [mag]	J <sup>b</sup> [mag]	H <sup>b</sup> [mag]	K <sup>b</sup> [mag]	$\mu_\alpha^b$ [mas/yr]	$\mu_\delta^b$ [mas/yr]
01	17 19 32.30	−0 13 45.63	14.72	13.81	13.39	12.032	11.612	11.521	+12.5	−14.8
02	17 19 02.83	−0 33 57.17	15.79	14.93	14.62	13.301	12.885	12.772	−23.8	+08.5
03	17 18 52.89	−0 29 26.93	15.94	14.95	14.55	12.624	11.972	11.847	−02.5	−12.7
04	17 19 44.76	−0 29 46.94	15.06	—	13.88	12.584	12.255	12.183	+03.2	+04.6
05	17 19 56.41	−0 10 14.46	14.73	13.71	13.27	11.218	10.631	10.497	−06.4	−05.9
06	17 20 07.28	−0 33 59.48	15.92	15.10	14.59	13.046	12.468	12.324	−06.7	−06.1
07	17 19 08.57	+0 26 47.16	15.71	14.69	14.24	12.285	11.678	11.457	−09.1	−05.4
08	17 19 13.81	+0 23 49.92	14.10	13.86	13.68	12.240	11.899	11.794	−03.5	−05.8
09	17 19 52.63	+0 47 03.92	14.95	13.94	13.78	12.259	11.947	11.775	+12.8	−03.7
10	17 20 20.26	+0 26 37.98	17.78	16.89	16.60	15.196	14.714	14.615	−12.0	−10.0
11	17 23 42.74	+0 27 21.20	15.95	15.33	14.58	13.948	13.625	13.412	+00.0	+00.0
12	17 24 19.18	+0 26 14.11	18.30	17.72	15.62	14.231	13.557	13.320	+00.0	+00.0
13	17 23 53.49	+0 25 15.85	15.92	15.07	14.53	12.887	12.394	12.166	−09.1	−00.7
14	17 24 24.97	+0 39 08.65	15.90	14.95	14.57	12.808	12.195	12.060	−00.1	−01.8
15	17 23 37.60	+0 47 27.85	15.29	13.98	13.65	11.355	10.577	10.379	−00.9	−10.2
16	17 22 35.58	+0 34 33.95	14.69	14.04	13.79	12.081	11.577	11.422	−04.3	+01.8
17	17 22 58.64	+0 25 57.15	16.23	15.22	15.04	13.645	13.255	13.111	−00.4	+02.9
18	17 22 40.18	+0 39 42.93	14.60	13.66	13.40	11.412	10.880	10.716	−11.3	−01.2
19	17 22 49.02	+0 47 11.50	16.10	15.47	14.96	13.777	13.449	13.289	+03.1	+03.7
20	17 24 26.01	−0 16 43.28	13.99	13.21	13.07	11.645	11.389	11.233	−01.7	+05.1
21	17 22 43.31	−0 20 59.00	15.92	14.87	14.46	12.845	12.325	12.170	+25.4	−01.2
22	17 22 44.05	−0 26 10.77	15.06	13.88	13.22	11.156	10.527	10.383	−10.3	+18.1

<sup>a</sup>Same as in Table 3.3.<sup>b</sup>All magnitudes and proper motions were identified after a match with the PPMXL astronomical catalog (available at <http://vo.uni-hd.de/ppmxl>), Roeser et al. 2010.

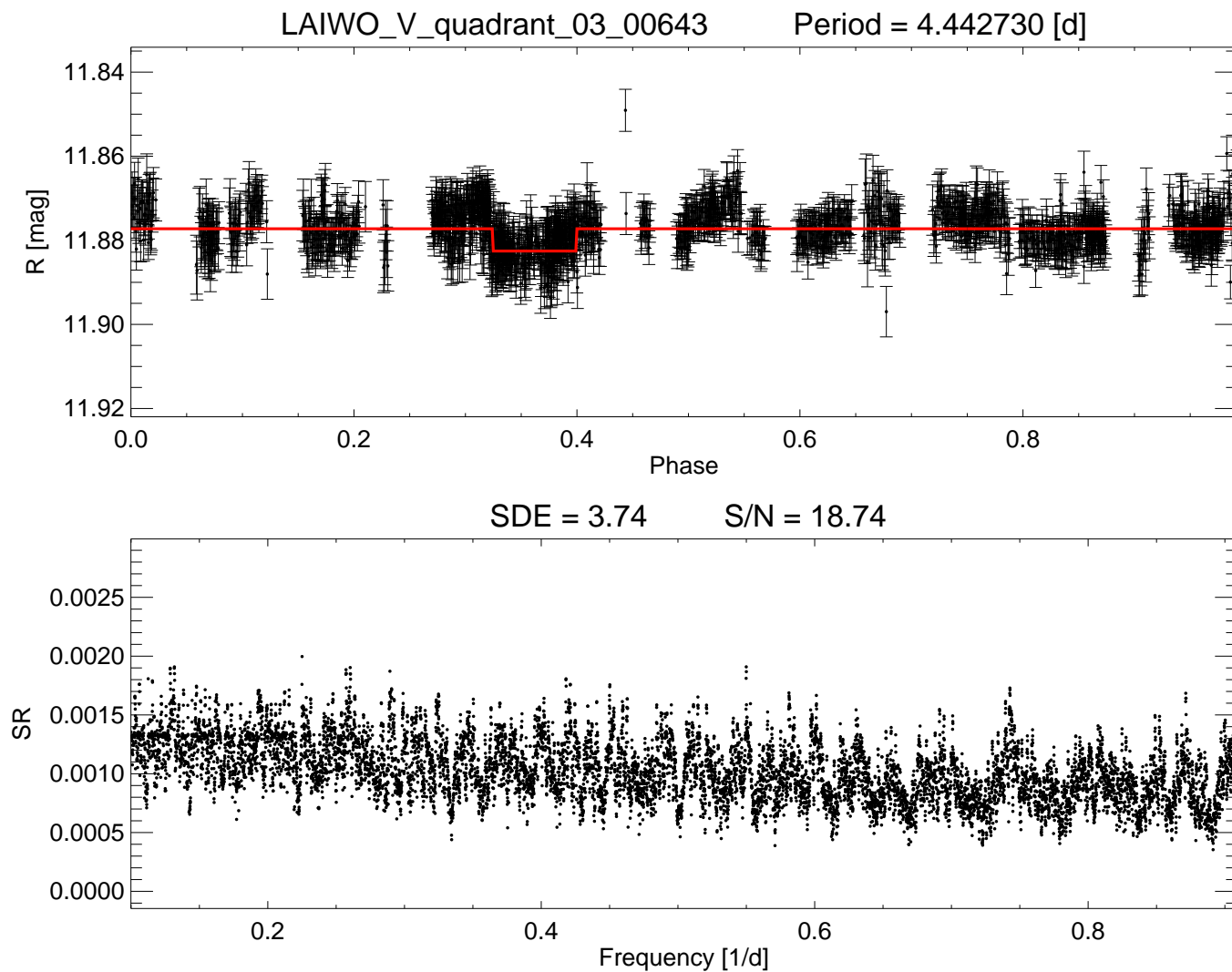


Figure 3.20 Phase-folded light curve (upper panel) and BLS spectrum (lower panel) of the transit candidate LAIWO-V-TR-05, identified in the third quadrant. The BLS model is over-imposed with the red continuous line. The highest peak in the BLS spectrum is located at  $\sim 0.23$  days, while the smaller ones correspond to harmonics and subharmonics.



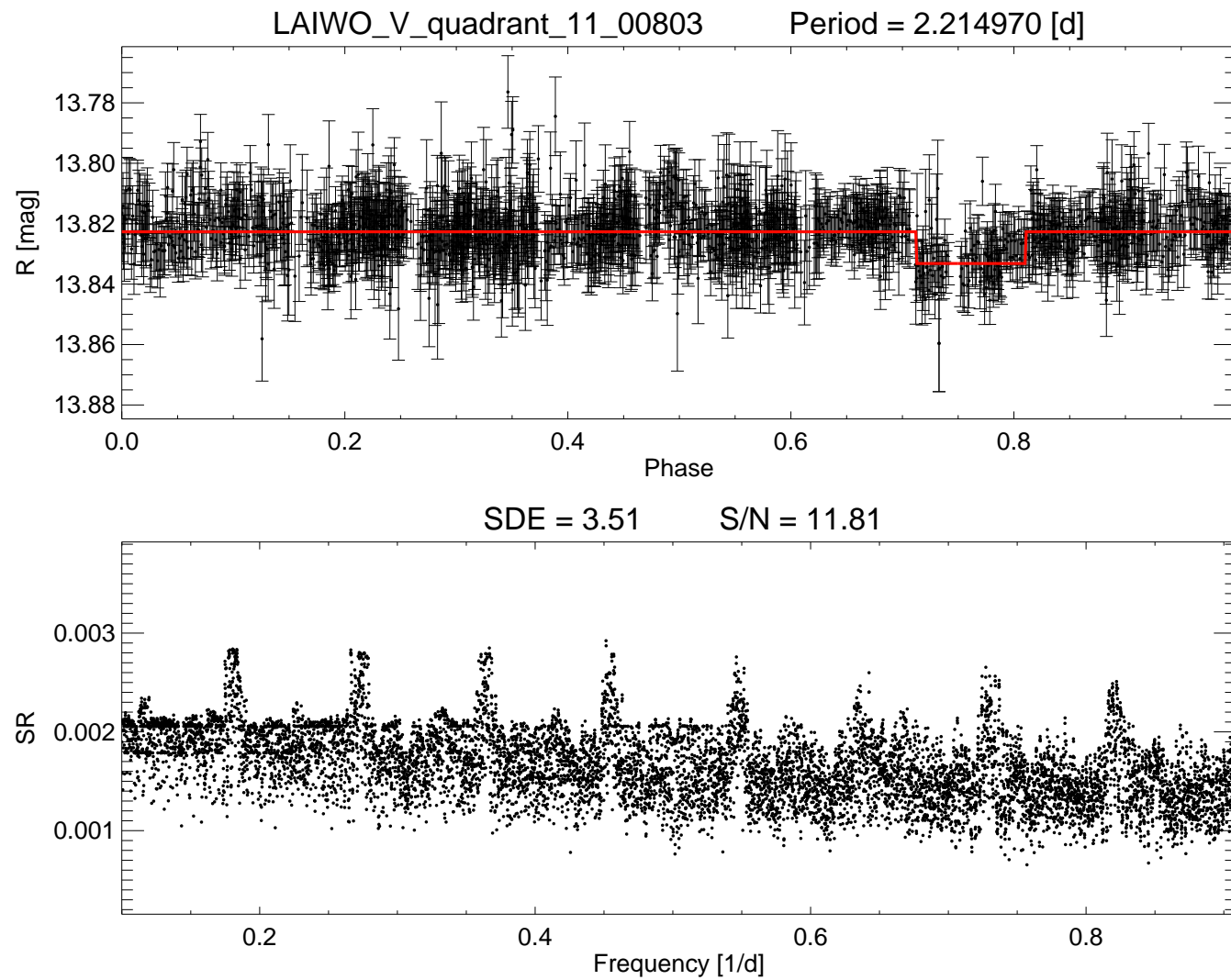


Figure 3.21 Phase-folded light curve (upper panel) and BLS spectrum (lower panel) of the transit candidate LAIWO-V-TR-17, identified in the third quadrant. The BLS model is over-imposed with the red continuous line. The highest peak in the BLS spectrum is located at  $\sim 0.45$  days, while the smaller ones correspond to harmonics and subharmonics.

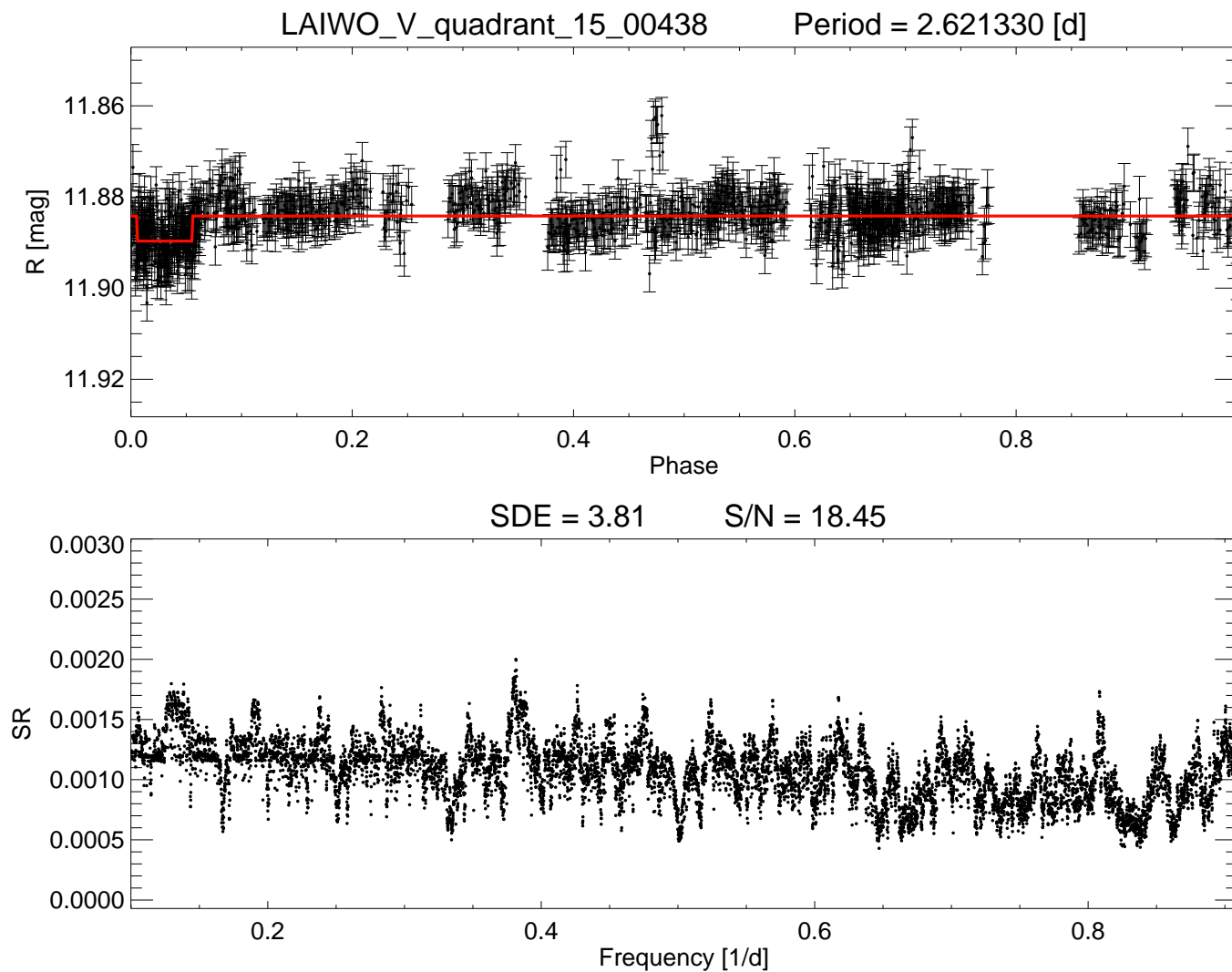


Figure 3.22 Phase-folded light curve (upper panel) and BLS spectrum (lower panel) of the transit candidate LAIWO-V-TR-22, identified in the third quadrant. The BLS model is over-imposed with the red continuous line. The highest peak in the BLS spectrum is located at  $\sim 0.38$  days, while the smaller ones correspond to harmonics and subharmonics.

Table 3.5 Configuration parameters used in the Lomb-Scargle periodogram analysis.

#	PARAMETER	VALUE	UNIT
1	Minimum period	0.1	[ <i>day</i> ]
2	Maximum period	6.0	[ <i>day</i> ]
3	Period resolution	0.01	[ <i>day</i> ]

### 3.6.2 Variable stars

To detect periodic variable stars we took use of the Lomb-Scargle algorithm (Lomb 1976, Scargle 1982) as implemented in the VARTOOLS program<sup>13</sup> (Hartman et al. 2008). The Lomb-Scargle periodogram analysis is particularly suited to non-uniformly sampled time series, such as our data set. Table 3.5 displays the main configuration parameters, which we adopted in the signal search. Typically, the program converged after  $\sim 30$  sec per light curve. A total of 20 clear detections of periodic variable stars were identified. In several cases the Lomb-Scargle algorithm computed a harmonic of the real period, therefore we do not report here the exact period (Table 3.6). The phase-folded light curves of all periodic variables detected in the analysis are presented in Appendix B.

None of the detected in our data periodic variable stars were found in the General Catalog of Variable Stars,<sup>14</sup> the VIZIER<sup>15</sup> or the SIMBAD<sup>16</sup> databases.

The light curve morphology of several periodic variables, such as Cepheid or eclipsing binaries, is indicative for their types. Therefore, most of our periodic variables permit a rough classification, based on characteristic light curve shapes, amplitudes and variability periods.

We identified the light curves of LAIWO-V-VAR-6, LAIWO-V-VAR-10 and LAIWO-V-VAR-11 as examples of short-period pulsating variables (type RR-Lyraes). First, the specific asymmetric shape of the three light curves is similar to the one indicative for RR Lyra-type pulsating stars. Secondly, the light curves of the three variables indicated very short periods ( $\sim 0.64$ ,  $\sim 0.54$  and  $\sim 0.57$  days) and variability amplitudes ( $\sim 0.2$ ,  $\sim 0.4$  and  $\sim 0.3$  mag) within the expected period ( $< 1$  day) and amplitude (0.2 to 2.0 mag)

<sup>13</sup>available at <https://www.cfa.harvard.edu/~jhartman/vartools/>

<sup>14</sup><http://www.sai.msu.su/groups/cluster/gcvs/gcvs/>

<sup>15</sup><http://archive.ast.cam.ac.uk/vizier/>

<sup>16</sup><http://simbad.u-strasbg.fr/simbad/>

ranges for the RR-Lyraes. Third, an analysis of the  $(B - V)$ ,  $(V - R)$  and  $(B - R)$  colors of the three stars indicated late A-, late A- and late F-type spectral classes, which is also consistent with RR-Lyra variables. This type of radial pulsating stars are stable and extensively used as distance indicators in astronomy. Assuming a mean absolute magnitude  $\sim 0.6 \pm 0.2$  mag (Smith 2004) and the average apparent  $V$  magnitudes of our variables ( $\sim 16.5$ ,  $\sim 14.7$  and  $\sim 15.5$ ), we estimated the distances to the three objects to  $\sim 16$ ,  $\sim 6$  and  $\sim 10$  kpc, respectively. However, here it should be pointed out that we did not take into account the interstellar extinction, which decreases the observed magnitudes and causes overestimated distances. Finally, the small proper motions of the three stars (see Table 3.6) were consistent with distant objects.

The light curve shape of LAIWO-V-VAR-17 is a "classic" example of Algol-type eclipsing binary, which consists of two stars of nearly equal size and significantly different temperatures (surface brightness). The deeper minimum observed in the light curve corresponds to an eclipse of the brighter component (the primary) due to the shade of the cooler secondary. In addition, due to the very short period ( $\sim 0.7$  days) the shape of the both components of the binary are expected to be elongated (ellipsoidal). This suggests ellipsoidal variability (see Chapter 2) which is also observed in the out-of-eclipse parts of the light curve of that star. Algol-type and eclipsing binaries in general are important in astronomy as they provide a unique opportunity to measure accurate stellar masses beyond the Solar system.

LAIWO-V-VAR-3 was identified as an eclipsing contact binary of *WUma*<sup>17</sup> type (see Chapter 2). Similar stellar binaries consist of two components which share a common outer layer. The later makes it impossible to indicate a clear begin or accomplishment of the stellar eclipses (if observed). Furthermore, the common layer is the reason *WUma* eclipsing binaries to show identical stellar types. Usually the components are two F-type MS dwarfs. Our analysis of the  $B - V$ ,  $V - R$  and  $B - R$  color indexes showed a clear indication of F-type star.

The light curves of LAIWO-V-VAR-1, 4, 5, 7, 8, 9, 12, 13, 14, 15, 16, 18, 19 and 20 could also be classified as contact binaries. However, their light curves were more noisy, which makes the classification more imprecise.

It is a well-known fact that transit search surveys discover many periodic variable stars, among which of great interest are eclipsing binaries composed of an F dwarf and

---

<sup>17</sup>W Ursae Majoris

---

an M dwarf (or F/M systems). Such systems produce transit-like light curves which are practically indistinguishable from those produced by Jupiter-like planets around Solar-type stars. However, the detection of such objects is one of the most valuable byproducts of the transit searches as the F/M systems permit determination of the masses of the M-dwarf component to a very good precision and therefore sample the lower end of the stellar mass function to unprecedented accuracy (Mandushev et al. 2006).

Table 3.6 Catalog and visual properties of the periodic variables identified in the LAIWO-V field.

ID <sup>a</sup>	R.A.(J2000) [hh mm ss]	DECL.(J2000) [dd mm ss]	B <sup>b</sup> [mag]	V <sup>b</sup> [mag]	R <sup>b</sup> [mag]	P <sup>c</sup> [day]	$\mu_{\alpha}^b$ [mas/yr]	$\mu_{\delta}^b$ [mas/yr]
01	17 19 24.99	-0 07 20.02	18.10	17.88	16.83	0.84034592	-12.0	+00.0
02	17 20 38.36	-0 08 23.24	16.64	16.52	16.35	0.28112860	+00.0	+00.0
03	17 19 22.37	-0 22 21.57	14.67	14.23	13.91	0.55388850	-19.1	-00.1
04	17 23 26.61	+0 37 19.80	17.54	17.84	17.34	0.40153480	-04.0	-04.0
05	17 19 15.12	-0 30 25.64	18.86	30.00	17.92	0.37802506	-04.0	+04.0
06	17 23 41.98	+0 40 22.30	17.26	16.47	16.29	0.63700299	-14.0	+02.0
07	17 19 27.79	+0 32 32.28	17.43	16.99	16.19	0.13987056	+00.0	+10.0
08	17 23 37.67	-0 08 21.09	17.45	17.47	16.81	0.16889769	+00.0	+00.0
09	17 22 56.85	-0 25 01.79	17.63	17.24	16.88	0.14628549	+00.0	+00.0
10	17 20 45.25	-0 05 27.54	15.14	14.65	15.00	0.54312713	-03.5	-08.7
11	17 19 55.34	-0 -16 20.73	16.14	15.46	14.97	0.56918687	-04.7	-10.3
12	17 24 05.00	-0 -10 54.11	18.54	30.00	17.77	0.18681728	+00.0	+00.0
13	17 24 01.05	+0 49 13.59	18.21	17.37	16.49	1.07222387	+06.0	+06.0
14	17 18 52.16	-0 09 48.56	17.15	16.35	16.01	0.62245192	+00.0	+00.0
15	17 19 01.87	-0 09 33.36	18.49	30.00	17.56	0.33007800	-24.0	-04.0
16	17 24 29.69	+0 50 40.42	16.17	15.22	14.83	3.75942422	-05.3	+04.7
17	17 20 17.75	+0 37 06.93	15.04	14.81	14.49	0.69009922	+03.5	-17.4
18	17 22 57.01	-0 28 17.88	17.20	17.30	15.38	0.24930976	+00.0	+00.0
19	17 23 25.84	-0 24 30.03	17.69	17.05	15.07	5.20262108	+10.0	+08.0
20	17 24 11.05	-0 27 50.22	16.09	15.62	30.00	0.24932609	+02.9	-13.9

<sup>a</sup>Periodic variable star identification number (LAIWO-V-VAR-ID).<sup>b</sup>All magnitudes and proper motions were identified after a match with the PPMXL astronomical catalog (available at <http://vo.uni-hd.de/ppmxl>), Roeser et al. 2010.<sup>c</sup>Orbital period (or harmonic).

## 3.7 Transit light curve analysis

### 3.7.1 Overlap with previous transit surveys

To perform an analysis of the transit candidates identified in the present survey we undertook the following steps. First a cross-search for an overlap between our detections and any of the announced transiting exoplanets<sup>18</sup> was performed. No matches were identified.

### 3.7.2 Size estimation

Secondly, we assumed that each of the transit events, present in the exoplanet candidates light curves were produced by transiting objects (planets, sub-stellar companions or stars). To estimate the size of the transiting body we first attempted to characterize the astrophysical parameters of the host star. We relayed on the available color information after a match of the equatorial coordinates of our stars with the PPMXL catalog. Based on the available  $UBV$  magnitudes we computed the  $(B-V)$ ,  $(V-R)$  and  $(B-R)$  colors. After a comparison with tabulated values, available in Kraus & Hillenbrand (2007), we identified the corresponding stellar spectral types and radii, assuming that all of the host stars are on the main sequence. We found in most of the cases a consistency between the three spectral types. However, some exceptions such as stars 09, 10, 11, 12, 17 and 20 showed a huge discrepancy between the three estimations. The reason for such inconsistency could be explained with a presence of stellar blends. The later occur when the starlight, originating from stars with different spectral types is mixed. For example, a combination of unresolved grazing eclipsing binary<sup>19</sup> and a single star, located nearly in the same direction on the sky produce a stellar blend.

Once we had the stellar spectral types and the corresponding radii estimates, we computed an approximate size of the transiting object. To perform this analysis we measured the transit depths directly from the light curves and plugged the numbers

---

<sup>18</sup>Available at the *Extrasolar Planet Encyclopedia*: <http://exoplanet.eu/>

<sup>19</sup>Those are normal eclipsing binaries whose orbital planes are viewed at tilted angles with respect to the line-of-sight.

in relation (1.2). We report the results in Table 3.7. It becomes clear from the radii estimations that each of the transiting events could be produced by transiting Jupiter- or Saturn-size planets.

To compare the sizes of our candidates with all confirmed transiting exoplanets up to date, we build the radii and orbital periods distributions for both sets (Figures 3.23 and 3.24). The first figure indicates that most of our transit candidates are located in a relatively low populated area in the radius distribution of the known exoplanets. It is evident from the second distribution that the LAIWO survey has sampled nearly the same range of orbital periods as the one based on the confirmed transiting planets.



Table 3.7 Astrophysical parameters of the host stars and radii of the transiting candidates.

ID	$B - V$	$SpT_{BV}^a$	$B - R$	$SpT_{BR}^b$	$V - R$	$SpT_{VR}^c$	$SpT$	$R_*/R_\odot$	$R_p/R_J$
01	0.910	K2V	1.330	K1V	0.420	G8V	K0V	0.85	0.81
02	0.860	K1V	1.170	G8V	0.310	G0V	G6V	0.91	0.78
03	0.990	K3V	1.390	K1V	0.400	G5V	K0V	0.85	1.00
04	—	—	1.180	G8V	—	—	G8V	0.88	0.56
05	1.020	K4V	1.460	K2V	0.440	G8V	K1V	0.83	0.59
06	0.820	K0V	1.330	K1V	0.510	K1V	K1V	0.83	0.78
07	1.020	K4V	1.470	K2V	0.450	K0V	K2V	0.81	0.68
08	0.240	F0V	0.420	F0V	0.180	F1V	F0V	1.50	1.19
09	1.010	K3V	1.170	G8V	0.160	F0V	G4V	0.95	0.76
10	0.890	K2V	1.180	G8V	0.290	F8V	G6V	0.91	1.45
11	0.620	G2V	1.370	K1V	0.750	K6V	K0V	0.85	0.74
12	0.580	G0V	2.680	M3V	2.100	M9V	K7V	0.68	1.02
13	0.850	K1V	1.390	K1V	0.540	K2V	K1V	0.83	0.64
14	0.950	K3V	1.330	K1V	0.380	G4V	G9V	0.87	0.75
15	1.310	K6V	1.640	K4V	0.330	G0V	K0V	0.85	0.65
16	0.650	G3V	0.900	G0V	0.250	F4V	G2V	1.00	1.03
17	1.010	K3V	1.190	K1V	0.180	F1V	G5V	0.92	0.92
18	0.940	K3V	1.200	K1V	0.260	K5V	K3V	0.79	0.53
19	0.630	G2V	1.140	G8V	0.510	K1V	G7V	0.90	1.14
20	0.780	G8V	0.920	G2V	0.140	B9V	F6V	1.27	1.15
21	1.050	K4V	1.460	K2V	0.410	G7V	K1V	0.83	0.64
22	1.180	K6V	1.840	K6V	0.660	K5V	K6V	0.70	0.51

<sup>a</sup>Using the  $(B - V)$  color and assuming MS stars.<sup>b</sup>Using the  $(B - R)$  color and assuming MS stars.<sup>c</sup>Using the  $(V - R)$  color and assuming MS stars.

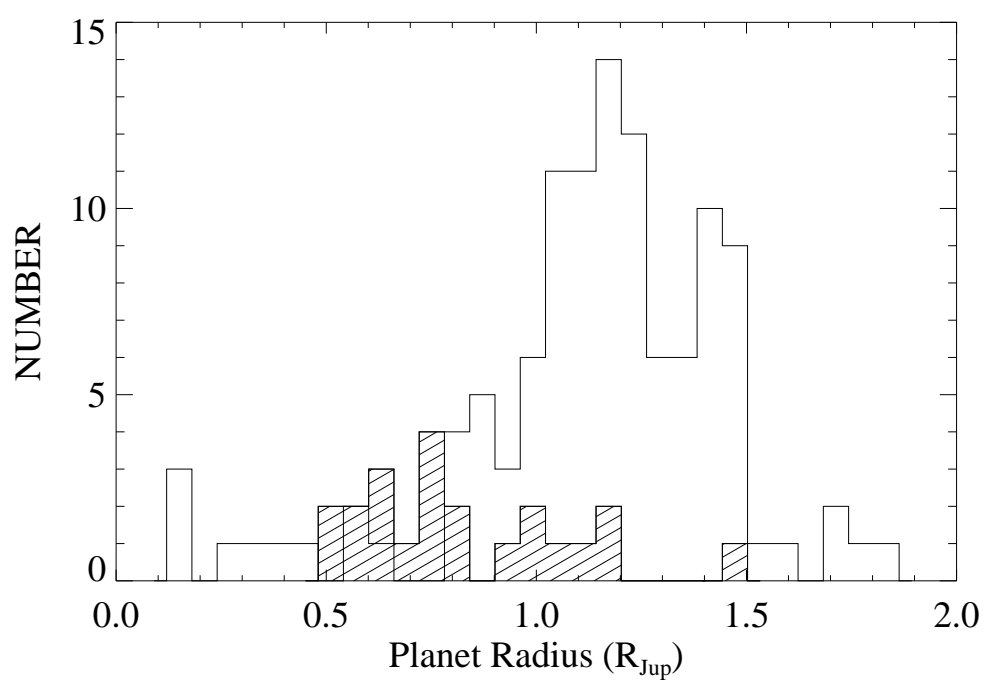


Figure 3.23 Planetary radii distributions of the LAIWO-V transit candidates (shaded area) and the confirmed transiting exoplanets (unshaded area).

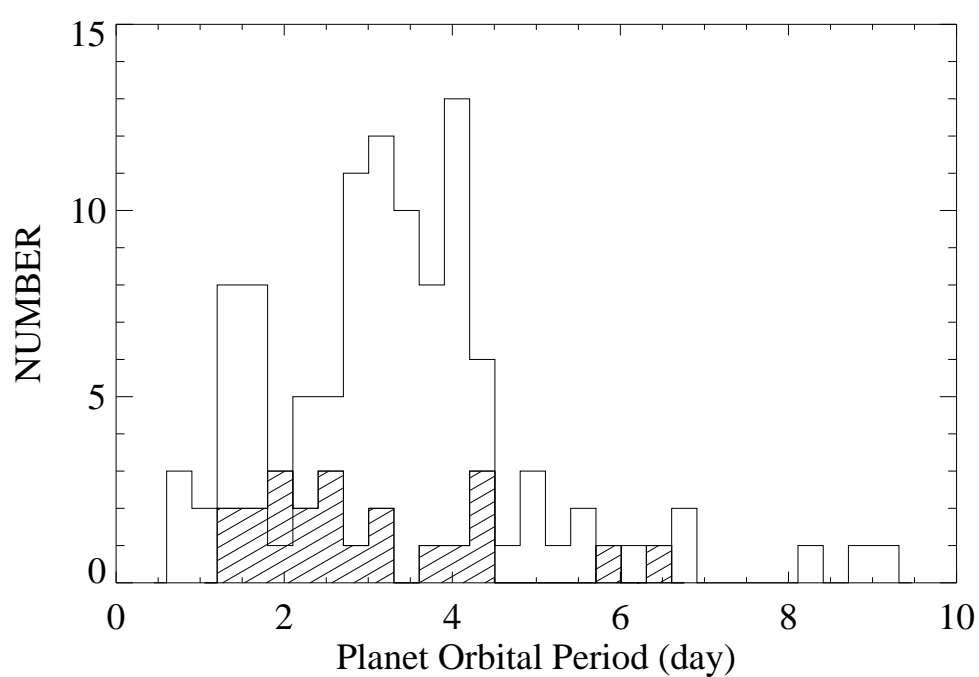


Figure 3.24 Planetary orbital periods distributions of the LAIWO-V transit candidates (shaded area) and the confirmed transiting exoplanets (unshaded area).

### 3.7.3 Exoplanet diagnostic ( $\eta$ )

The transit data alone permits some additional analysis regarding the nature of the transit candidates. As it was shown in Chapter 2, based on the transit period, depth and duration one can compute the exoplanet diagnostic ( $\eta$ ) in order to identify promising candidates (Figure 3.25). If we stick to the rule that only the real exoplanets fall below the cutoff line, there are a total of two promising candidates (LAIWO-TR-V-4 and LAIWO-TR-22). However, it should be pointed out that at the quality level of our transit light curves it would be challenging to perform accurate measurements of the transit duration or even depth. Therefore, we must release the cutoff and consider all candidates below  $\sim 2$ , i.e. excluding only four of the initial candidates list.

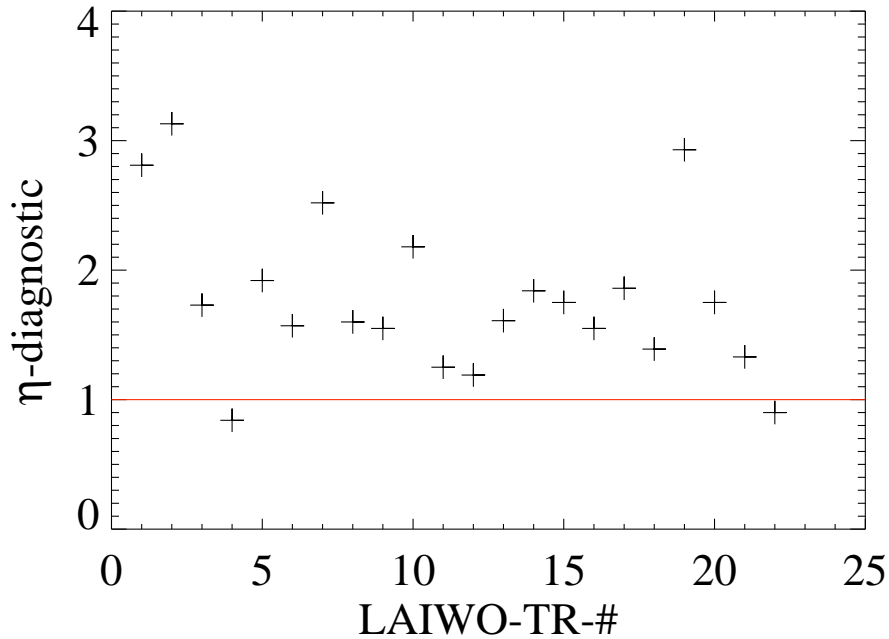


Figure 3.25 Exoplanet  $\eta$ —diagnostic computed for the LAIWO transit candidates. The red continuous line represents the cutoff below which transiting extrasolar planets should fall.

### 3.7.4 Ellipsoidal variability

We considered the out-of-eclipse data points of each transit candidate light curve and evaluated the amplitude of the ellipsoidal variability. To fit the non-linear five-parameter ( $I, a_{c1}, a_{c2}, a_{s1}, a_{s2}$ ) model to the phase-folded light curves, we ran our program described in Chapter 2 (see for details). As a second approach, we also invoked the MARQ<sup>20</sup> function in IDL to minimize the  $\chi^2$  statistic over the data. The MARQ utility reached convergence very fast (typically for a few fractions of a second per light curve) and output the best-fit parameters with one-sigma errors. We produced almost indistinguishable results from both approaches. The amplitude of the ellipsoidal variability and the one sigma error bars are reported in Table 3.8.

The transit candidate LAIWO-V-TR-10 has significant ellipsoidal variability, indicating a massive, not planetary companion. Among the remaining candidates LAIWO-V-TR-12 and LAIWO-V-TR-1 show also high value for the  $a_{c2}$  term and should not be considered as planet hosts.

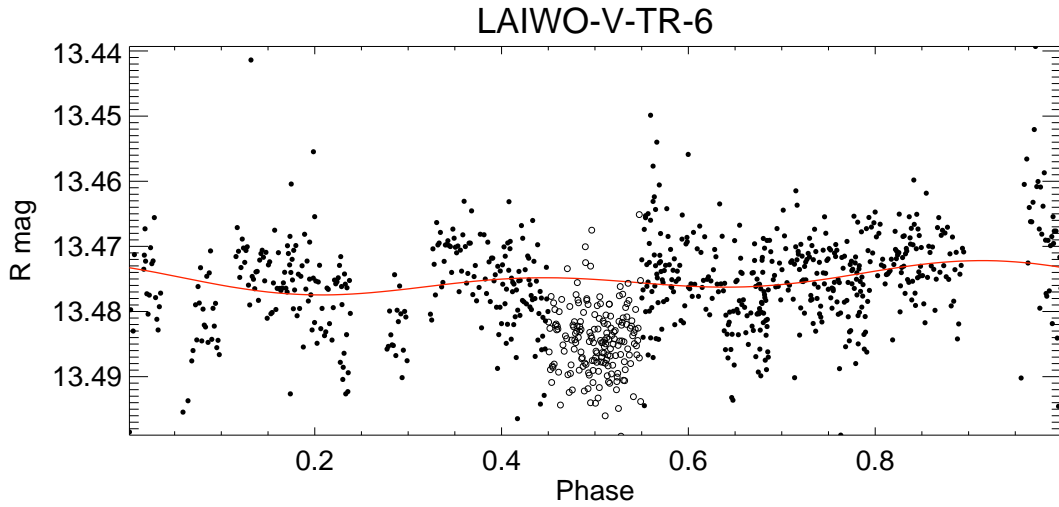


Figure 3.26 The light curve of the transit candidate LAIWO-V-TR-6 is shown with the ellipsoidal variability model (continuous line). The empty circles were removed during the fit to prevent any bias due to points in the transit.

<sup>20</sup>based on the Marquardt method described in Bevington, P. R. & Robinson, D. K. 1992, Data Reduction and Error Analysis for the Physical Sciences, 2e (New York:McGraw Hill), p. 161.

Table 3.8 List of transiting objects with estimated amplitude of the ellipsoidal variability.

ID	$a_{c2}^a$	$\sigma^b$	$\chi^2$
	[mmag]	[mmag]	
LAIWO-V-TR-1	2.819	0.196	0.890
LAIWO-V-TR-2	0.493	0.471	0.800
LAIWO-V-TR-3	0.859	0.361	0.728
LAIWO-V-TR-4	0.621	0.240	0.629
LAIWO-V-TR-5	0.075	0.196	0.925
LAIWO-V-TR-6	0.967	0.456	0.789
LAIWO-V-TR-7	0.583	0.246	0.525
LAIWO-V-TR-8	0.623	0.256	0.874
LAIWO-V-TR-9	1.018	0.237	0.568
LAIWO-V-TR-10	16.563	2.618	1.282
LAIWO-V-TR-11	0.098	0.416	1.171
LAIWO-V-TR-12	3.009	0.861	1.584
LAIWO-V-TR-13	0.072	0.318	0.875
LAIWO-V-TR-14	0.488	0.290	0.655
LAIWO-V-TR-15	0.425	0.233	0.895
LAIWO-V-TR-16	0.276	0.223	1.112
LAIWO-V-TR-17	0.888	0.383	0.635
LAIWO-V-TR-18	0.710	0.192	0.822
LAIWO-V-TR-19	0.189	0.572	0.767
LAIWO-V-TR-20	0.107	0.208	1.743
LAIWO-V-TR-21	1.509	0.591	0.822
LAIWO-V-TR-22	0.116	0.212	1.115

<sup>a</sup>Amplitude of the ellipsoidal variability.<sup>b</sup>Uncertainty of the ellipsoidal amplitude

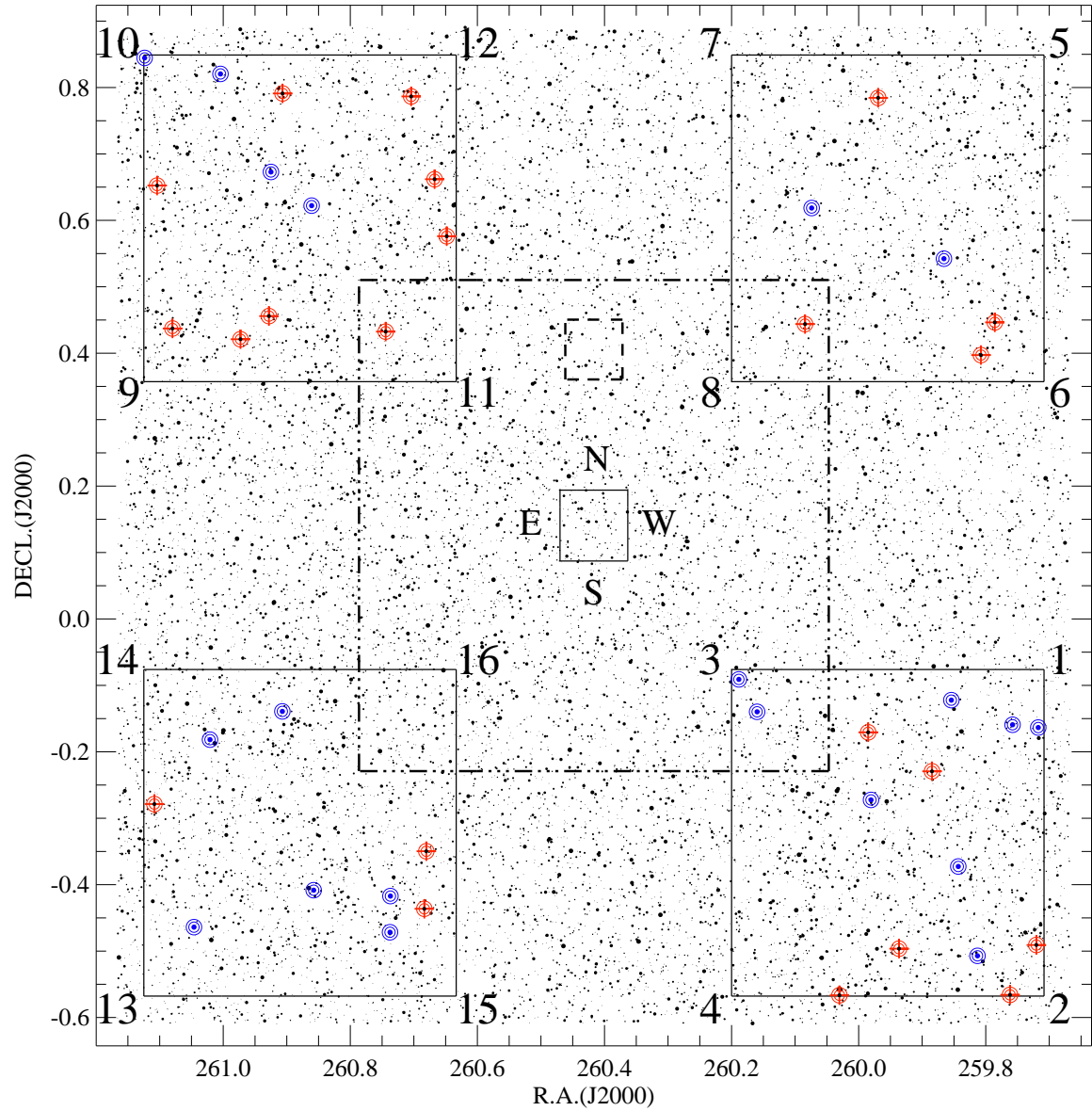


Figure 3.27 Positions of the transit candidates (red crossed circles) and periodic variables (blue circles) identified in the LAIWO-V field. The points represent all matched stars (11-18 mag) with the PPMXL stellar catalog. To compare the fields of view, the layouts of the LAIWO, LAICA and GROND instruments are indicated respectively with continuous, dash-dotted and hatched lines.

### 3.8 Planetary candidates summary and proposed scheme for efficient follow-up

We have analyzed over 16,000 stars, spread in a field of view  $\sim 1$  square degree on the sky. Among them we have identified 22 objects with periodic, small photometric variations (1 – 2%) in their light curves. As such repetitive dips might be produced by transiting planets we estimated their sizes and concluded that they all are consistent with the size of Jupiter in our Solar System. Furthermore, we computed the exoplanet diagnostic ( $\eta$ ) and showed that only two candidates fall below the cutoff line (i.e.  $\eta < 1$ ). Finally, we estimated the ellipsoidal variability of each candidate and concluded that only three showed evidences for a presence of massive companions. Taking into account the entire analysis we concluded that our subset of transit candidates should contain between zero and two light curves produced by real transiting planets. We identify LAIWO-V-TR- 4, 5, 9, 15, 18, 22 candidates as most promising and propose a follow up scheme for further screening.

The effort and time that need to be settled in the follow-up observations and analysis of transit candidates is large. Therefore, a well-organized plan must be prepared in order to efficiently use the time needed for the mass determination of the planetary transits. Sorted from the cheapest to the more expensive and sophisticated methods, every transit candidate should verify:

1. **Low signal-to-noise radial velocity (RV).** An efficient method to reject the majority of false positive transit detections, produced by eclipsing binaries is to obtain 1–2 or more high resolution spectra with low signal-to-noise ratio ( $S/N \sim 25$ ). Double or single-lined eclipsing binaries and rapidly rotating stars may immediately be eliminated based on a single spectrum. Transit candidates produced by stellar eclipses present high RV amplitudes (typically  $\geq 5$  km/s). Furthermore, a presence of changes in the shape of the spectral line profile is indicative for stellar triples (Latham et al. 2009, Bakos et al. 2011). Finally, when available the stellar spectral information provides accurate astrophysical characterization of the host stars (such as  $T_{eff}$ ,  $\log g$ ,  $[Fe/H]$ ,  $age$  and  $mass$ ), which is critical for the correct planetary size estimation.

A RV follow up of the LAIWO transit candidates may be performed using the



FEROS echelle spectrograph, mounted on the ESO/MPG 2.2m telescope at La Silla Observatory. The instrument has a high resolving power ( $R \sim 48,000$ ), which permits precise RV measurements down to  $\sim 11$  m/s. The apparent  $V$  magnitudes of each of our targets are similar to  $V \sim 13.8$ , which would allow  $\sim 50$  min integrations with FEROS, depending on the weather.

2. **Multicolor transit photometry.** If produced by an exoplanet passage the transit depth measured from the light curve must be achromatic. Most of the triple stellar systems can be detected with  $\sim 1\%$  multicolor photometry.

A multicolor photometric follow up of our targets may easily be carried out on using the GROND<sup>21</sup> camera at the ESO/MPG 2.2m telescope at La Silla Observatory. The instrument is unique as it permits a simultaneous multicolor observations in four optical (Sloan  $g', r', I', z'$ ) and three NIR ( $JHK$ ) channels. The fields of view in the optical ( $5.4' \times 5.4'$ ) and NIR ( $10'/times 10'$ ) filters would cover our transit candidates along with reference stars needed for the differential photometry.

Furthermore, the LAICA<sup>22</sup> wide field camera, mounted on the 3.5m telescope at the Calar Alto Observatory (CA) may also be involved in the multicolor photometric follow up. The large collective power (3.5m) and field of view ( $44.36' \times 44.36'$ ) of that instrument would enable a high cadence observations of several transit candidates in the wide range of the telescope optical pass bands. Figure 3.27 displays the positions of the transit candidates and periodic variables identified in the LAIWO-V field as they appear on the sky along with the fields of view of the LAIWO, GROND and LAICA instruments.

3. **High signal-to-noise radial velocities and bisector analysis.** The final stage of the confirmation follow-up strategy is to obtain high-resolution, high  $S/N$  spectra with sufficient velocity precision to detect the orbital variation of the star due to the gravitational influence of a planet. These measurements are used to study false alarms which were hard to investigate at the previous two steps. Furthermore, if present variations of the line bisector enables one to reject transit candidates as produced by low-mass companion objects. The later cause radial velocity variations in the residual of the modeled data.

---

<sup>21</sup>Gamma Ray Optical and Near Infrared Detector

<sup>22</sup>Large Area Imager for the Calar Alto Observatory

Spectra with high signal-to-noise ratios can be obtained at big telescopes equipped with high-resolution spectrographs such as the High Resolution Echelle Spectrometer (HIRES) on the 10m Keck I telescope, the High Dispersion Spectrograph (HDS) on the Subaru 8.2m or the Ultraviolet and Visual Echelle Spectrograph (UVES) on the 8.2m Keck telescope (UT2, VLT).

## Chapter 4

---

# Multi-band Photometry of WASP-4

### 4.1 Introduction

WASP-4b is one of the first transiting extrasolar planets detected in the southern sky by the SuperWASP-South. The giant planet is slightly heavier than Jupiter ( $1.24 M_{\text{Jup}}$ ) orbiting a G7V star with a period of 1.34 days (Wilson et al. 2008; Gillon et al 2009; Winn et al. 2009). This transit discovery is interesting because the planet has unusually large radius, short orbital period; and the host star is one of the brightest ( $V = 12.5$ ) among exoplanet hosts in the southern hemisphere. The exoplanet WASP-4b is an attractive target for precise ground based photometric transit observations, as it causes significant ( $\sim 4\%$ ) transit depth. In addition, the planet is expected to generate a rather strong signal while hiding behind the star, during secondary eclipses. The later present an observational opportunity for measurements of the planet's reflected light, emergent thermal radiation and orbital eccentricity constraints.

The low southern declination of WASP-4 makes it an ideal target for many telescopes located in the southern hemisphere. In this chapter we report transit observations of WASP-4 with the ESO/MPG 2.2m telescope. Our motivation was to derive independent parameters for this interesting system and to perform precise measurements of the midtransit times, which can be used to detect the presence of additional planets in the system (Holman & Murray 2005). Driven by the same motivation Gillon et al. (2008) and Winn et al. (2009) observed transits of WASP-4 with respectively one of the 8.2m Very Large Telescopes (VLTs) and the Magellan/Baade 6.5 m telescope.

## 4.2 Observations

Prior to observations, we used the ephemeris presented in Wilson et al. (2008) to compute midtransit times of the WASP-4b exoplanet. We selected five transits, observable at sufficiently low air-mass from the ESO/MPG 2.2 m telescope at La Silla observatory in Chile and prepared an observing program. Initially, it was planned to gather data during five transits, however due to bad weather observations were not allowed during two of the scheduled nights.

We observed three transits of WASP-4b on August 25 and 29 and October 07 2009 with the Gamma Ray Burst Optical and Near-Infrared Detector (GROND), which is a gamma-ray burst follow-up instrument (Greiner et al. 2008). GROND allows simultaneous photometric observations in four optical (Sloan  $g'$ ,  $r'$ ,  $i'$ ,  $z'$ ) and three near-infrared ( $JHK$ ) filters.

In the optical channels the telescope and the GROND camera provided a field of view of  $5.4' \times 5.4'$  with a pixel scale of  $0''.158 \text{ pixel}^{-1}$ . Each observing night we verified that WASP-4 and a nearby comparison star were within GROND's field of view. The comparison star was  $\sim 1.3'$  south-east from our target (Winn et al. 2009). For each night we obtained repeated integrations of WASP-4 and the comparison star for  $\sim 3.5$  hr, bracketing the predicted central transit times. The exposure time were in the range 8–14 sec, depended on the weather conditions. During all observations we used the fast readout mode ( $\sim 10$  sec), achieving a cadence ranging from 18 to 24 sec. To minimize systematics in the photometry associated with the PSF ( $x, y$ ) position on the CCD chip, the autoguider was switched on. However, technical reasons prevented its usual work, causing  $\sim 35\%$  unguided exposures from the total number of collected images.

At the beginning of the August 25 and 29 observations WASP-4 rose from an air-mass of 1.02 and 1.05, respectively which increased monotonically to 1.5 and 1.6 at the end of the runs. During the October 7 observations the air-mass decreased from 1.06 to 1.02 and then increased to 1.15 at the end of the observing run.

In the near-infrared (NIR) channels, due to technical constraints, the maximal exposure time is limited to 10 s. This integration time was not long enough to obtain the sufficient signal-to-noise ratio for accurate light curves. As we carried out all observations without dithering to increase the cadence and to minimize systematics in the photometry, it was not possible to stack groups of NIR images with prior background subtraction. Therefore,

we excluded the NIR data in the further analysis.

### 4.3 Data reduction and photometric analysis

We used standard IRAF procedures to perform bias and dark current subtraction and flat fielding for each optical channel. Median combined bias was computed using 22 zero-second exposure frames and 4 dark frames were used to calculate the master dark. A master flatfield was calculated after a median combination of 12 twilight flats.

Aperture photometry of WASP-4 and the reference star was performed on each calibrated image. To produce the differential light curve of WASP-4 its magnitude was subtracted from that of the comparison star. Fortunately, the later was of similar color and brightness, which reduced the effect of differential color extinction. We experimented with various aperture sizes and sky areas, aiming to minimize the scatter <sup>1</sup> in the out-of-transit (OOT) part of WASP-4 differential light curve. Best results were obtained with aperture radii of 16, 20.5 and 17.5 pixels for the August 25 and 29 and October 7 dates, respectively.

To decrease systematic effects that influence the quality of our light curves, we undertook the following steps. First, for each date and channel individually, we modeled the magnitude vs. air-mass of the OOT portions of the light curves to correct for differential air-mass ( $z$ ) extinction. The function we used was of the form:

$$f(z) = a + bz, \quad (4.1)$$

where  $a$  and  $b$  are constants. We then applied this correction to both the transit and the OOT data. Figure 4.1 displays the results after each step of the described process for the r'-channel data obtained on October 7 2009.

Second, following this correction we noticed that the fluxes of our target and the comparison star showed a nearly linear correlations with the x or y positions of the centroid of the stellar PSF on the chips. We removed these near-linear trends from the data of WASP-4 and the reference star by performing a linear fit to the x and y positions of the centroid of the PSF and the normalized flux of the OOT photometry. The function we

---

<sup>1</sup>measured by the magnitude root-mean-square (r.m.s)

used to model the flux of the OOT data was of the form:

$$f(x, y) = 1 + k_x x + k_y y + k_{xy} xy, \quad (4.2)$$

where  $k_x$ ,  $k_y$  and  $k_{xy}$  are constants. Then, we subtracted the fit from the photometry of each date and channel. No other trends that were correlated with instrumental parameters were found.

## 4.4 System parameters

We fitted the light curves using the analytic models of Mandel & Agol (2002). The set of parameters included the planet-to-star size ratio ( $R_p/R_*$ ), the normalized orbital semimajor axis ( $a/R_*$ ), the orbital inclination ( $i$ ) and the central transit time ( $T_c$ ).

We assumed a quadratic stellar limb darkening law (see equation 2.5, Section 2.2.2, Chapter 2) and selected the coefficients from Claret (2004) according to the astrophysical properties of our star: effective temperature  $T_{eff} = 5500$  K, metallicity  $[Fe/H] = -0.03$ , surface gravity  $\log g = 4.48$ , which were provided from Winn et al. (2009).

We find the values of the parameters that minimize the  $\chi^2$  statistic (see equation 2.6 in Chapter 2) using the AMOEBA algorithm (Press et al. 1992, p.408). As initial values for the parameters we choose: midtransit times provided by our initial ephemeris of Wilson et al. (2008),  $R_p/R_* = 0.15$ , orbital inclination  $i = 90^\circ$  and  $a/R_* = 10$ .

To estimate the uncertainties in the fitted parameters we used the Bootstrap Monte Carlo Method (Press et al. 1992). It generates a large number ( $\sim 10^5$ ) of light curves by resampling a given observational set with repetitions. Then each light curve is modeled and the resulting parameter distributions provide error estimates. However, we point out that in our error analysis of the fitted parameters we did not incorporate any contribution of correlated low frequency noise (Pont et al. 2006). Therefore, the errors might probably be underestimated.

## 4.5 Results

In Table 4.1. we present WASP-4 system parameters derived from the best fit. The values for the planetary radius agree within one sigma without the one derived from the g' band, which is slightly smaller. The numbers for the normalized planet-to-star orbital distance also agree except for the z' band, for which a higher value is favored.

Based on our results we estimated the absolute values of the planetary radius and the orbital semimajor axis. We adopted the value for the stellar radius  $R_* = 0.912 \pm 0.013 R_\odot$  from Winn et al. (2009). For the planetary radius we found  $R_p = 1.39 \pm 0.05 R_{Jup}$  and for the orbital semimajor axis  $a = 0.023 \pm 0.002$  AU. Both results are in good agreement with previous estimates. Figures 4.2, 4.3 and 4.4. display the transit light curves and the best-fit models.

Using the three transits we performed a joint period fit and derived the following ephemeris:

$$T_c[HJD] = 2453934.957509(\pm 0.00027) + 1.33822870(\pm 3.68 \times 10^{-5}) \times E \quad (4.3)$$

Finally, we combined the three midtransit times, measured from our data with all previous references and computed the observed (O) minus calculated (C) values to search for transit timing variations. The result is reported on Figure 4.5. Here epoch -880 corresponds to the first observed transit epoch of WASP-4b, derived by Wilson et al. (2008). Epoch 0 corresponds to the October 7, 2009 observation. The O-C diagram suggests no significant transit timing variations.

Table 4.1 Results for the planet-to-star size ratio, the normalized semimajor axis and the inclination for the filters used. The last column contains the result from a joined fit to the entire data set.

Band:	$g'$	$r'$	$i'$	$z'$	combined
$R_p/R_*$	0.1548	0.1563	0.1568	0.1571	0.1569
	$\pm 0.0008$	$\pm 0.0005$	$\pm 0.0005$	$\pm 0.0005$	$\pm 0.0008$
$a/R_*$	5.46	5.27	5.31	5.70	5.39
	$\pm 0.17$	$\pm 0.13$	$\pm 0.13$	$\pm 0.14$	$\pm 0.09$
$i^\circ$	87.95	87.68	87.84	87.73	87.82
	$\pm 0.31$	$\pm 0.29$	$\pm 0.27$	$\pm 0.24$	$\pm 0.14$



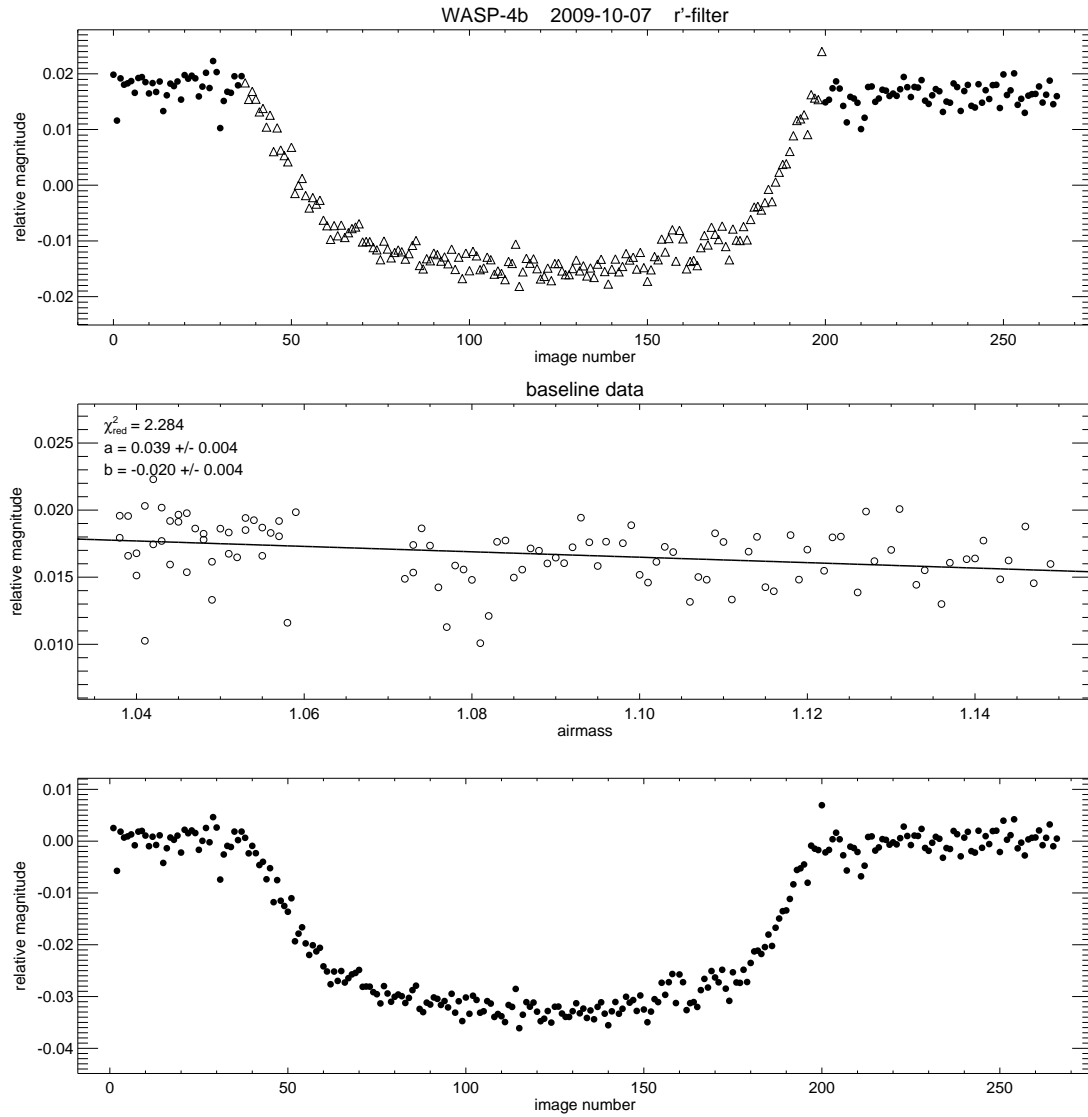


Figure 4.1 Differential air-mass extinction correction of the r'-band photometry of WASP-4, obtained on October 7, 2009. *Top panel*: uncorrected baseline and transit flux measurements are indicated with dots and triangle symbols, respectively; *middle pannel*: out-of-transit data with the linear fit; *bottom pannel*: corrected data.

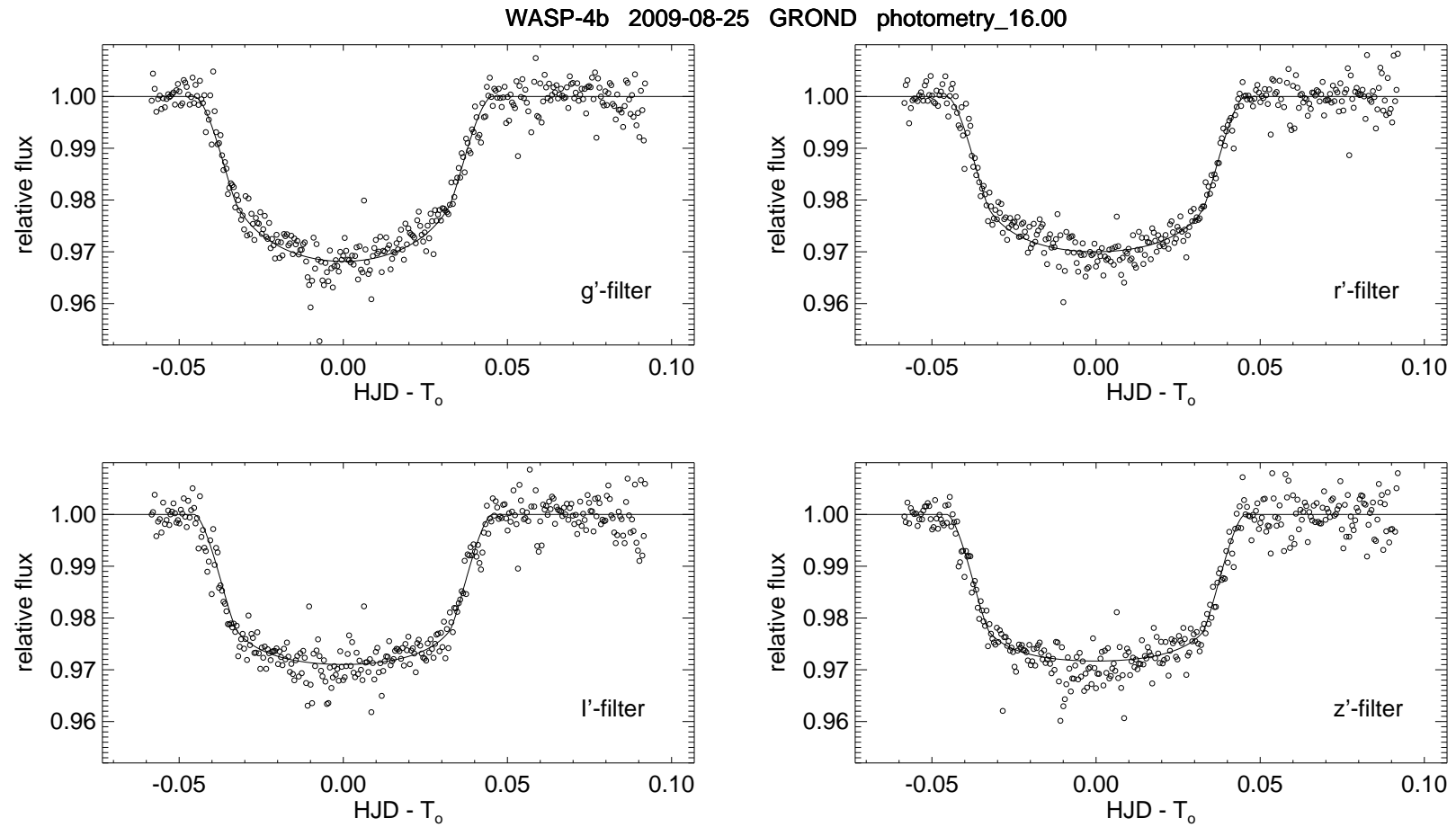


Figure 4.2 The light curves of WASP-4 in the four optical channels obtained during the night of August 25 2009. The radius of the aperture used to measure the star flux is indicated in the plot title. The continuous lines represent the best fit to the data.

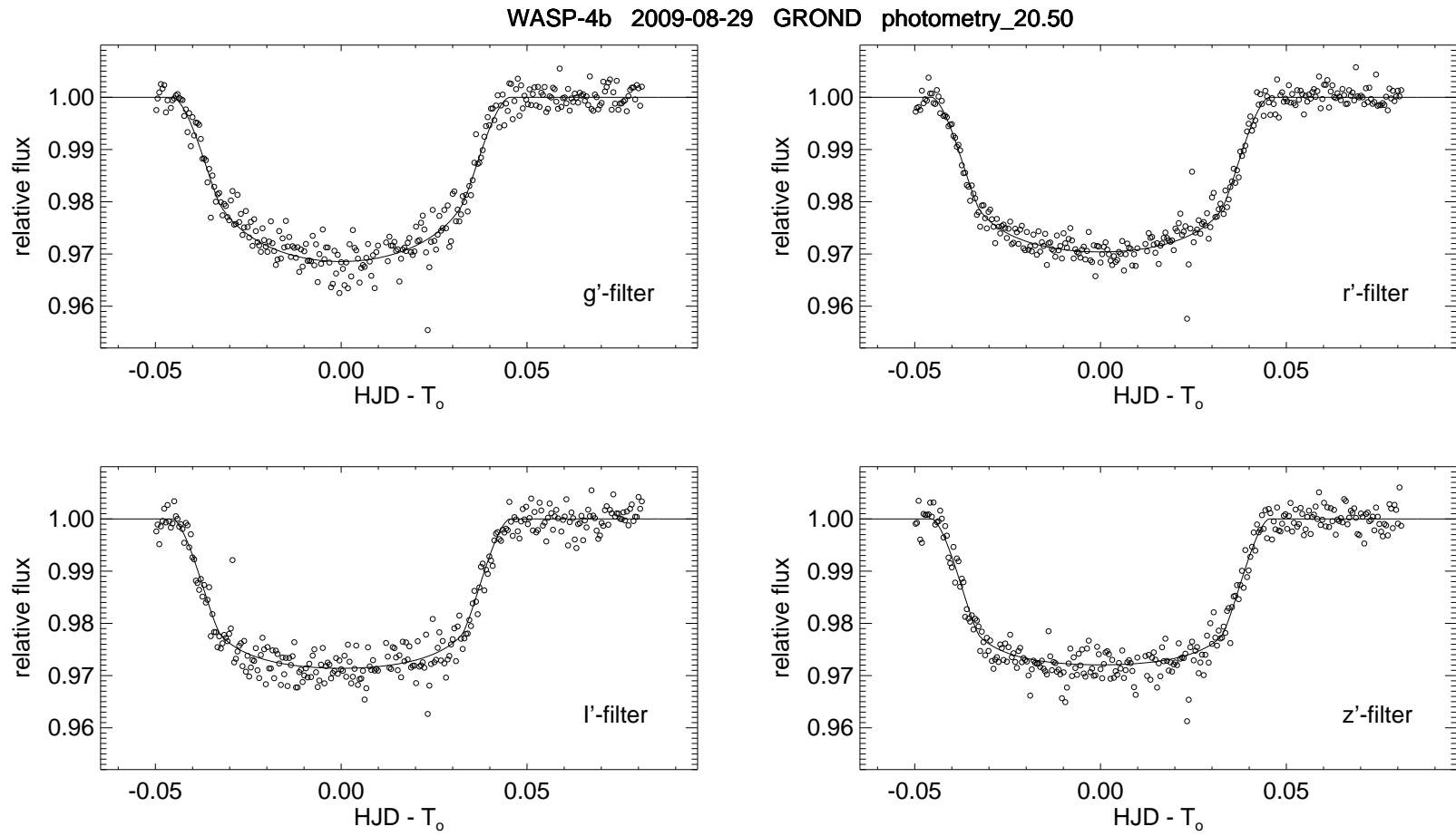


Figure 4.3 The light curves of WASP-4 in the four optical channels obtained during the night of August 29 2009. The radius of the aperture used to measure the star flux is indicated in the plot title. The continuous lines represent the best fit to the data.

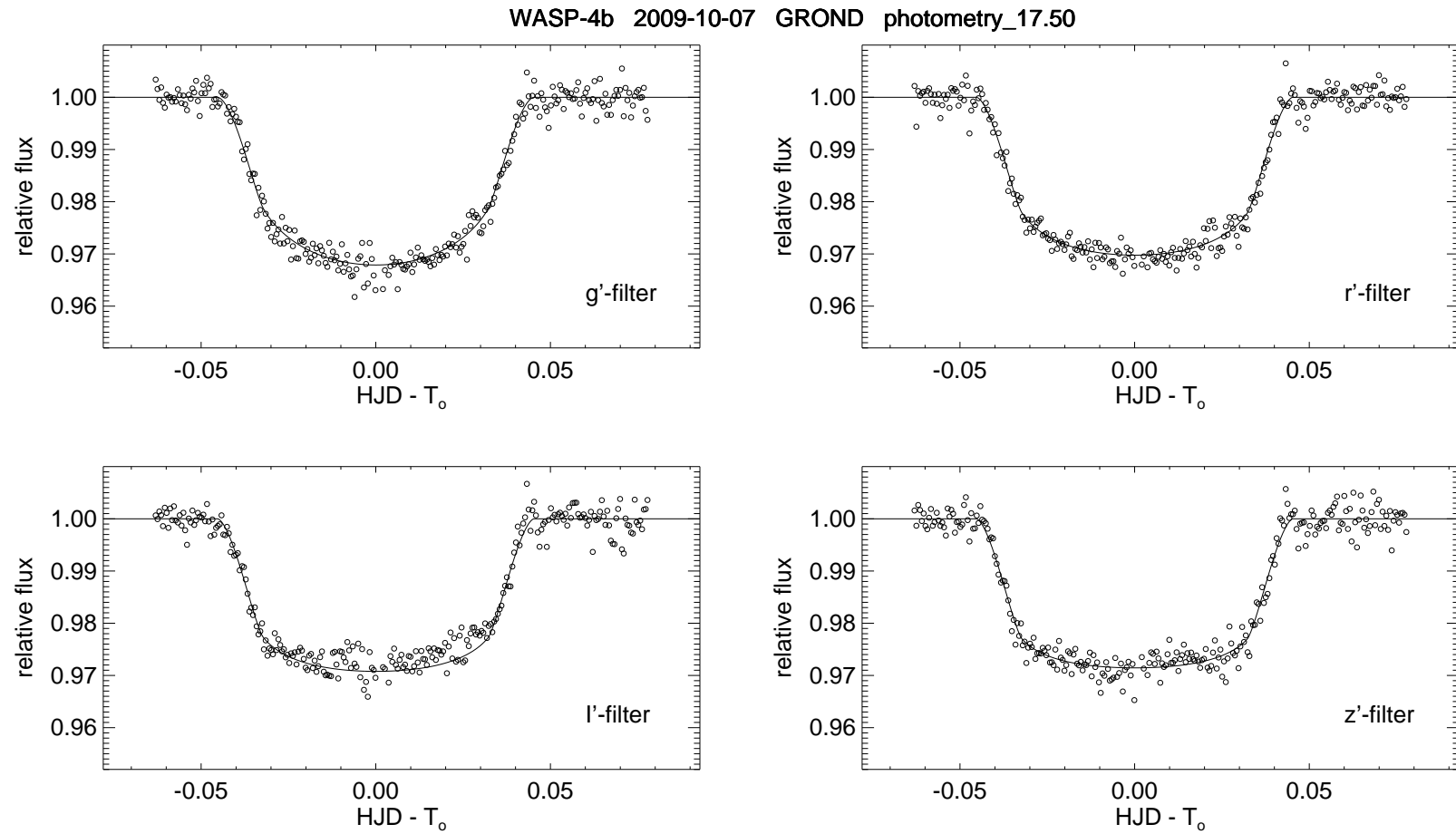


Figure 4.4 The light curves of WASP-4 in the four optical channels obtained during the night of October 7 2009. The radius of the aperture used to measure the star flux is indicated in the plot title. The continuous lines represent the best fit to the data.

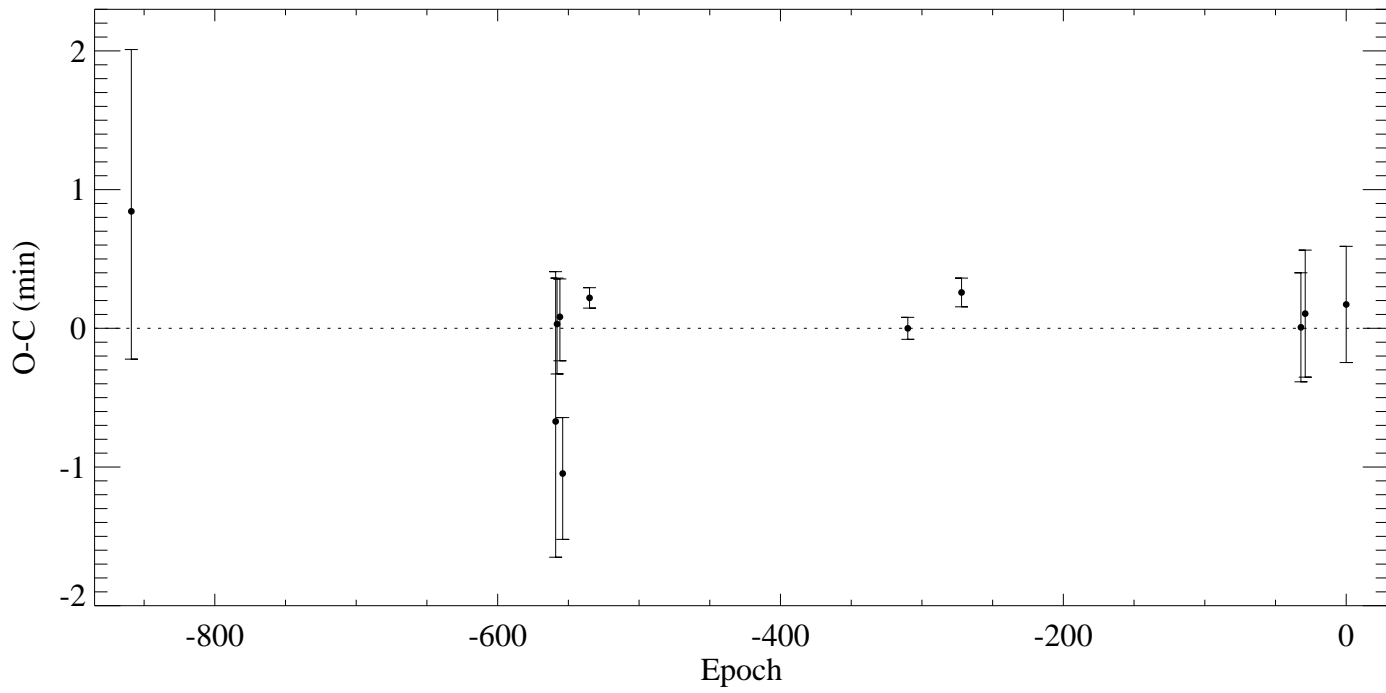


Figure 4.5 O-C diagram based on the orbital period and the mid-transit times derived from our data and previous observations.



---

## Conclusions

I summarize here the main results of the work described in this thesis.

In Chapter 1 I present a description of the photometric transit method for detecting extrasolar planets, along with the main astrophysical parameters that can be determined by observing transits. I discuss the difficulties that ground-based transit surveys may face and present a brief overview of the science investigations with transiting exoplanets.

In Chapter 2 I study the most widespread cases of transit false positives and present three classification methods for the pipeline of the Pan-Planets transit survey. I implement them in an automatic pipeline and present results based on tests. To judge the efficiency of the implementation of the first method, evaluation of the out-of-eclipse ellipsoidal variability I use the OGLE data. In over 50% of the light curves I detect ellipsoidal amplitudes consistent with stellar companions, which is in agreement with previous studies. In addition, I compare my results with similar of other authors (Drake 2003, Sirko & Paczynsky 2003) and conclude an excellent consistency. I test the second method, determination of astrophysical parameters from a transit fit using a set of high quality transit light curves. I identify a maximum deviation from the tabulated values for the normalized semi-major axis. In the worst case it reaches a fractional difference of 2.8%. The remaining parameters (orbital inclination and planet-to-star size ratio) are in a very good agreement with the compared values. Finally, I test the implementation of the exoplanet diagnostic ( $\eta$ ) method. I use three data sets: OGLE, all confirmed transiting exoplanets and Pan-Planets simulations. The first test results in an excellent consistency with the one

of Tingley & Sackett (2005), identifying each of the confirmed transiting planets present in the data set. The results based on the second data set are ambiguous. Nearly half of the confirmed planets fall below the cutoff line, which can be interpreted as a weakness of the assumptions behind the derivation of the exoplanet diagnostic. The results of the last data set are similar to the second one. I identify over 54% of the planets and the remaining fall very close to the cutoff line. Viewing the results from the tests I conclude that the evaluation of the out-of-transit ellipsoidal variability is the most reliable method for identifying false positives in transit searches.

In Chapter 3 I perform a photometric analysis of over 64,000 images, produce over 16,000 light curves and identify among them 22 new transit candidates and 20 variable stars based on one and a half years of Johnson R-band observations of the LAIWO-V field in Ophiuchus. I develop an automated data processing pipeline that performs image calibration, astrometric solution, differential photometry, systematics removal and periodic signal detection.

To identify the stellar sources I compute astrometric solution of our data with the 2MASS catalog and identify the stars on each time series element with a sub-pixel accuracy.

I dramatically decrease the systematics by performing differential photometry using a set of reference stars, thoroughly examined for intrinsic variability. Furthermore, I use additional methods (SYSREM) to improve the light curves quality, which for the bright non-variable stars reaches a root-mean-square  $\sim 0.3\%$ .

To identify transit candidates and the periodic variables, I run the BLS and Lomb-Scargle algorithms respectively. The first method results in  $\sim 500$  and the second  $\sim 800$  significant detections. I select the light curves of 22 transit candidates with sufficiently high signal-to-noise and U-shaped transits with depths  $\leq 1.5\%$ . In the second set of detections I identify 20 periodic variable stars. Among them I classify a few RR Lyra-type and several eclipsing binaries.

I attempt to identify the transit candidates and variable stars respectively in other surveys and variable stars catalogs, however with negative result.

I further analyze the 22 transit light curves for ellipsoidal modulations and conclude that three of them (LAIWO-V-TR-1, LAIWO-V-TR-10 and LAIWO-V-TR-12) are consistent with stellar companions. Moreover, I analyze the photometric colors of the transit candidates host stars and estimate their spectral types and radii, assuming that they are on the main sequence. I estimate the radii of the planet candidates, using the light curve



depths and conclude that the size of all of them is consistent with the size of Jupiter in the Solar System. Finally, I estimate the exoplanet diagnostic and identify two candidates below the cutoff line. In conclusion, taking into account the entire analysis I identify six promising transit candidates with G and K spectral type stars, sufficiently bright for a reconnaissance spectroscopy with the FEROS spectrograph.

In Chapter 4 I study the physical parameters of the WASP-4b transiting exoplanet using multi-band photometry. I derive estimates of the planet radius, orbital semimajor axis and inclination. In addition, I measure the central transit times, constrain the orbital period and derive a new ephemeris. Finally, I analyze the observed minus calculated residuals of the central transit times in my data and those derived from previous observations of WASP-4. I conclude no significant transit timing variations.

In conclusion this work presents several useful results. I show that the most reliable way to rule out astrophysical false alarms in transit searches based on the photometry alone is the evaluation of ellipsoidal variability in the out-of-eclipse light curve portion. I describe a method to obtain high quality light curves from photometric time series. I show how to identify transit candidates and to further derive astrophysical parameters based on their light curves and reference catalogs. I also carry out a multi-band photometric study of WASP-4b – deriving planetary radius, orbital period, distance and inclination and finally show how to search for transit timing variations.

## Future prospects

The work I present in this thesis suggest a number of future developments. I will briefly discuss the most important cases:

- A spectroscopic follow-up study is a natural continuation of the screening process, needed for the confirmation of the transit candidates, identified in the LAIWO-V field. A few high resolution, low signal-to-noise spectra per target would immediately reveal stellar companions as they produce radial velocities of the primary of  $\geq 10$  km/s. The spectral characterization of the transit candidate host stars would provide also secure constraints on their radii and masses, which are needed for more accurate estimates of the sizes and masses of the transiting bodies.

- High signal-to-noise multicolor photometry would be required for those transit candidates that pass the spectroscopic reconnaissance. As transit events are achromatic an eventual false positive can easily be identified by examining the transit depths observed in different wavelengths.
- An examination of the radial velocity variations of WASP-4 star during transit of its planet would provide estimate of the spin-orbit alignment of the planetary orbital plane and the rotation axis of its star. WASP-4 is one of the brightest planet hosts in the southern hemisphere and its planet has a huge radius, thus it should be expected to produce a strong Rossiter-McLaughlin effect.

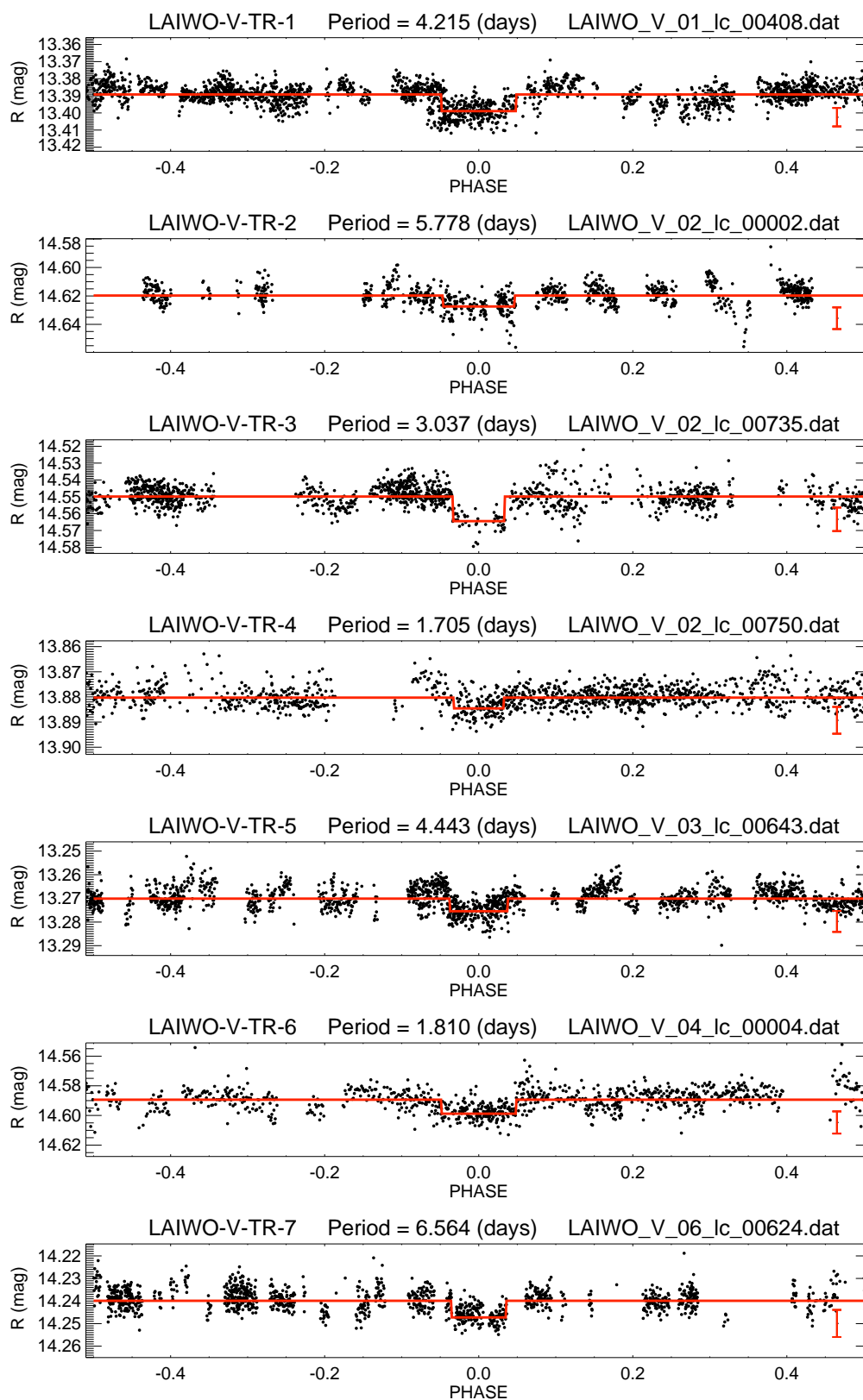
---

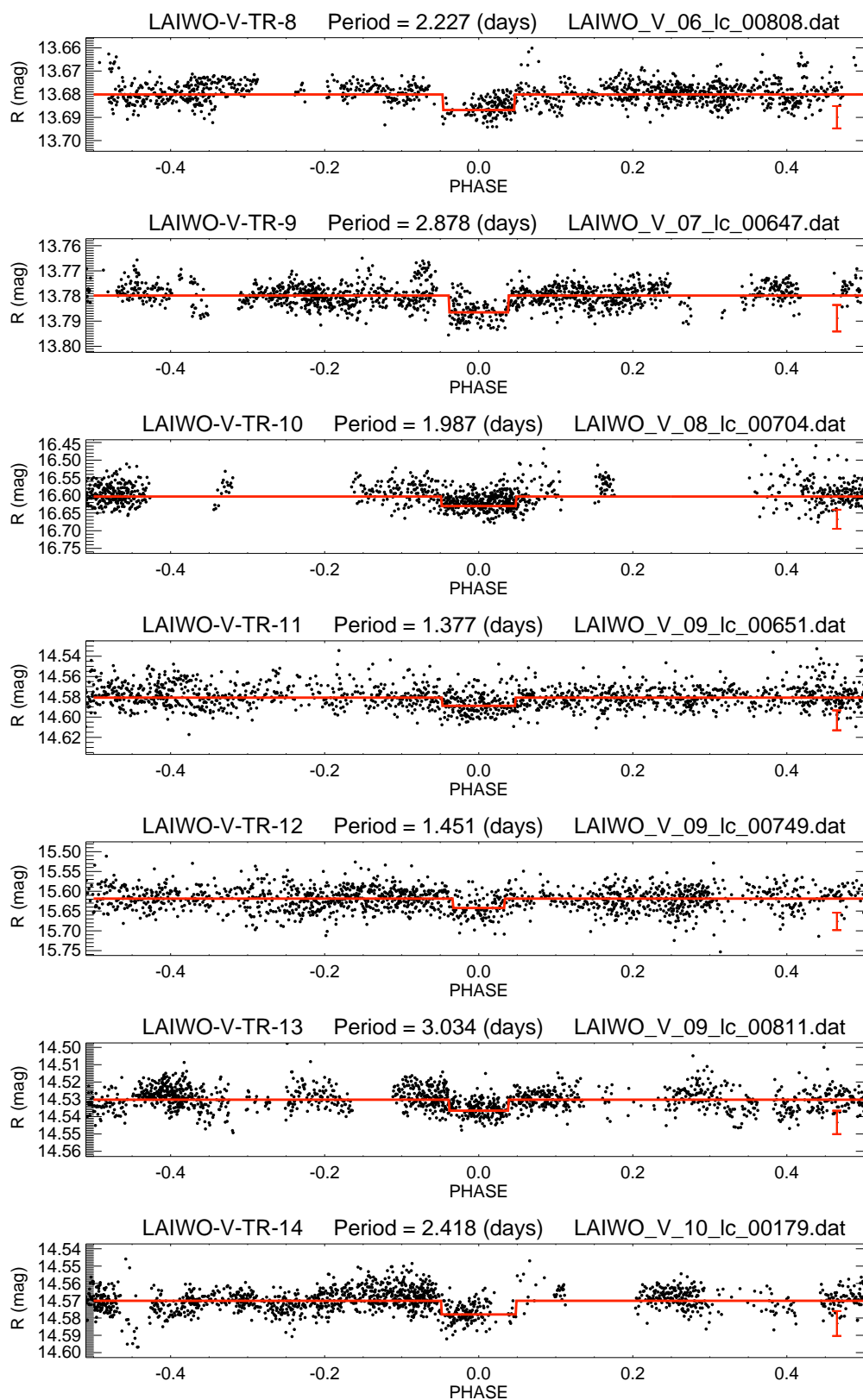
## Appendix A: Transit candidates

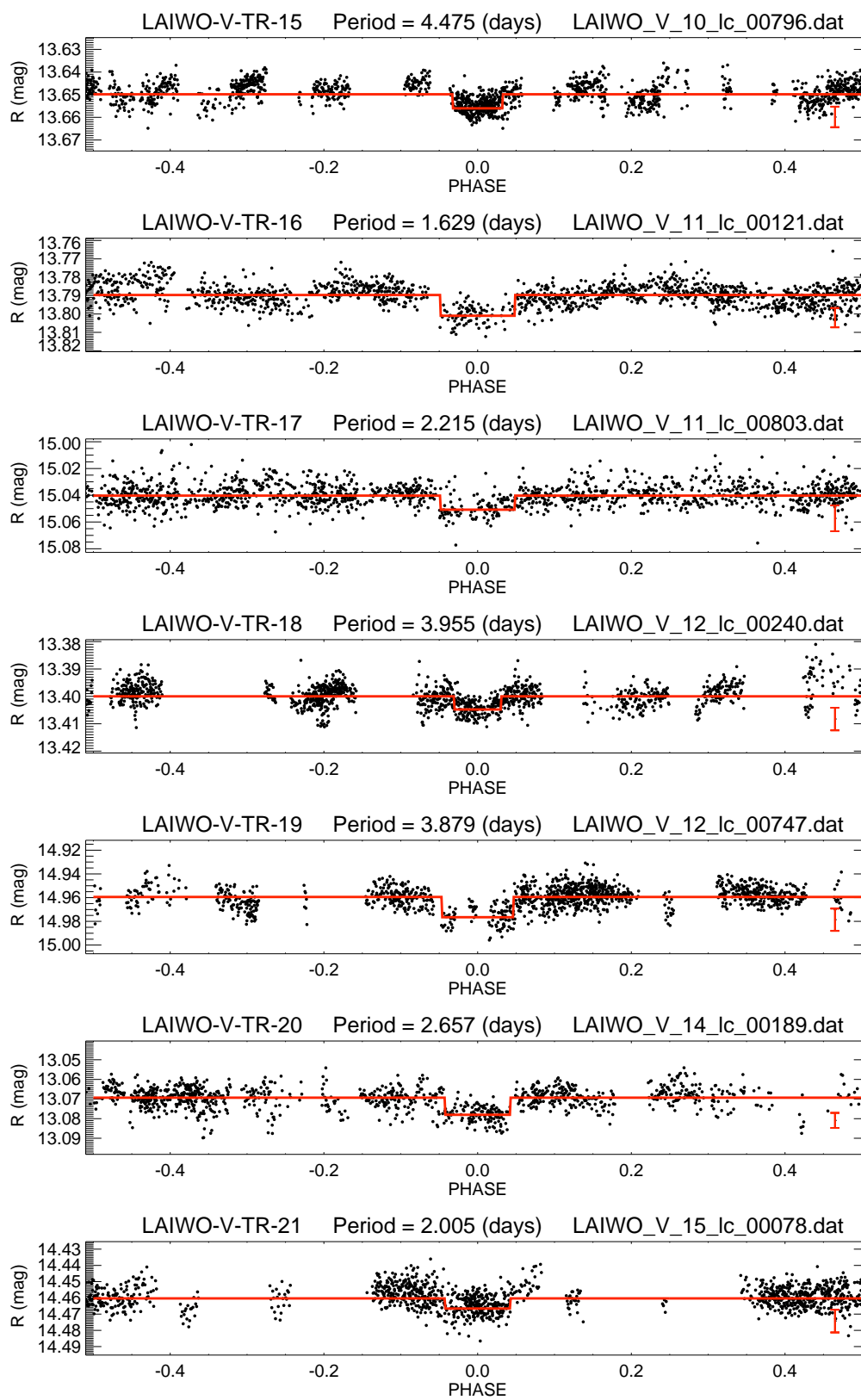
We phase-folded the light curves of the 22 transit candidates , identified in the LAIWO-V field. The horizontal axis of each plot represents the phase, ranging from -0.5 to +0.5. The vertical line is the apparent R magnitude after a match with the PPMXL astronomical catalog.

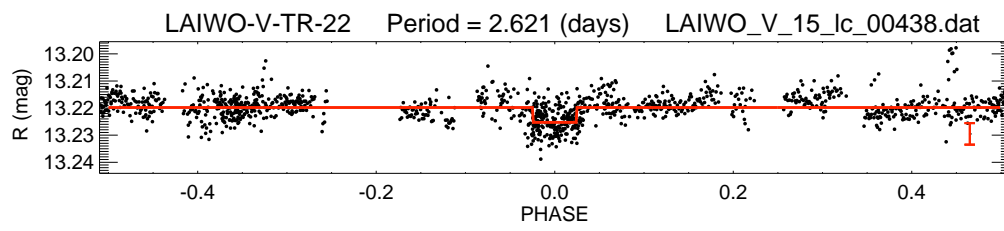
Above the plot of each individual light curve the transit identification number is indicated, followed by the orbital period of the system and the internal identification number, which consists of the LAIWO field ID, the number of the quadrant and the light curve number.

Finally, the average photometric error bar is displayed for each light curve at the lower right corner with red color.













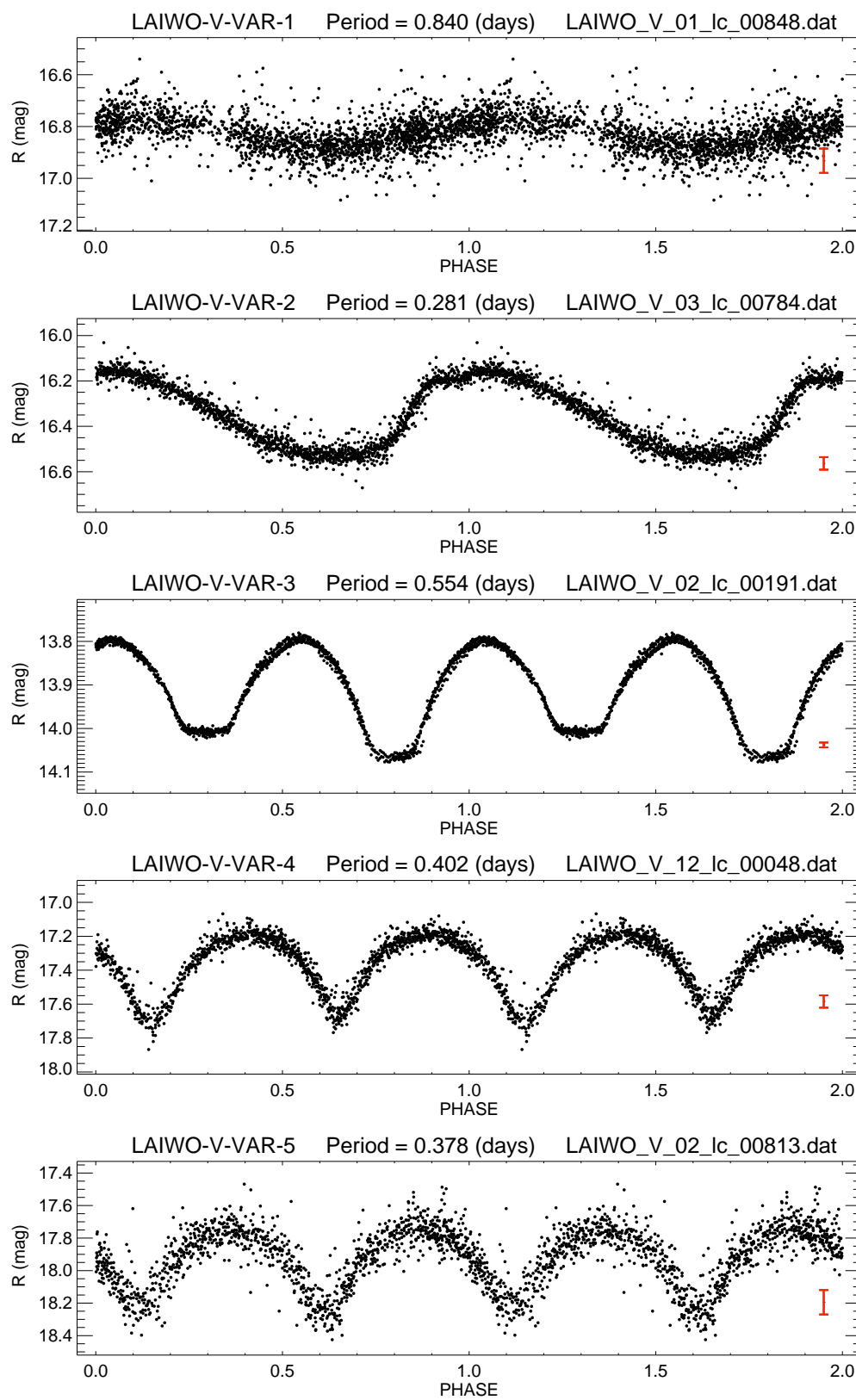
---

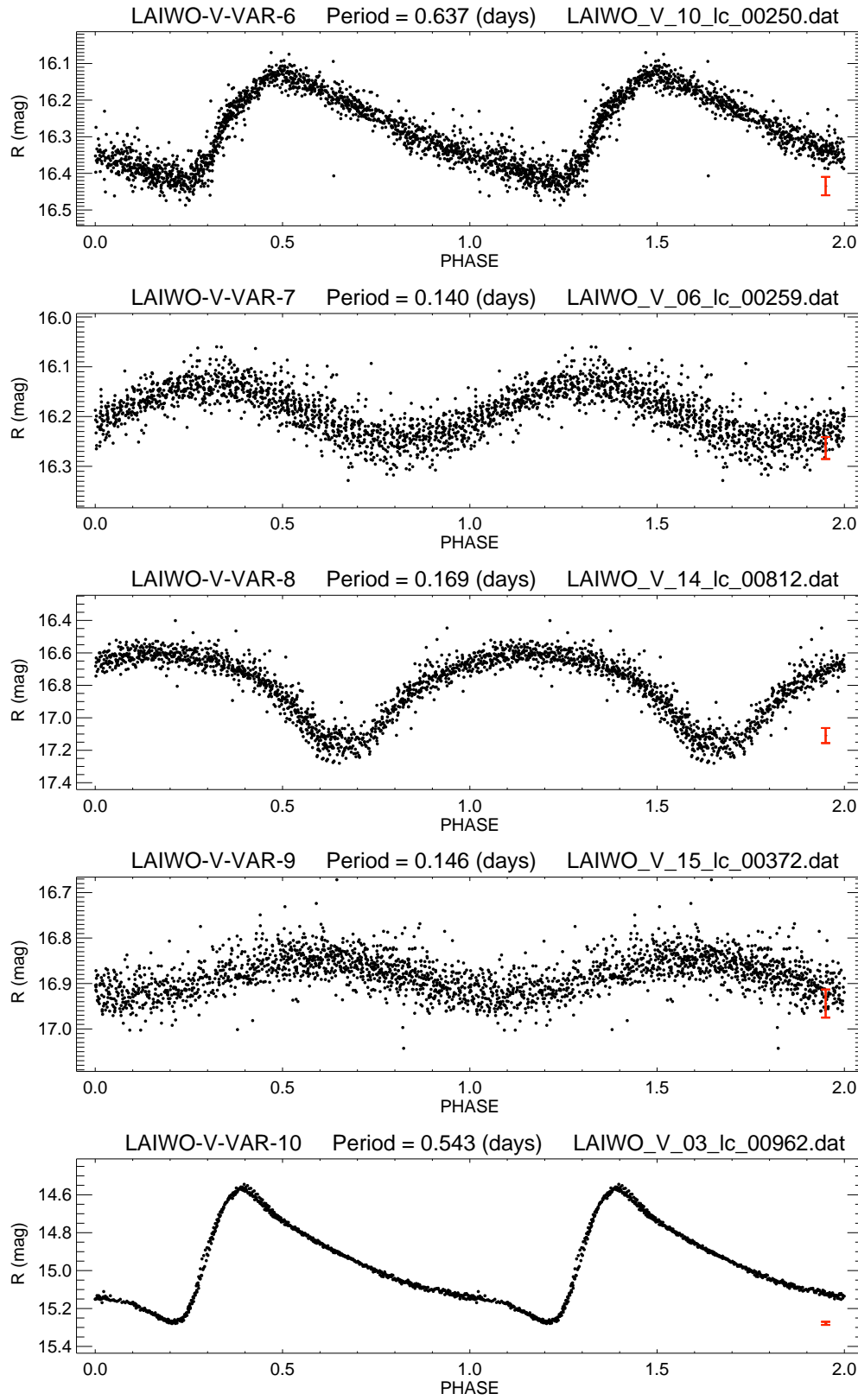
## Appendix B: Periodic variables

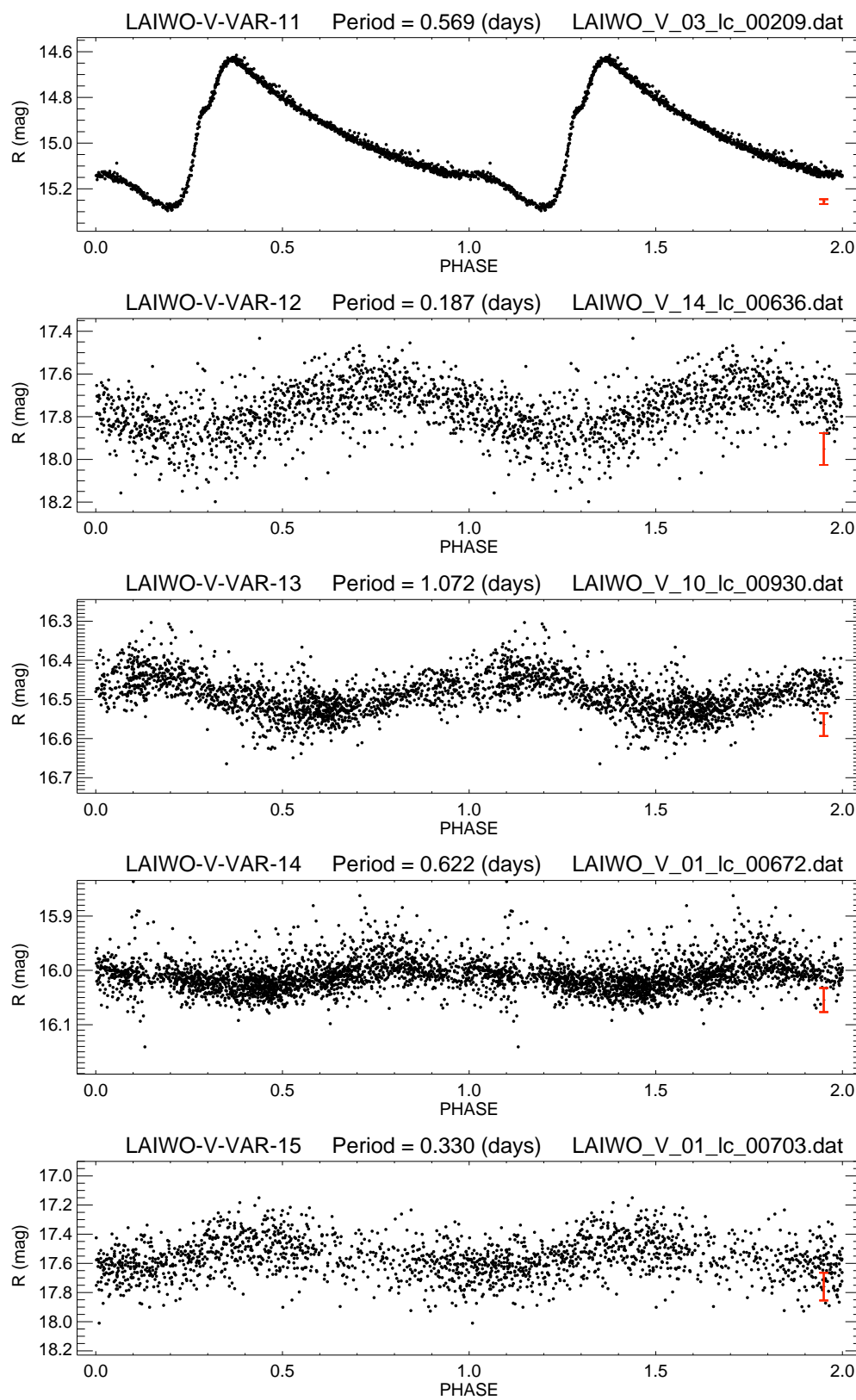
We phase-folded the light curves of all detected periodic variable stars, identified in the LAIWO-V field. The horizontal axis of each plot represents the phase (ranging from 0 to 2, for two periods). The vertical line is the apparent R magnitude after a match with the PPMXL astronomical catalog.

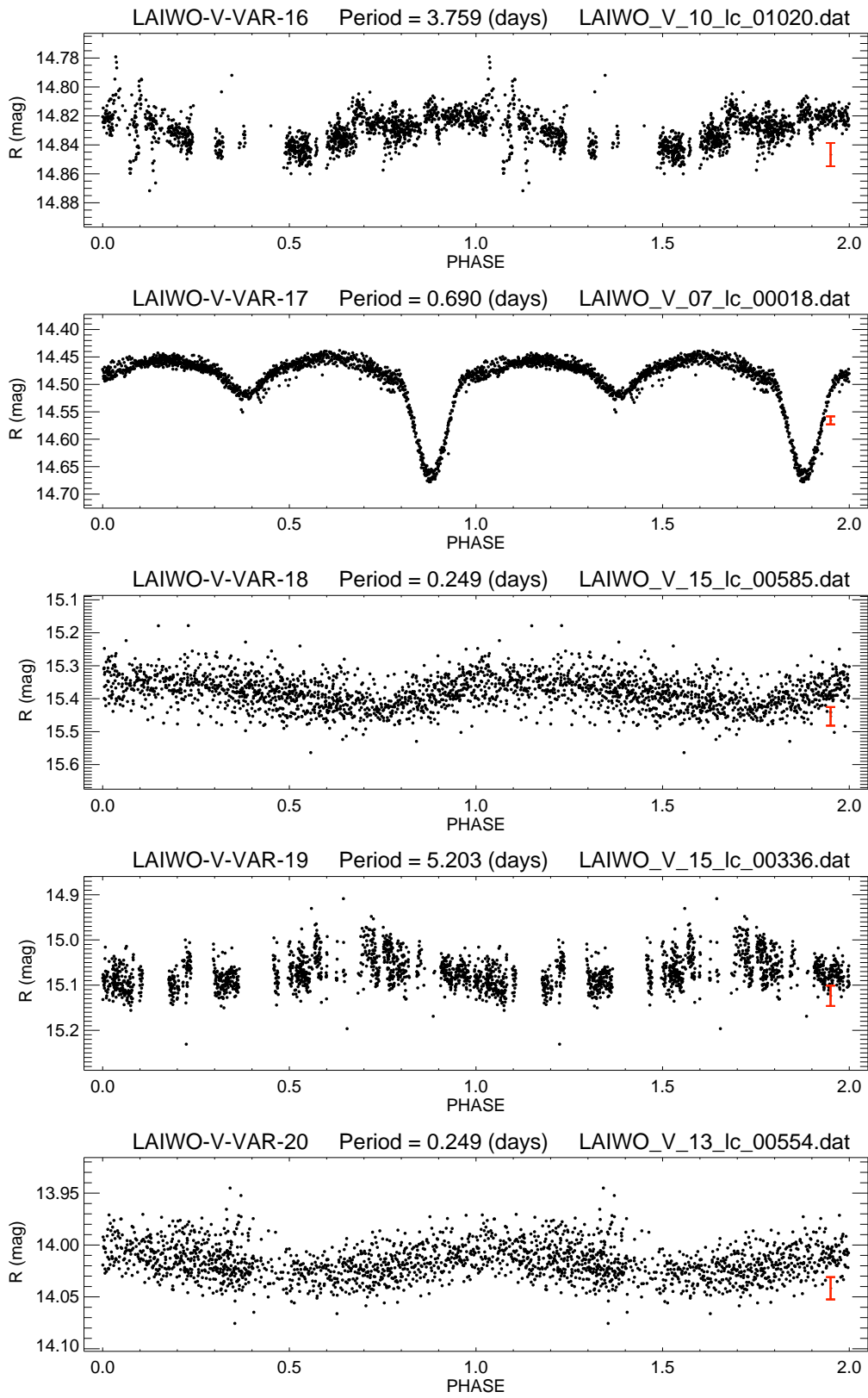
Above the plot of each individual light curve the variable identification number is indicated, followed by the orbital period of the system and the internal identification number, which consists of the LAIWO field ID, the number of the quadrant and the light curve number.

Finally, the average photometric error bar is displayed for each light curve at the lower right corner with red color.











---

## Bibliography

- Agol, E., Steffen, J., Sari, R. and Clarkson, W. 2005, MNRAS, 359, 567
- Allain, S., et al. 1995, STIN, 9625312A
- Alonso, R., et al. 2004, ApJ, 613, L153
- Baglin, A., et al. 2002, in ESA Special Publication, Vol. 485, Stellar Structure and Habitable Planet Finding, ed. B. Battrick, F. Favata, I. W. Roxburgh, & D. Galadi, 1724
- Bakos, G., et al. 2007, ApJ, 656, 552
- Bakos, G., Hartman, J., et al. 2011, arXiv:1101.0322v1
- Barman, T. S. 2008, ApJ, 676, L61
- Baumeister, H., et al. 2006, Proceedings of the SPIE, 6269
- Bertin, E. & Arnouts, S. 1996, A&A Suppl., 117, 393
- Bertin, E. 2006, in Astronomical Society of the Pacific Conference Series, Vol. 351, Astronomical Data Analysis Software and Systems XV, ed. C. Gabriel, C. Arviset, D. Ponz, & S. Enrique, 112
- Bevington, P. R. & Robinson, D. K. 2003, Data reduction and error analysis for the physical sciences, 3rd edn. (McGraw-Hill)

- Bouchy, F., et al. 2004, *A&A*, 421, L13
- Borucki, W., Koch, D., Batalha, N., Caldwell, D., Christensen-Dalsgaard, J., et al., A. 2010, *Science*, 327, 977
- Brown, T. M. 2003, *Astrophys. J., Lett*, 593, L125
- Charbonneau, D., Brown, T. M., Latham, D. W., & Mayor, M. 2000, *ApJ*, 529, L45
- Charbonneau, D., et al. 2005, *ApJ*, 626, 523
- Charbonneau, D., & Deming, D. 2007, *arXiv:0706.1047*
- Charbonneau, D., et al. 2007, *Protostars & Planets V*, 701
- Charbonneau, D., et al. 2008, *AJ*, 686, 1341
- Charbonneau, D. 2008, *arXiv:0808.3007*
- Claret, A. 2004, *A&A*, 428, 1001
- Collier Cameron, A., et al. 2007, *MNRAS*, 380, 1230
- Cox, A. N. 2000, *Allen's Astrophysical Quantities*, (Springer-Verlag: New York), p. 355-357
- Drake, A. J. 2003, *ApJ*, 589, 1020
- Forbes, C. 1911, *MNRAS*, 71, 578
- Fortney, J. J., et al. 2008, *ApJ*, 678, 1419
- Gaidos, E., et al. 2007, *Science*, 318, 210
- Greiner, J., Bornemann, W., Clemens, C., et al. 2008, *PASP*, 120, 405
- Gillon, M., et al. 2008, *arXiv:0812.1998*
- Gillon, M., et al. 2009, *A&A*, 496, 259
- Henry, G. W., Marcy, G. W., Butler, R. P., & Vogt, S. S. 2000, *ApJ*, 529, 41
- Holman, M. J., & Murray, N. W. 2005, *Science*, 307, 1288
- Holman, M. J., et al. 2006, *ApJ*, 652, 1715
- Holman, M. J., et al. 2007, *ApJ*, 664, 1185
- Holman, M. J., et al. 2010, *Science*, 330, 6000



- Knutson, H. A., Charbonneau, D., Allen, L. E., et al. 2007, *Nature*, 447, 183
- Konacki, M., Torres, G., Gha, S., & Sasselov, D. D. 2003, *Nature*, 421, 507
- Koppenhoefer, J., Afonso, C., Saglia, R. P., & Henning, T. 2009, *Astron. Astrophys*, 494, 707
- Kovács, G., Bakos, G., & Noyes, R. W. 2005, *Mon. Not. R. Astron. Soc*, 356, 557
- Kovacs, G., Zucker, S., & Mazeh, T. 2002, *A&A*, 391, 369
- Kraus, A. L. & Hillenbrand, L. A. 2007, *Astrophysical Journal*, 134, 2340
- Latham, D. W., et al. 2009, *ApJ*, 704, 1107
- Lomb, N. R. 1976, *Ap&SS*, 39, 447
- MacQueen, P. J., Moorhead, A. V., Morehead, R. C., & Orosz, J. A. 2010, *Science*, 330, 51
- Mandel, K. & Agol, E. 2002, *ApJ*, 580, L171
- Mayor, M. & Queloz, D. 1995, *Nature*, 378, 355
- Mazeh, T., et al. 2000, *ApJ*, 532, L55
- McCullough, P. R., Stys, J. E., Valenti, J. A., Fleming, S. W., Janes, K. A., & Heasley, J. N. 2005, *Publ.. Astron. Soc. Pac*, 117, 783
- McCullough, P. R., et al. 2006, *ApJ*, 648, 1228
- McLaughlin, D. B. 1924, *Astrophys. J*, 60, 22
- Moutou, C., et al. 2006, *Formation planétaire et exoplanètes*, Ecole thématique du CNRS, Goutelas (Loire), 23 - 27 mai 2005 Edited by J.-L. Halbwachs, D. Egret, and J.-M. Hameury. Strasbourg: Observatoire astronomique de Strasbourg et Société Française d'Astronomie et d'Astrophysique (SF2A), 2006, p. 55-79
- Nutzman, P. & Charbonneau, D. 2008, *Publ.. Astron. Soc. Pac*, 120, 317
- Pont, F., et al. 2005, *A&A*, 433, L21
- Pont, F., Zucker, S., & Queloz, D. 2006, *MNRAS*, 373, 231
- Press, W. H., Teukolsky, S. A., Vetterling, W. T., & Flannery, B. P. 1992, *Numerical recipes in C. The art of scientific computing*, ed. T.S.A.V.W.T.F.B.P. Press, W. H.

- Roeser, S., et al. 2010, *AJ*, 139, 2440
- Rossiter, R. A. 1924, *Astrophys. J*, 60, 15
- Scargle, J. D. 1982, *ApJ*, 263, 835
- Schlesinger, F. 1911, *MNRAS*, 71, 719
- Scholz, A., & Eislöffel, J. 2004, *A&A*, 419, 249
- Seager, S., & Sasselov, D. D. 2000, *ApJ*, 537, 916
- Seager, S., & Mallén-Ornelas, G. 2003, *ApJ*, 585, 1038
- Sirko, E. & Paczyński, B. 2003, *Astrophys. J*, 592, 1217
- Skrutskie, M. F., et al. 2006, *AJ*, 131, 1163
- Smith, H., *RR Lyrae Stars*, Cambridge University Press, 2004 - Science
- Soszynski, I., Szewczyk, O., Wyrzykowski, L., & Pietrzynski, G. 2002a, L41
- Stebbins, J., 1920, *ApJ*, 51, 218S
- Swain, M. R., Vasisht, G., & Tinetti, G. 2008, *Nature*, 452, 329
- Tamuz, O., Mazeh, T., & Zucker, S. 2005, *MNRAS*, 356, 1466
- Tingley, B. & Sackett, P. D. 2005, *Astrophys. J*, 627, 1011
- Udalski, A., Paczynski, B., Zebrun, K., Szymanski, M., Kubiak, M., Soszynski, I., Szewczyk, O., Wyrzykowski, L., & Pietrzynski, G. 2002a, *Acta Astron.*, 52, 1
- Udalski, A., Paczynski, B., Zebrun, K., Szymanski, M., Kubiak, M., Soszynski, I., Szewczyk, O., Wyrzykowski, L., & Pietrzynski, G. 2002b, *Acta Astron.*, 52, 115
- Udalski, A., Szewczyk, O., Zebrun, K., Pietrzynski, G., Szymanski, M., Kubiak, M., Soszynski, I., & Wyrzykowski, L. 2002c, *Acta Astron.*, 52, 317
- Udalski, A., Pietrzynski, G., Szymanski, M., Kubiak, M., Zebrun, K., Soszynski, I., Szewczyk, O., & Wyrzykowski, L. 2003, *Acta Astronomica*, 53, 133
- von Zeipel, H. 1924, *MNRAS*, 84, 665
- Winn, J. N. et al. 2006, *ApJ*, 653, L69
- Winn, J. N. et al. 2007, *AJ*, 133, 1828

---

Winn, J., Holman, M., Carter, J., Torres, G., Osip, D., Beatty, T., 2009, AJ, 137, 3826W

Winn, J. 2010, arXiv:1001.2010

Wilson, D. M., et al. 2008, ApJ, 675, L113

Wolszczan, A. & Frail, D. A. 1992, Nature, 355, 145